



Nanopatterning of 2D materials by block copolymer self-assembly

Nielsen, Christina Breth

Publication date:
2023

Document Version
Publisher's PDF, also known as Version of record

[Link back to DTU Orbit](#)

Citation (APA):
Nielsen, C. B. (2023). *Nanopatterning of 2D materials by block copolymer self-assembly*. Technical University of Denmark.

General rights

Copyright and moral rights for the publications made accessible in the public portal are retained by the authors and/or other copyright owners and it is a condition of accessing publications that users recognise and abide by the legal requirements associated with these rights.

- Users may download and print one copy of any publication from the public portal for the purpose of private study or research.
- You may not further distribute the material or use it for any profit-making activity or commercial gain
- You may freely distribute the URL identifying the publication in the public portal

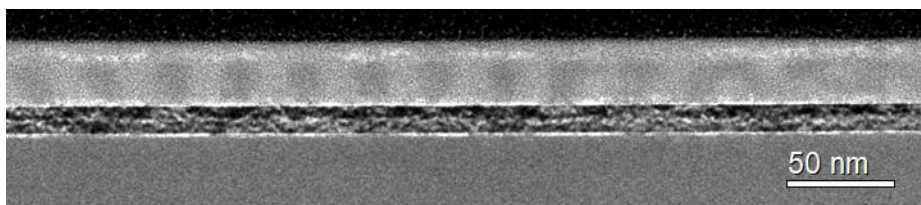
If you believe that this document breaches copyright please contact us providing details, and we will remove access to the work immediately and investigate your claim.



Nanopatterning of 2D materials by block copolymer self-assembly

PhD thesis

Christina Breth Nielsen



Supervisor: Professor Kristoffer Almdal

Co-supervisor: Associate Professor Timothy J. Booth

Department of Chemistry

Technical University of Denmark

Marts, 2023

Abstract

As we face emerging global challenges, such as rising energy consumption and drinking water scarcity it is necessary that we invest in the research and development of new technologies. Nanopatterning using block copolymer (BCP) self-assembly is a promising way to advancements in applications ranging from water treatment technologies to energy-efficient devices. 2D materials have also shown great potential for many future technologies, including the aforementioned.

Nano-structuring of 2D materials is key to tuning their properties, for example introducing a bandgap in graphene via a nanomesh or nanoribbons. This requires high-quality periodic patterns with nanoscale resolution over large areas. Most conventional nanostructuring techniques for 2D materials are difficult to scale. BCP nanopatterning can offer a scalable solution, but few studies show this technique applied to 2D materials beyond graphene. Different surface interactions on various 2D materials can have a determining role in BCP microphase segregation. In this PhD thesis, the anionic polymerization of cylindrical forming polystyrene-*block*-polydimethylsiloxane, (PS-*b*-PDMS) is reported and for the first time, the characterization and direct confirmation of its formation are done through a fast multidimensional ^1H - ^{29}Si HMBC NMR experiment. Furthermore, the self-assembly of cylindrical forming PS-*b*-PDMS on mechanically exfoliated hexagonal boron nitride (hBN) is investigated and used for the nanopatterning of hBN and an hBN encapsulated graphene van der Waals (vdW) heterostructure.

The use of soft topographic guiding patterns for the directed self-assembly (DSA) of cylindrical forming PS-*b*-PDMS is also being studied on top of 2D materials. The main goal with this is to achieve ordered PDMS nanochannels that can be encapsulated between 2D materials for the fabrication of a nanofluidic device.

The discoveries presented in this thesis aim to uncover the immense potential of BCP nanopatterning in conjunction with 2D materials and to inspire further exploration of this exciting research area.

Dansk resume

Med globale udfordringer, såsom stigende energiforbrug og drikkevandsmangel, er det nødvendigt at vi investerer i forskning og udvikling af nye teknologier. Nanostrukturering vha. blok copolymer (BCP) selvorganisering er en lovende metode til at forbedre både vandbehandlings- og energieffektive teknologier. 2D materialer har også vist stort potentiale for mange teknologier inklusiv de før omtalte.

Nanostrukturering af 2D materialer er vigtigt for at kunne justere deres egenskaber, for eksempel ved at åbne et bånd gap i grafen via et nanonet eller nanobånd. Dette kræver periodiske mønstre af høj kvalitet med nanoskala opløsning over store områder. De fleste konventionelle nanostruktureringsteknikker brugt til 2D materialer er svære at skalere. BCP nanostrukturering er en skalerbar løsning, men der er få studier der anvender denne teknik på andre 2D materialer ud over grafen. 2D materialer har forskellige overfladeinteraktioner hvilket kan have en afgørende betydning for BCP-mikrofaseadskillelsen.

I denne PhD afhandling rapporteres den anioniske polymerisering af cylindrisk formede polystyren-*block*-polydimethylsiloxane, (PS-*b*-PDMS) og for første gang bliver denne karakteriseret og direkte bekræftet dannet ud fra et hurtigt multidimensionalt ^1H - ^{29}Si HMBC NMR eksperiment. Endvidere er selvorganisering af cylindrisk formede PS-*b*-PDMS oven på mekanisk eksfolieret hexagonal bornitrid (hBN) undersøgt og brugt til nanostrukturering af hBN og en hBN-indkapslet graphene van der Waals (vdW) heterostruktur.

Brugen af bløde topografiske guide mønstre til direkte selvorganisering (DSA) af cylindrisk formede PS-*b*-PDMS er også studeret på 2D materialer. Hovedformålet med dette, er at opnå ordnet PDMS nanokanaler der kan indkapsles mellem 2D materialer til at fremstille en nanofluidic enhed.

Opdagelserne præsenteret i denne afhandling har til formål at afdække det enorme potentiale der er for BCP nanostrukturering i sammenhæng med 2D materialer og at inspirere til yderligere eksploration af dette spændende forskningsområde.

Preface and acknowledgement

This PhD thesis investigates the synthesis of a high- χ block copolymer (BCP) system and its potential BCP self-assembly use on 2D materials. The background for this project originates from the now-terminated Center for Nanostructured Graphene (CNG). This thesis contains six chapters, covering; First, an introduction to BCPs and their self-assembly followed by an introduction to 2D materials and heterostructures. The second chapter gives a brief overview of previous research in the field of BCP nanopatterning of 2D materials. In chapter 3, the anionic polymerization of PS-*b*-PDMS and its molecular characterization with ^1H - and ^1H - ^{29}Si HMBC Nuclear Magnetic Resonance (NMR) and size-exclusion chromatography (SEC) are presented and discussed. Chapter 4 concerns the self-assembly process, of PS-*b*-PDMS directly on 2D materials, and the following nanopatterning, which is introduced in detail. The use of topographic features to guide the PS-*b*-PDMS self-assembly on 2D is presented and discussed in chapter 5. Lastly, a chapter collecting the most important conclusions and discussion is found together with an outline presenting future perspectives.

The initial steps using topographic guiding patterns, described in chapter 5, were performed during my stay abroad at the National Graphene Institute (NGI), University of Manchester (UoM), United Kingdom, June-Aug 2022. The cross-sectional lift-outs, electron microscopy investigations and NanoFrazor lithography found in chapters 4 and 5 were all conducted in collaboration with colleagues from the Department of physics, - Nanolab, Technical University of Denmark (DTU) or NGI, (UoM).

The studies were done under the supervision of Assoc. prof. Tim Booth, DTU physics and prof. Kristoffer Almdal, DTU Chemistry. The research presented has mainly been conducted at the Departments of Chemistry and Physics (DTU). With the past 3 years, among other things, offering a new scientific field, unforeseen Covid-19 lockdowns, and laboratory movements it has truly been an exciting, educational, and challenging journey, both on a professional and personal level.

First, I would like to thank my main supervisor Prof. Kristoffer Almdal, who has been a great help with my entrance to the field of polymers and anionic polymerization as well as with administrative work. I would further like to express my gratitude to him and my co-supervisor, Assoc. Prof. Tim Booth for precious discussions during our supervisor meetings and for the initiatives concerning my research. In addition, I would like to thank the members of the Polymers and Functional Interfaces group and the Applied 2D Materials group for the scientific discussions, laboratory guidance, social events and support during my PhD. A special thanks to Anton Lyksborg-Andersen, Shima Kadkhodazadeh and Jeppe Ormstrup for the many hours spent together doing cross-sectional lift-outs and electron microscopy. Furthermore, a big thanks to Leonid Iliushyn and Xiang Cheng for the support with 2D material fabrication and to Nolan Lassaline and Thiago Sousa for providing me with the lithography pre-patterning of some of the samples.

During my stay abroad, I worked under the supervision of Prof. Radha Boya from the Department of Physics and Astronomy (UoM). I would like to give her a heartfelt thanks for the opportunity to join her group and for providing me with a safe and supportive research environment. A special thanks to the staff at NGI and Max Rimmer who became a dear colleague during my time in Manchester.

Further, I would like to express my gratitude to Kasper Enemark-Rasmussen who helped me with the NMR studies and to Lotte Nielsen and Lars Schulte from DTU Health Tech who gave me laboratory assistance at the start of my PhD

Lastly, I would like to give a big thanks to my friends and family, who have supported me and helped me keep my head high throughout this journey.

I am thankful for the financial support provided by the Department of Chemistry (DTU) and the Center for Nanostructured Graphene (CNG), sponsored by the Danish National Research Foundation.

Christina Breth Nielsen

Kongens Lyngby, Marts 30th 2023

List of abbreviations

| | |
|-------------------------|--------------------------------------------|
| AFM | Atomic force microscopy |
| ASAP | Acceleration sharing adjacent polarization |
| BCP | Block copolymer |
| BF | Bright Field |
| Bu₂Mg | Dibutylmagnesium (1M solution in heptane) |
| CAB | Cellulose acetate butyrate |
| CDCl₃ | Deuterated chloroform |
| CHX | Cyclohexane (HPLC grade) |
| CTMS | Chlorotrimethylsilane (≥99.0%) |
| CVD | Chemical vapor deposition |
| D₃ | Hexamethylcyclotrisiloxane |
| DC | Direct current |
| DI | Deionized |
| DIS | Disordered state |
| DMSO | Dimethyl sulfoxide |
| DP | Degree of polymerization |
| DSA | Directed self-assembly |
| EBL | Electron Beam Lithography |
| EELS | Energy Electron Loss Spectroscopy |
| FIB | Focus Ion beam |
| FWHM | Full width at half maximum |
| GNM | Graphene nanomesh |
| GNR | Graphene nanoribbons |
| Gr | Graphene |
| hBN | Hexagonal Boron Nitride |
| HMBC | Heteronuclear multiplebond correlation |

| | |
|--------------------------------------------------------|---------------------------------------------------------------------------------------|
| HAADF | High-angle annular dark-field imaging |
| IPA | Isopropanol |
| KOH | Potassium hydroxide |
| MBE | Molecular Beam Epitaxy |
| MeOH | Methanol (HPLC grade) |
| n-BuLi | n-Butyllithium (1.6M solution in hexane) |
| NMR | Nuclear magnetic resonance |
| O_x-PDMS | Oxidized PDMS into (silicon oxycarbide) |
| P2VP-<i>b</i>-PS-<i>b</i>-P2VP | poly(2-vinylpyridine)- <i>block</i> -polystyrene- <i>block</i> -poly(2-vinylpyridine) |
| PDI | Polydispersity index |
| PDMS | Polydimethylsiloxane |
| PGME | Propylene glycol methyl ether |
| PGMEA | Propylene glycol monomethyl ether acetate |
| PMMA | Poly(methyl methacrylate) |
| PMMA/MA | Poly(methylmethacrylate-co-methacrylic acid) |
| PPC-<i>b</i>-PS | Poly(propylene carbonate)- <i>block</i> -polystyrene |
| PS | Polystyrene |
| PS-<i>b</i>-PDMS | Polystyrene- <i>block</i> -Polydimethylsiloxane |
| PS-<i>b</i>-PLA | Polystyrene- <i>block</i> -polylactide |
| PS-<i>b</i>-PMMA | Polystyrene- <i>block</i> -poly(methyl methacrylate) |
| PS-<i>b</i>-P_xVP (<i>x</i> = 2 or 4) | Polystyrene- <i>block</i> -poly(<i>x</i> -vinylpyridine) |
| PSLi⁺ | Polystyryllithium |
| RI | Refractive Index |
| RIE | Reactive Ion Etching |
| rpm | Revolutions per minut |
| RLi | Organolithium |
| RT | Room temperature (21°C) |
| S-Butyl | Sec-Butyl (CH ₃ -CH ₂ -CH(CH ₃)-) |

| | |
|-----------------------------|------------------------------------------------------|
| sccm | Standard cubic centimeters per minute |
| SCMF | Self-consistent mean-field |
| SEC | Size exclusion chromatography |
| sec-BuLi | Sec-Butyllithium (1.4M solution in cyclohexane) |
| SEM | Scanning Electron Microscope |
| Si | Silicon |
| SiN | Silicon nitride |
| SiO₂ | Silicon dioxide |
| SIS | Sequential Infiltration Synthesis |
| STEM | Scanning Transmission Electron Microscopy |
| SVA | Solvent vapor annealing |
| TEM | Transmission Electron Microscopy |
| THF | Tetrahydrofuran (HPLC grade) |
| TMD | Transition metal dichalcogenide |
| TMS | Trimethylsilyl (-Si(CH ₃) ₃) |
| t-SPL | Thermal Scanning probe lithography |
| UV | Ultraviolet |
| vdW | Van der Waals |
| L_0 | Domain/natural periodicity |
| M_n | Number average molecular weight |
| M_w | Weight average molecular weight |
| M_z | Higher average molecular weight |
| N | Degree of polymerization |
| V_{Ret} | Retention volume |
| χ | Flory-Huggins interaction parameter |

Contents

| | |
|------------------------------------------------------------------|-----|
| Abstract | I |
| Dansk resume | II |
| Preface and acknowledgement | III |
| List of abbreviations | V |
| 1 Introduction..... | 1 |
| 1.1 Block copolymers | 2 |
| 1.1.1 Block copolymer self-assembly | 3 |
| 1.1.2 Self-assembly in thin films | 5 |
| 1.1.1 Annealing methods | 6 |
| 1.2 2D materials..... | 7 |
| 1.2.1 Graphene | 8 |
| 1.2.2 Hexagonal boron nitride | 9 |
| 1.2.3 Van der Waals Heterostructures..... | 10 |
| 2 Block copolymer nanopatterning..... | 11 |
| 2.1 The block copolymer nanopatterning process | 12 |
| 2.1.1 Directed self-assembly | 13 |
| 2.2 Block copolymer nanopatterning using PS- <i>b</i> -PDMS..... | 15 |
| 2.3 Block copolymer nanopatterning of 2D materials | 17 |
| 3 Anionic polymerization of PS- <i>b</i> -PDMS | 19 |
| 3.1 Introduction..... | 19 |
| 3.2 Experimental..... | 23 |
| 3.2.1 Materials, setup and purification | 23 |

| | | |
|-------|--------------------------------------------------------------------------------------------|----|
| 3.2.2 | Nuclear magnetic Resonance..... | 24 |
| 3.2.3 | Size Exclusion Chromatography | 25 |
| 3.3 | Results and discussion..... | 26 |
| 3.3.1 | ^1H -NMR analysis | 29 |
| 3.3.1 | ^{29}Si -NMR analysis..... | 34 |
| 3.3.2 | ^1H - ^{29}Si HMBC NMR analysis..... | 36 |
| 3.3.3 | Investigating kinetics with ^1H and ^1H - ^{29}Si HMBC NMR..... | 38 |
| 3.3.1 | Homopolymer removal..... | 42 |
| 3.4 | Summary | 43 |
| 4 | Self-assembly of PS- <i>b</i> -PDMS on 2D materials | 45 |
| 4.1 | Introduction..... | 45 |
| 4.2 | Experimental..... | 47 |
| 4.2.1 | Materials and sample fabrication..... | 47 |
| 4.2.2 | Atomic force microscopy..... | 48 |
| 4.2.3 | Electron microscopy and focus ion beam processing | 49 |
| 4.1 | Results and discussion..... | 50 |
| 4.1.1 | PS- <i>b</i> -PDMS self-assembly on hBN..... | 51 |
| 4.1.1 | PS- <i>b</i> -PDMS self-assembly on hBN/Graphene/hBN | 57 |
| 4.2 | Summary | 58 |
| 5 | PDMS nanofluidic channel fabrication on 2D materials..... | 59 |
| 5.1 | Introduction..... | 59 |
| 5.2 | Experimental..... | 61 |
| 5.2.1 | Materials and sample fabrication..... | 61 |
| 5.2.2 | Topographic guiding patterns | 62 |

| | | |
|-------|-----------------------------------------------------------|-----|
| 5.2.3 | Transfer methods | 65 |
| 5.3 | Results and discussion | 65 |
| 5.3.1 | Trench patterns made with E-beam lithography | 69 |
| 5.3.2 | Trench patterns made with photolithography | 72 |
| 5.3.1 | Trench patterns made with t-SPL..... | 75 |
| 5.3.2 | Transfer | 77 |
| 5.4 | Summary | 80 |
| 6 | Conclusion | 82 |
| 6.1 | Outlook | 83 |
| | Appendix..... | 85 |
| A. | Conference contributions | 85 |
| B. | Anionic polymerization of PS- <i>b</i> -PDMS | 86 |
| C. | Self-assembly of PS- <i>b</i> -PDMS on 2D materials | 89 |
| D. | PDMS nanofluidic channel fabrication on 2D materials..... | 93 |
| | Bibliography | 97 |
| E. | Manuscript | 107 |

1 Introduction

The global challenges such as the scarcity of drinking water and rising energy consumption are the results of an increase in population growth and industrialization. To solve these problems, new technologies e.g. desalination, wastewater treatment and power consumption reduction are required. This has led researchers to look into new materials and manufacturing processes that can lay the foundation for future separation technologies [11-13] and electronics [9, 14, 15].

In the search for new materials for such technological solutions, 2D materials have come into play due to their atomically flat structures, unique physical properties and the big playground of material composites they open up [16]. Here especially, graphene, hexagonal boron nitride (hBN) and transition metal dichalcogenides (TMDs) are of interest for future membrane- [17-19] and semiconductor materials [9, 20-22].

However, for such technologies, structuring of the composed materials is required. A good example is membranes that separate salts, heavy metals or other contaminants. This requires pore patterns, often of different sizes and/or chemical affinities to remove contaminants of different sizes and chemistry [23]. Also, electronics require structuring for circuit- and electrode patterns and for electronics fabricated from 2D materials, structuring can offer a way to alter the fundamental material properties [9, 15, 24, 25].

Nanopatterning has emerged as a solution for increasing selectivity and processing power by enabling the shrinkage of device feature sizes. Nanopatterning, also known as nanolithography, is a process that involves creating nanoscale patterns on the surface of the material. It can be performed through many techniques including optical lithography, scanning probe lithography (SPL) and electron beam lithography (EBL). Most of these techniques are time-consuming and they do not offer a low-cost

and large-scale process for industrial purposes. On the other hand, block copolymer (BCP) nanopatterning is very promising in terms of scalability and cost [13].

The BCP nanopatterning process is based on BCPs and their ability to self-assemble into various nanostructures. BCPs have been around since the 1950s and are commercially used in shoe soles, as the pressure-sensitive adhesive on the back of your post-it note and to modify asphalt so it can resist large temperature fluctuations [26]. However, in recent years the self-assembly of BCPs has gathered massive interest from the semiconductor industry due to its high potential as template materials for large-scale nanopatterns down to sub-10 nm dimensions [13, 27]. Additionally, not only has the BCP nanopatterning process shown useful to nanopattern 2D materials for e.g. sensor- and electronic applications [12, 15, 20, 28, 29], but it has also been useful in combining 2D materials and BCPs into applications such as memristors [30].

The scope of this thesis is to investigate the synthesis and characterization of a silicon-containing BCP together with its BCP nanopatterning process and applications in conjunction with 2D materials. The first part of the thesis will explore the synthesis of polystyrene-*block*-polydimethylsiloxane (PS-*b*-PDMS), together with a new characterization method for silicon-containing BCPs. With PS-*b*-PDMS being the main material connecting this thesis, a second part will investigate its BCP nanopatterning process performed on exfoliated 2D materials and how a combination of BCPs and 2D materials can create new fluidic devices. Before getting to any of this, a brief background on BCPs, their self-assembly and usage for 2D materials nanopatterning will be presented.

1.1 Block copolymers

BCPs has been around for more than 50 years and is commercially utilized in many of today's thermoplastic elastomer applications e.g. footwear and adhesives. Their history took off with the discovery of living anionic polymerization (1956), which also

opened up for the possibility to combine thermodynamically incompatible polymer blocks such as polystyrene (PS) and polydimethylsiloxane (PDMS). With this other promising applications based on the self-assembly of these BCPs into various structures were presented first through theory and later in practice [26, 31]. In this section, the background on BCPs and their self-assembly in bulk melts and thin films will be described together with annealing methods used to drive the self-assembly into equilibrium structures.

1.1.1 Block copolymer self-assembly

A polymer structure composed of two or more chemically different molecular units e.g. A and B is called a copolymer. If arranged in specific segments/blocks e.g. [A-A-A]-[B-B-B] and covalently bonded to each other it is called a block copolymer (BCP). The molecular design of BCPs spans a wide range of structures from linear-, cyclic-, branched- and star architectures combining different block sequences using two or more monomer units [26, 32]. Due to the difference in chemistry between the blocks, BCPs can self-assemble into different microphase separated morphologies with controllable dimensions. The self-assembly process is driven by thermodynamics and the most studied BCP system is the linear diblock copolymers which consist of two blocks in a highly flexible polymer chain [33]. The microphase separation morphologies found in diblock copolymer melts are well known and described with the phase diagram found in Figure 1A. The presented phase diagram is theoretically predicted by self-consistent mean-field (SCMF) theory based on diblock copolymer melts [2, 34]. It shows the Flory-Huggins interaction parameter, χ times the degree of polymerization, N as a function of the volume fraction, f , of one of the blocks (A or B). These are the BCP characteristics where, N and f are values one can tune in a

polymer synthesis laboratory resulting in different equilibrium morphologies such as lamellas (L), hexagonally packed cylinders (H), and body-centred spheres (Q^{229}), illustrated in Figure 1B [2]. The BCP domain sizes are controlled by the molecular weight and therefore N and χ , which describe the interaction between the two blocks and are inversely proportional to the temperature [32, 33].

As seen in Figure 1A, below $\chi N \ll 10.5$, a disordered BCPs state is found (DIS) and two limits are introduced, the strong segregation limit (SSL, $\chi N \gg 10.5$) and the weak segregation limit (WSL, $\chi N \approx 10.5$). In the SSL the domain periodicity (L_0), scales as $N^{2/3}\chi^{1/6}$ while in the WSL it scales as $N^{1/2}$. From this, it is clear that a high- χ parameter is important to achieve small domain periodicities [35].

This thesis only concerns diblock copolymers, which from now on, throughout this thesis will be referred to as block copolymers (BCPs) for simplicity.

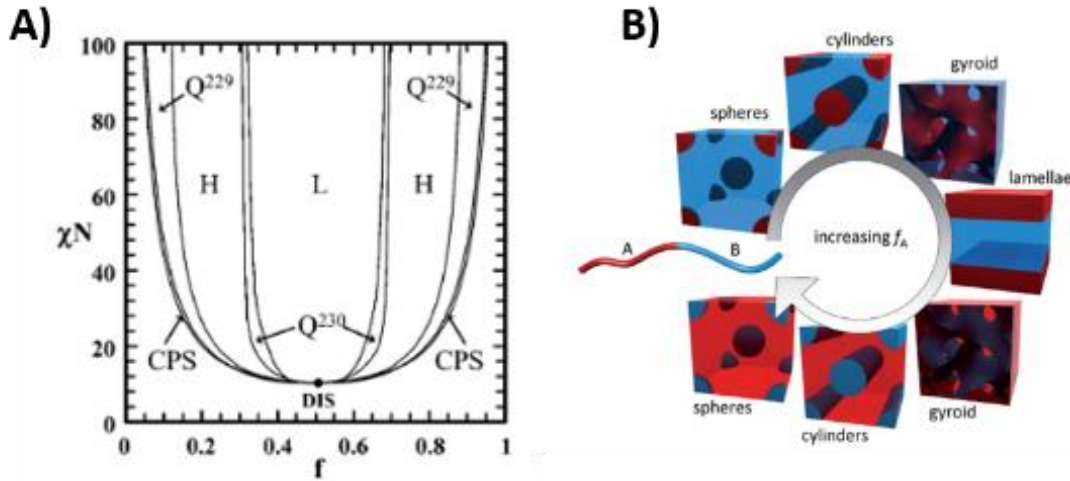


Figure 1: **A)** Theoretical phase diagram for a diblock copolymer melt adapted from ref. [2]. DIS=disordered, H=hexagonal/cylinders, L=lamellae, CPS=cubic packed spheres, Q^{229} = body-centered spherical phase ($Im\bar{3}m$) and Q^{230} =double-gyroid phase. **B)** Illustration of the different phase morphologies found in diblock copolymer melt when changing the volume fraction, f_A , adapted from [8]. The reader is referred to the main text for further details.

1.1.2 Self-assembly in thin films

In general, the BCP self-assembly in thin films deviates from the one found in bulk melts since additional parameters concerning the film thickness and interactions at the BCP/substrate and BCP/air surface interface have to be considered. A film thickness corresponding to an integer unit of L_0 would in the ideal case e.g. for cylindrical forming BCPs tend to form cylindrical structures parallel to the substrate surface [36]. However, various phases have been predicted to appear dependent on the film thickness, creating both parallel and perpendicular structure alignments [37]. To drive the system towards the ideal equilibrium case, an annealing step is often applied. The initial non-integer film thicknesses cause an increase in the free energy of the BCP system by stretching and compressing the microdomains. Through the annealing process, this is circumvented by the formation of terraces (sometimes referred to as dewetting) in the final structure. These terraces will have terrace thicknesses either smaller or larger than L_0 [38]. Details concerning the annealing process are presented in the following section, 1.1.1.

Moreover, the surface energies of the substrate and the BCP can influence the wettability and cause so-called wetting layers at the different interfaces, which is not desirable for application purposes [35, 39, 40]. Usually, the block in the BCP with the lowest surface energy will wet the smooth substrate surface to lower the system's free energy. In studies concerning BCP thin film applications, much attention has been put on the BCP/substrate interface where the wetting is often controlled by the functionalization of the substrate by polymer brushes [6, 38, 39, 41, 42]. In addition, this functionalization has also been shown to extend the long range ordering, reduce BCP pattern defects and be able to control the orientation of the domain features [39, 42]. The wetting at the BCP/air interface and the orientation of the domains can also be controlled by the use of a top-coat. This has shown to be useful, especially for lamellae and cylindrical morphologies, where features normal to the substrate surface are often of interest [43, 44].

1.1.1 Annealing methods

For many applications such as BCP nanopatterning, BCP thin films are required. When spin casting a BCP thin film on a substrate, the system becomes kinetically trapped and the obtained film will be in a disordered non-equilibrium state. By playing with the mobility of the polymer chains, the predicted equilibrium structures found from bulk melts can be adopted onto the surface with ordered domains [45]. Two of the most common ways to enhance chain mobility and improve the ordering is by doing thermal- and/or solvent annealing. During thermal annealing, the BCP is heated close to or above the glass transition temperature (T_g) to induce microphase separation. However, thermal annealing often requires long annealing times and high-temperature annealing can lead to degradation or chain scission. In solvent vapor annealing (SVA) solvent molecules are introduced into a chamber and absorbed by the BCP which reduces the diffusive energy barrier and thereby promotes the ordering [45, 46]. SVA is a complex method and a comprehensive understanding of how the final structure is formed has still not been established. Many parameters, such as vapor pressure [47], solvent uptake [45, 48] and solvent desorption [48] will affect the ordering of the final state. Additionally, different solvents and solvent

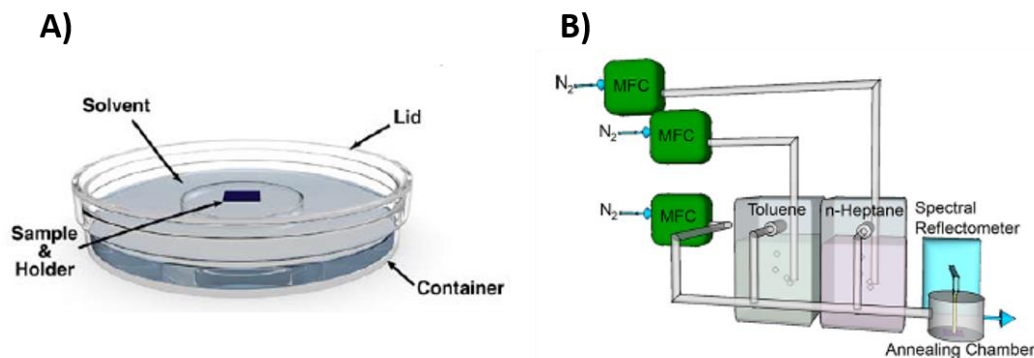


Figure 2: Two different SVA setups. A) SVA chamber is petri dishes put together to obtain a closed chamber wherein solvent is placed. Adapted from [4]. B) SVA chamber wherein saturated vapor streams of toluene and heptane is introduced while the process is tracked in situ through a spectral reflectometer. Adapted from [10].

mixtures will show different selectivity towards the blocks in the BCP and influence the morphology by slightly shifting the block volume fraction [10, 49, 50]. The types of SVA chambers span from simply closed chambers, like the one seen in Figure 2A, to more complex systems, wherein the aforementioned parameter, can be controlled and the evolution of the system during the process can be monitored simultaneously, see Figure 2B [4, 10, 45].

Thermal annealing and SVA are often combined under names such as thermo-solvent [46] or solvothermal annealing [45]. This combination opens a wider parameter space wherein the BCP morphology can be tuned. Other ways to promote the self-assembly of BCPs include electric fields [51] and laser writing [52].

1.2 2D materials

2D materials are atomically thin materials whose existence was first discovered experimentally, by mechanically ripping the layered crystal material, graphite. This resulted in flakes consisting of multi- and monolayers of graphite commonly known as graphene [53, 54]. Since then, the field of 2D materials has expanded tremendously and many other materials including, hBN, MoS₂ and other transition metal dichalcogenides (TMDs) have been added to the 2D material library [16]. The popularity of 2D materials is owing to their unique properties, which opens huge potential in e.g. electronic devices [15, 30, 55, 56], separation technologies [18, 57] and for studying exotic physical phenomena [58, 59]. Graphene and hBN are two very promising 2D materials for such technologies and will be described in the following section together with the combination of the two into van der Waals (vdW) heterostructures.

1.2.1 Graphene

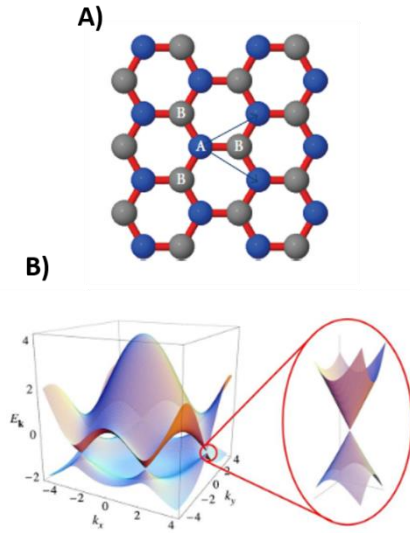


Figure 3: A) Crystal structure of graphene. The unit cell contains two carbon atoms (A) and (B) which each has 3 neighboring carbon atoms. Adapted from [3]. **B)** The electronic band structure found in graphene. The zoom in show an energy band close to a Dirac point. Adapted from [7].

As illustrated in Figure 3A, carbon atoms forming a hexagonal lattice in a 2D plane build up the crystal structure of graphene. Each carbon atom shares three σ -bonds formed by sp^2 -hybridised orbitals with neighboring carbon atoms. These bonds are responsible for a fracture strength of 130 GPa found in graphene [60]. The last p-electrons become hybridized π -bands, which are delocalized over the whole structure. These bands, give rise to graphene's remarkable band structure seen in Figure 3B and are responsible for its high carrier mobility found at RT [61]. Besides showing peculiar mechanical and

electronic properties, graphene also shows very high thermal conductivity [62] and is completely impermeable to any gases [63].

Graphene can be obtained in many ways and is often synthesized by chemical vapor deposition (CVD) or molecular beam epitaxy (MBE). These methods are advantageous since they provide higher control over the layer thicknesses and lateral size in comparison to the exfoliation method. For applications such as electronic devices, high-quality graphene is needed to achieve the best performance. Despite improvements in the before-mentioned synthesis approaches, mechanical exfoliation of layered graphite crystals remains the best way to obtain high-quality graphene [64].

A big challenge in the field of graphene is the fact that it is a semimetal and therefore not useful in electronics unless it is modified so that a band gap is introduced. A band

gap opening can be achieved through e.g. moiré superlattices [65, 66] or nanostructuring [15, 67, 68]. Quantum confinement effects introduce a band gap opening in graphene nano-structures such as a graphene nanoribbon (GNR) [55, 69] and a graphene nanomesh (GNM)/antidot lattice [9, 15, 68].

Standard graphene devices have for long been using SiO_2 as their primary dielectric substrate. However, graphene does not exhibit its expected carrier charges, when placed on SiO_2 , due to scattering from charged surface states, impurities and surface roughness [21, 70]. This problem was solved by placing graphene on another 2D material, known as hexagonal boron nitride (hBN) [22].

1.2.2 Hexagonal boron nitride

Hexagonal boron nitride is an isomorph to graphene with a sublattice containing alternating boron and nitrogen atoms, see Figure 4A. Just like graphene, it shows covalent bonds in the in-plan sheet structure while weak van der Waals (vdW) interactions dominate in-between layers of two or more sheets. Because of the difference in the on-site energies of the boron and nitrogen atoms, it is an insulator with a wide band gap (5.5-6 eV) [71]. Additionally, it presents high heat resistance, high thermal conductivity and a fracture strength of approximately 70 GPa which does not decrease as layer thickness increases, in contrast to graphene [72, 73].

High-quality and significant lateral-sized hBN sheets are challenging to obtain. Large area hBN sheets have been prepared on different substrates using CVD, high-pressure or high-temperature techniques [1]. However, due to high synthesis temperatures and different gas exposures, problems with thickness uniformity and defect creation often arises [74]. Just like graphene, mechanical exfoliation from bulk hBN crystals provides high-quality flakes but with a higher concentration of small flake sizes compared to that of graphene.

hBN is a promising candidate for robust both liquid and gas separation membranes since it presents a chemically inert surface, high corrosion resistance and high thermal stability [57, 75, 76]. Additionally, its atomically flat surface can suppress the ripping of graphene and its popularity rose when it was realized that it would be the ideal dielectric substrate for graphene- and later MoS₂-based devices [16, 22]. The development of suitable transfer methods, such as wet- [77] and dry transfer [78], described in detail later in section 5.2.3, lead to the encapsulation of graphene between two hBN flakes, gave birth to the field of van der Waals (vdW) heterostructures.

1.2.3 Van der Waals Heterostructures

The stacking of different 2D materials on top of each other results in the production of artificial materials with atomic layer precision called van der Waals heterostructures [16]. In these materials, the layer arrangement can be designed such that new or improved properties can arise and even pre-patterned layers can be stacked together [65, 79-81]. VdW heterostructures are usually made manually from

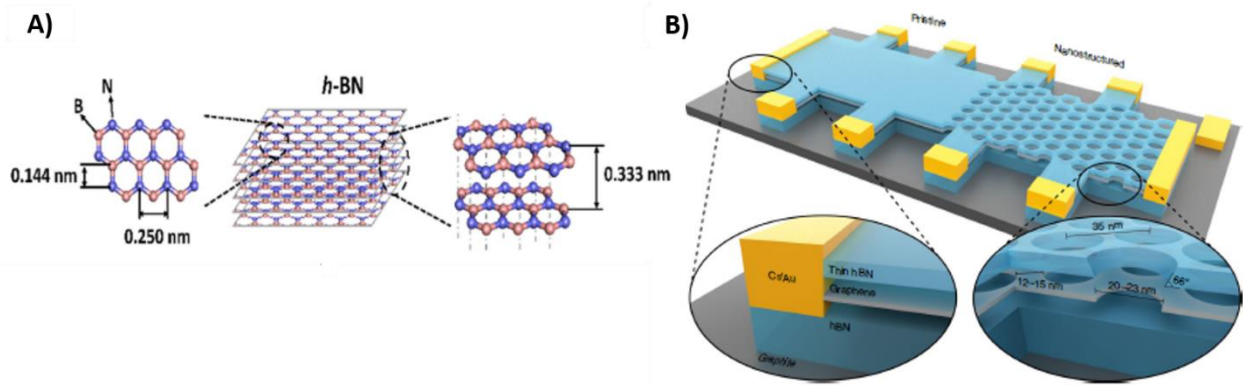


Figure 4: A) Illustration of the monolayer and bilayer crystal structure of hBN. Adapted from [1]. B) hBN/graphene/hBN hall bar device where half of is nanopatterned. Adapted from [9].

stacks of mechanically exfoliated 2D materials flake, since the transfer and integration of largely grown 2D materials into vdW heterostructures is tricky [16, 74].

Flakes of hBN are often employed in vdW heterostructures as a substrate, a protection cover from the environment or for full encapsulation of other 2D materials [9, 81]. Using hBN as a substrate for graphene gives rise to so-called moiré superlattices due to a lattice mismatch between the two crystal structures. With the formation of the moiré superlattice, the graphene band structure presents moiré minibands and a band gap opening at charge neutrality [65, 66].

Full encapsulation of graphene in hBN flakes has proven to consistently enable high-quality devices, which over time, are not influenced by ambient conditions. Additionally, as seen in Figure 4B, band engineering of graphene through nanopatterning of hBN/graphene/hBN heterostructures has shown great promise for future hBN encapsulated graphene devices [9].

2 Block copolymer nanopatterning

The semiconductor industry has shown significant interest in the self-assembly of BCP thin films because of its immense potential as a template material for creating large-scale nanopatterns with sub-10 nm dimensions. [13, 27]. However, BCP self-assembly and nanopatterning go beyond the semiconductor industry and can also be used e.g. in separation technologies [23, 82, 83] and energy devices [84-86]. This chapter will go through a typical BCP nanopatterning process for the production of BCP templates that can be used for manufacturing nanodevices. We further show how directed self-assembly can improve pattern quality and reduce defects by increasing pattern control. This will be followed by a section on a specific high- χ BCP, PS-*b*-PDMS which is often used in nanopatterning processes and lastly some details on how BCP nanopatterning has been used on 2D materials are presented.

2.1 The block copolymer nanopatterning process

BCP nanopatterning is a very versatile nanofabrication technique because of the large variety of well-defined periodic nanostructures that can be obtained with characteristic feature sizes ranging from 5-100 nm. For many years, nanopatterning using BCP self-assembly has been driven by the intense interest in downscaling feature sizes in the semiconductor industry. In such applications, highly ordered spheres, cylinders and lamellas are of prime interest and good control of the BCP nanopatterning process is required to obtain highly ordered patterns with a limited defect amount [86]. One way to achieve this is by doing directed self-assembly which will be discussed in the next section.

With the new developments in nanotechnology, the demand for nanopatterning has spread to other applications such as sensors [83], membranes [23, 82], catalysts [84, 85] and optical devices [56]. Many of these applications do not require the same high amount of control of the nanostructures and defectivity [86].

There are four different strategies for designing nanodevices using BCP self-assembly. These include sequential infiltration synthesis (SIS), BCP co-assembly, microphase-separated BCPs and BCP templating [87]. The latter is the most commonly used strategy where the BCP nanopatterning process includes the following steps shown in Figure 5.

First, the BCP thin film is deposited from a solution onto the target substrate, which may have been functionalized with e.g. a polymer brush layer prior to this step. This is usually done by spin coating, however, other techniques such as dip and spray coating can also be employed [45]. In the second step, the microphase separation is triggered by an annealing procedure as described in section 1.1.1. For applications where a long-range ordering is, required different strategies such as DSA or top-coats can be applied. The third step includes the selective etching of one of the blocks and the subsequent transfer of the obtained BCP template pattern into the target

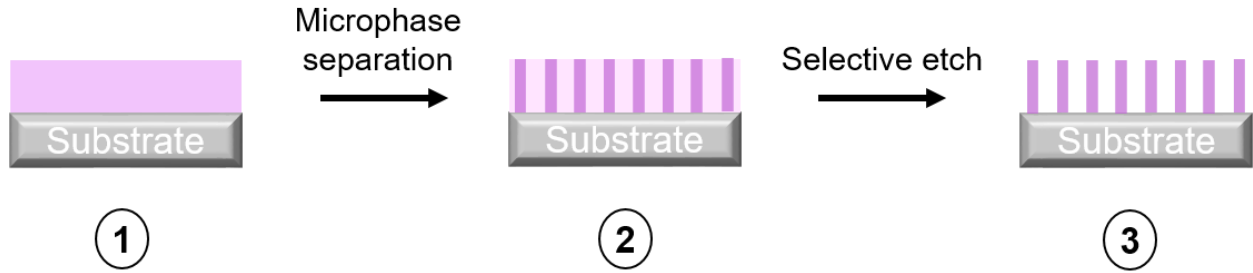


Figure 5: Schematic of a typical BCP nanopatterning process. **(1)** The BCP thin film deposition. **(2)** The microphase separation. **(3)** The selective etching of one of the blocks.

substrate. The etching and pattern transfer are commonly done through a dry reactive ion etching (RIE) process [35, 45, 86].

For many years, polystyrene-*block*-poly(methyl methacrylate) (PS-PMMA) has been the current standard for BCP nanopatterning processes since the understanding of thin film physics, materials design and processing was already well-established. However, PS-PMMA lacks two of the most essential properties for BCP templating, a high etch selectivity and a high- χ parameter which limits its use, especially for applications where small feature sizes are required [35]. This initiated a search for new BCPs that could generate feature sizes on the sub-10 nm scale. These dimensions can be achieved together with reduced pattern defects through high- χ BCPs such as polystyrene-*block*-polylactide, polystyrene-*block*-poly(x -vinylpyridine) and polystyrene-*block*-polydimethylsiloxane (PS-*b*-PLA, PS-*b*-P_xVP ($x = 2$ or 4) and PS-*b*-PDMS) [39, 88].

2.1.1 Directed self-assembly

Directed self-assembly (DSA) secures a higher control of the BCP self-assembly process which is required for some technologies. Two of the main ways to do DSA, are either by graphoepitaxy or epitaxial self-assembly (sometimes referred to as chemoepitaxy) [5, 89], both illustrated in Figure 6. The epitaxial self-assembly of

BCPs utilizes that the substrate is chemically patterned in particular areas to define an affinity towards one of the blocks in that exact area and hereby guide the self-assembly and orientation. However, obtaining a pattern that is commensurate with the BCP morphology often requires high-cost lithography techniques e.g. e-beam lithography or scanning probe lithography (SPL) which limits large-area nanofabrication [5].

The second approach, graphoepitaxy, guides the self-assembly through pre-defined topographic patterns in/on the substrate. Because of the topographic confinement caused by the trench sidewalls, the patterning area is limited to the width of the trench. The topographic guiding patterns can be prepared by various techniques, here among conventional photolithography, making this approach more feasible for up-

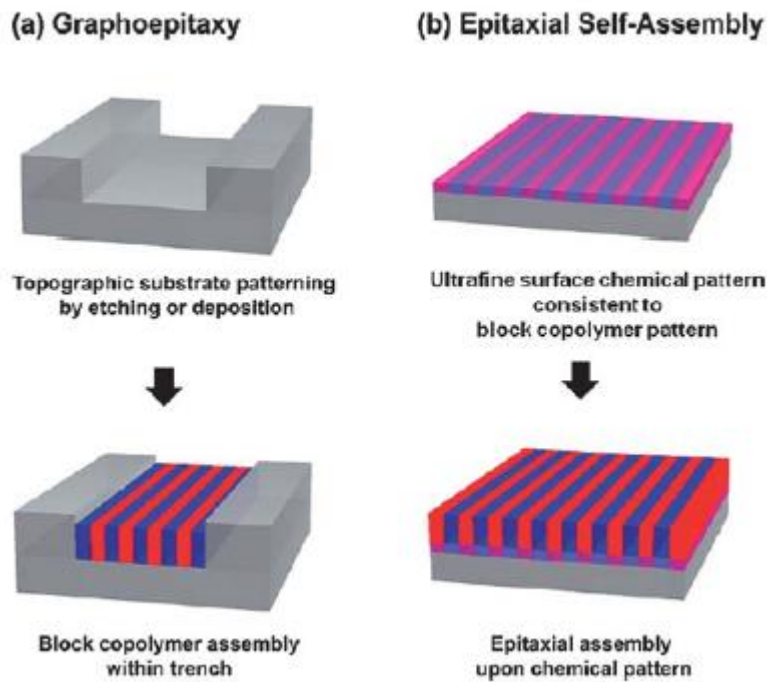


Figure 6: Schematic of the two different DSA methods. A) Graphoepitaxy use topographic guiding patterns to guide the self-assembly of the BCP. B) Epitaxial self-assembly also sometimes referred to as chemoepitaxy. Here a pre-defined chemical pattern is used the self-assembly of the BCP. Adapted from [5].

scaling [5]. Many studies have focused on the making of topographic patterns directly in the silicon substrate [39, 90, 91] or in other silicon-containing layers [4, 49]. However, this means that the pre-defined topographic pattern remains even after pattern transfer [5]. Others have used a removable template [55] or what is known as soft graphoepitaxy using a disposable negative tone photoresist confinement [5, 92], to overcome this problem.

Similarly, to epitaxial self-assembly, commensurability plays a key role in the resulting topographic guided structures. Defect-free and highly aligned structures are formed when the trench width is commensurate with the characteristic period length, L_0 . Especially, for sphere- and cylindrical morphologies, the domain period will adjust itself to match a potential slight incommensurate trench width. This means that aligned defect-free structures with n domain rows can be formed in trench widths, L_s in the range $(n - 0.5)L_0 < L_s < (n + 0.5)L_0$ [93].

2.2 Block copolymer nanopatterning using PS-*b*-PDMS

PS-*b*-PDMS is a BCP containing two well-known and very different polymers. Polystyrene (PS) is used as foam and in a lot of packaging while polydimethylsiloxane (PDMS) is used in contact lenses, medical devices, and lubricant oils. In terms of characteristics, PS is stiff with a glass transition temperature, T_g of 110°C which is in big contrast to PDMS which has high chain flexibility with a T_g -125°C [94, 95]. This special nature of the organic and inorganic parts gives rise to the distinct properties found for PS-*b*-PDMS in solution and thin films leading to applications spanning from thermoplastic elastomers to nanopatterning [40, 96, 97].

PS-*b*-PDMS is widely studied for BCP nanopatterning applications because of its high- χ value, providing feature sizes as small as 7.5 nm [20] and its high etch contrast due to the big dissimilarity between the blocks. It is composed of two blocks, the stiff PS and the rubbery silicon-containing PDMS, which show a big difference in surface energies, γ_{PDMS} = 19.9 mN/m and γ_{PS} = 40.7 mN/m. Because of this, PDMS

preferentially segregate at BCP/air interface creating the structure shown in Figure 7 [40].

The PS block can be selectively removed by an oxygen plasma etch which subsequently will oxidize the PDMS block into a silicon oxycarbide (ox-PDMS) hard template which is thermally stable (up to 700°C) and can act as a patterning template. However, because of the wetting layer at the BCP/air interface, an additional plasma exposure step (CF_4 , CHF_3 , SF_6), to remove the top PDMS is, always reported as a default step in the BCP nanopatterning procedure for PS-*b*-PDMS since an oxygen etch alone, will fail to produce sharp domain patterns [39, 41].

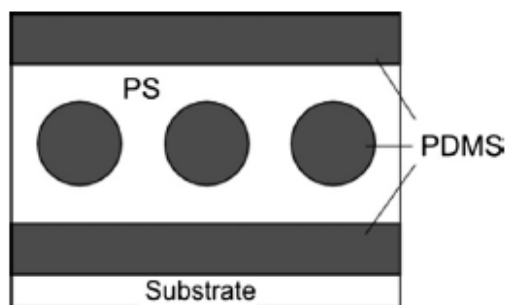


*Figure 7: Illustration of the cross-section of a cylindrical forming PS-*b*-PDMS film on a substrate. Due to the big difference in surface energies, PDMS creates wetting layers at the substrate/BCP and BCP/air interface. Adapted from [6].*

The PDMS surface segregation is also seen at the substrate/BCP interface for most substrates, except for substrates, which are selective towards PS e.g. a PS-brush functionalized substrate. For native silicon, an undulating wetting layer at the substrate/BCP interface has been reported and is believed to be caused by a near-neutral surface i.e. the surface does not favor either PS or PDMS [6].

The versatility and robustness of the ox-PDMS template have been demonstrated for BCP nanopatterning of chromium (Cr), silicon nitride (SiN) and aluminium indium phosphide (AlInP) which makes it a promising candidate for patterning of industrially valuable substrates [91, 98].

2.3 Block copolymer nanopatterning of 2D materials

Tuning the optical and electrical performances of 2D materials is well-known to be accessible through nanopatterning. Devices made of 2D materials and their heterostructures are mostly nanopatterned by electron beam lithography on a lab scale [9, 81, 99]. However, as 2D materials research is becoming more interesting for different commercial industries, research on the implementation of a scalable low-cost method, such as BCP templating, for nanopatterning of 2D materials has been thriving [15, 20, 25, 55, 56, 58, 67, 90, 100, 101].

There are several studies on the nanopatterning of graphene into graphene-nanoribbons [55, 90, 101-103], quantum dots [56, 58] and nanomeshes [15, 67] and only a few on nanopatterning of MoS₂ [20, 25]. Common for these studies is that they do the BCP nanopatterning process on smooth surfaces such as substrates with CVD grown 2D material sheets or mechanically exfoliated flakes with a top protection layer e.g. evaporated SiO₂ or a polymer brush. Because of this, either the final device quality or the BCP process (by adding additional processing step(s)) is compromised.

The first studies using BCP nanopatterning to structure graphene used PS-*b*-PMMA but more recently other BCPs such as PPC-*b*-PS [104], P2VP-*b*-PS-*b*-P2VP [101] and PS-*b*-PDMS [58, 90, 103] has been applied. BCP nanopatterning on graphene and MoS₂ using PS-*b*-PDMS has shown great potential, but often the final device performance is limited by the remaining challenges concerning, the stripping of the PDMS hard template, removal of polymer residues and uniform pattern transfer into few atomic layered materials [103]. Similar challenges have been found for BCP nanopatterning of 2D materials utilizing DSA methods which often adds undesired additional steps to the nanofabrication process [20, 55, 89].

BCP self-assembly on 2D materials has most been concerned with BCP templating for nanopatterning of 2D materials for various device applications. However, researchers are using other BCP self-assembly strategies, such as SIS and BCP co-assembly, in combination with 2D materials. In SIS, the BCP nanopatterned

template is turned into metal sulfides such as MoS_2 through e-beam physical vapor deposition [28] while in BCP co-assembly, inorganic nanoparticles such as TMDs and graphene are incorporated into the bulk BCP solution to yield ordered nanostructures of inorganic nanoparticles with BCP microphase separation [87, 105, 106]. Since this thesis will only concern BCP nanopatterning using the BCP templating strategy, the aforementioned strategies are not further covered here.

3 Anionic polymerization of PS-*b*-PDMS

The following chapter covers the synthesis and molecular characterization of the BCP, PS-*b*-PDMS performed at DTU Chemistry. For simplification, the PDMS chain is sometimes described as $M-D_i-D_j-[D]_m-D_j-D_i-M$ where D represents $[-Si(CH_3)_2O-]$ labelled D_m for the ones in the PDMS backbone, M denotes the terminal $-Si(CH_3)_3$ groups and D_i and D_j is the siloxanes which are 1 and 2 spaces, respectively, from the terminal M. The terminal M group will sometimes be denoted M^{OH} which represents a $-Si(CH_3)_2OH$ terminal group. The junction between PS and PDMS, $-CH-Si(CH_3)_2-O-$ is denoted J and the nearest neighbor to the PDMS side is denoted J_i . An illustration of the notation is found in Figure 8.

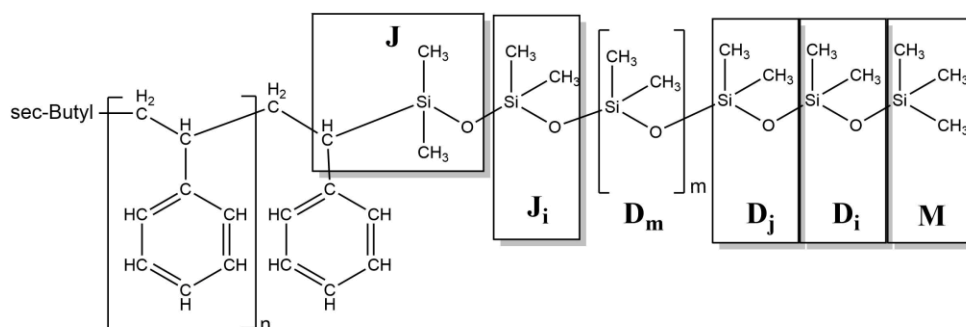


Figure 8: Illustration of the notation used for PS-*b*-PDMS.

3.1 Introduction

Polystyrene-*block*-polydimethylsiloxane (PS-*b*-PDMS) is a promising block copolymer (BCP) for BCP nanopatterning, due to its high- χ value and excellent etch contrast. For BCP nanopatterning, the use of homogenous and narrow molecular weight distribution BCPs is often necessary to obtain the best possible pattern control and -quality. The best way to achieve such BCPs is through living polymerization. Living polymerization includes, among others, anionic- and cationic polymerization which only differ from each other based on the character of their reactive intermediates [97]. The ideal living polymerization is carried out with no side reactions of the

propagation “living” polymer and with an initiation rate greater than the propagation rate. To ensure no spontaneous termination, the polymerization is done in the absence of possible terminating impurities (H_2O , O_2 etc.) [107, 108].

Anionic polymerization using organolithium (RLi) reagents has long been known to synthesize homopolymers of PS [107-110] and PDMS [97, 111-114] from the monomers styrene and hexamethylcyclotrisiloxane (D_3) respectively. Especially, the polymerization of D_3 into PDMS has been discussed due to the challenges in the initial ring-opening polymerization where the cyclic siloxane monomer is cleaved into linear siloxane segments [112-115]. Previous studies have reported the reaction between RLi reagents and D_3 in a hydrocarbon solution. They found that the rate of the ring opening of D_3 was much slower than the following alkylation reactions and after termination with chlorotrimethylsilane (CTMS), the major product was $\text{Bu}(\text{D}_1)\text{Si}(\text{CH}_3)_3$ (D_1 representing a single $[-\text{Si}(\text{CH}_3)_2\text{O}-]$) with a substantial amount of unreacted D_3 . They further claimed that the D_3 does not polymerize before the addition of a donor solvent (promoter) such as diethyl ether, dimethyl sulfoxide (DMSO), or tetrahydrofuran (THF) [112, 114, 116]. Furthermore, at D_3 conversion higher than 85%, the PDMS chains start to get attacked by their living ends due to the reduced amount of monomer. These backbiting reactions create cyclic silicone oligomers (D_4 or higher) [117]. The role of the promotor is to increase the propagation rate and reduce the possibilities of such side reactions [115]. Other ways to avoid backbiting reactions include early termination (at D_3 conversions <85%) [94, 114, 116].

The BCP, PS-*b*-PDMS was first synthesized by sequential anionic polymerization with D_3 [96]. Here a sequential addition of monomers, styrene, and D_3 in cyclohexane with $n\text{-BuLi}$ as the initiator was reported. Since then, minor adjustments to the synthesis parameters have been made concerning the reaction temperature and reaction time of the crucial step when adding D_3 to the living polystyryllithium (PSLi^+). The following polymerization propagation is kept at low temperatures for 3-7 days [31, 95, 118, 119].

The most common characterization methods for synthesized PS-*b*-PDMS include size-exclusion chromatography (SEC) and liquid nuclear magnetic resonance (NMR). From SEC, the molecular weight averages of the BCP can be determined together with the polydispersity index (PDI) and the presence of residue monomer. This is done in relation to a calibration curve usually made from measuring commercially available monodisperse homopolymer standards, which is not ideal for BCP analysis [120]. Additionally, when doing SEC on PS-*b*-PDMS, the presence of homopolymers can slur the actual picture of the sample and it can be difficult to determine how much is a homopolymer and how much is BCP [94, 96]. Furthermore, SEC is an environment-sensitive and time-consuming process since a calibration curve is needed, ideally, every time samples are measured [121].

For NMR experiments, the most common ones are the 1D ^1H - or ^{13}C -NMR where proton- or carbon nuclei present in the sample, are recorded and represented in a 1D spectrum with the (frequency) chemical shift as the x-axes and the intensity as the y-axes. ^1H -NMR is convenient and fast with measurement times being less than 10 min, even for polymers. From a ^1H -NMR spectrum, the presence and mole fractions of PS, PDMS, and monomer residues are rather easy to observe [122, 123]. Additionally, depending on the end-group, the number average molecular weight (M_n), can be calculated by end-group analysis. For BCPs, it has not been customary to find the M_n this way and the method is believed to be restricted to $M_n < 20$ kg/mol due to decreasing sensitivity with increasing chain length reducing the end-group signal [121]. Another drawback, especially for PS-*b*-PDMS is that it is nearly impossible to distinguish between a PS/PDMS homopolymer blend and a PS-*b*-PDMS BCP only by ^1H -NMR due to the overlap of the signals from nuclei in PDMS in slightly different chemical environments [124].

Special for PDMS is that it contains silicon and hence ^{29}Si -NMR experiments can help determine the microstructure of silicon-containing polymers as reported before [125]. For ^{29}Si - and ^{13}C -NMR a wider chemical shift range is found compared to ^1H -NMR, providing less overlap and therefore a better chemical environment determination.

However, the signal sensitivity herein signal-to-noise-ratio depends on the gyromagnetic ratio (γ), which describes the rotation of a charged particle and is different from each nucleus. For ^{13}C and ^{29}Si this value is low compared to ^1H resulting in recording times being hours or sometimes even days, especially for polymers due to the longer relaxation times [126].

Another way to gain knowledge about the microstructure is by looking at the connectivity of chemical bonds through the observation of spin-spin coupling, which is the interaction between nuclear spins. This can be done through 2D NMR experiments where the resulting spectrum is represented in a 2D contour map with (frequency) chemical shifts, of each nucleus measured, as the horizontal and vertical axes. With these experiments, the coupling between nuclei, one, two, or three bonds away from each other can be seen and can help to describe the structure conformation [126]. Heteronuclear multiple bond correlation (HMBC) is a 2D NMR experiment where the correlation between nuclei of different types separated by two or three bonds is investigated. In such an experiment, nucleus, X (often ^1H) transfers its magnetization to nucleus Y, which then returns it to nucleus X before another pulse hits and by that the correlation between X and Y can be investigated [127].

The literature concerning the structural determination of PS-*b*-PDMS with 2D NMR is sparse although its huge potential especially after fast multidimensional experiments can be implemented on most instruments [122, 128]. This chapter will investigate the anionic polymerization of PS-*b*-PDMS mainly through ^1H -NMR and a ^1H - ^{29}Si HMBC NMR experiment based on the acceleration by sharing adjacent polarization (ASAP) method [128] to highlight its potential for silicon-containing BCPs. The findings are compared to SEC results to validate the potentials and possible limits of this ^1H - and ^1H - ^{29}Si HMBC NMR method.

3.2 Experimental

3.2.1 Materials, setup and purification

The synthesis of PS-*b*-PDMS was done through sequential anionic polymerization in a setup similar to the one used in [129]. All glassware was flame cleaned under a vacuum prior to their usage. HPLC grade solvents, cyclohexane (CHX) and tetrahydrofuran (THF) were purified, first by passing it through an Al₂O₃ column into a cleaned round bottom flask under argon flow. Sodium in paraffin was added to THF and it was put up for reflux. Afterwards a small amount of benzophenone was added and the characteristic dark blue/purple color of anhydrous THF was seen. CHX was put up for reflux and later a small amount of styrene and n-BuLi (1.6M in hexane) was added to verify the purity.

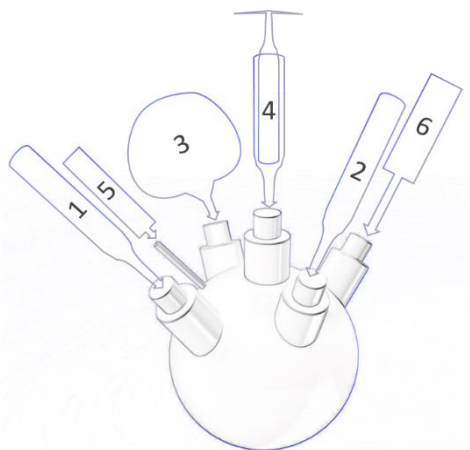


Figure 9: Illustration of the reactor with 6 necks. 1 and 2 represents the two monomer ampoules, 3 is the THF flask and 4 is the rubber septum where syringes can be let through. 5 is the thermometer and 6 is the argon/vacuum inlet.

Styrene was poured through an Al₂O₃ column to remove the stabilizer and hereafter further purified. Both monomers, styrene, and hexamethylcyclotrisiloxane (D₃), were stirred over CaH₂ overnight and degassed with at least three freeze-pump-thaw cycles. This was followed by a distillation over Bu₂Mg (1M in heptane) and finally a distillation into precalibrated monomer ampoules. CHX was distilled into the monomer ampoules while THF were distilled into a precalibrated one-neck round bottom flask. All flasks and ampoules were connected to a reactor with the setup as illustrated in Figure 9. Reactor necks with additional connections to; the argon/vacuum inlet (6), a thermometer (5), and a neck closed by a rubber septum used to pass syringes through (4). The reaction was initiated with a newly opened sec-BuLi

(1.4 M in CHX) and nitrogen bubbled CTMS ($\geq 99\%$) or MeOH ($\geq 99.9\%$) was used as terminating agents. The initiator volume, V_I was calculated using

$$V_I = \frac{m}{c_I M} \quad (1)$$

where c_I is the concentration of the initiator, m is the monomer mass and M the desired molar mass of the polymer [129]. Initiation, termination, and taken-up sample aliquots were performed with gas-tight syringes. The temperature was varied along the synthesis as described later in section 3.3.

3.2.2 Nuclear magnetic Resonance

^1H - and ^1H - ^{29}Si HMBC NMR experiments were recorded for structural characterization of the synthesized PS-*b*-PDMS. For the ^1H - ^{29}Si HMBC NMR experiments it is assumed that the different compounds containing Si nuclei in the samples had similar T_2 relaxation because then the measurement of the ^1H - ^{29}Si coupling could be obtained in less than 10 min using the ASAP method described elsewhere [128]. ^{29}Si -NMR was measured for a few samples for comparison to the obtained signals from the ^1H - ^{29}Si HMBC NMR experiments.

The NMR spectra were recorded on deuterated chloroform (CDCl_3 , 7.26 ppm) solutions with approximately 100 mg of BCP sample or on solutions directly taken out of the reaction without the addition of a reference solvent. The spectra were recorded on either a Bruker AVANCE 400MHz or 600MHz at RT or slightly above. ^1H -NMR spectra were used to quantify M_n values and therefore the relaxation delay was set to 10-20s for all ^1H -NMR to ensure full relaxation of all the BCP nuclei. For ^{29}Si -NMR and ^1H - ^{29}Si the delay time was 1.5s. Additionally, the ^{29}Si -NMR was ^1H decoupled to only see the average state of the protons and hence obtain a single signal. The ^1H - ^{29}Si HMBC spectra only show two and three-bond spin-spin couplings between ^{29}Si and ^1H . They are ^1H coupled resulting in a splitting of the signal into a

doublet with the long-range coupling, $^2J_{\text{CH}_3\text{-Si}} = 7 \text{ Hz}$, from the methyl protons and their coupling to silicon.

The program MestReNova was used for data analysis and a baseline was applied to all spectra before integration. A line fitting was used to obtain integral values of signals overlapping significantly with solvent signals e.g. PS signal ($-\text{CH}_2$ and $-\text{CH}$). The ratios of PS and PDMS in the samples were determined from the integrated values of the aromatic PS- and the methyl PDMS signals found by proton NMR. End-group analysis was done using ^1H -NMR and ^1H - ^{29}Si HMBC NMR to obtain the number average molecular weight, M_n as described later in section 3.3 based on [120]. Some useful ^{29}Si chemical shift values can be found in [124].

3.2.3 Size Exclusion Chromatography

Chromatography is the most widely used technique for the molecular weight characterization of polymers. Here, size exclusion chromatography (SEC) in which macromolecules in an eluent are separated by their hydrodynamic volume was performed mainly for the comparison with obtained NMR results. The refractive index (RI) intensity from the samples was collected with SEC and the molecular weight averages were found through a conventional calibration based on monodisperse PS standards. The SEC data was obtained on a VISCOTEK differential refractometer/viscometer (only the RI detector was used) with a Nucleosil-300-7-OH column with toluene as the eluent. The flow rate was kept at 0.5 ml/min and the injection volume at 10 or 100 μL . The TriSEC software was used to record the RI signal as function of the retention volume, V_{ret} . Sample solutions of 5-2.5 mg/ml in toluene were prepared. PS standards were used to make a calibration curve ($\log(M)$ vs. V_{ret}) and small amounts of Irganox 1330, mixed in the first and last standard ensured a steady flow. No instrument calibration was done prior to the measurements, meaning the peak broadening, sigma (band broadening) and tau (tailing), were not taken into account. The average molecular weights were

determined from the calibration curve (see example in appendix B1) using the TriSEC software. Below is a description of the different molecular characteristics given from the SEC analysis.

Synthetic polymers are never composed of just one exact chain length and are therefore called polydisperse. This means that the molecular weight characteristics need to be expressed in different ways using e.g. a number average molecular weight (\overline{M}_n), weight average molecular weight (\overline{M}_w) and a higher average molecular weight (\overline{M}_z). \overline{M}_n give the number of molecules of each weight while \overline{M}_w gives the molecular weight based on the weight of the constituting molecules [120]. \overline{M}_z emphasizes large molecules, but is commonly not quoted and will not be reported here. The molecular weight averages and the PDI were found based on the general expressions given here,

Where N_i = # of polymer molecules, M_i = molecular weight and a is either 1, 2, or 3

$$\overline{M} = \frac{\sum N_i M_i^a}{\sum N_i M_i^{(a-1)}} \quad (2)$$

generating the above-mentioned molecular weight averages expressed below,

$$\overline{M}_n = \frac{\sum N_i M_i}{\sum N_i} \quad (3) \quad \overline{M}_w = \frac{\sum N_i M_i^2}{\sum N_i M_i} \quad (4) \quad \overline{M}_z = \frac{\sum N_i M_i^3}{\sum N_i M_i^2} \quad (5)$$

The ratio $\overline{M}_w/\overline{M}_n$ is the PDI which indicates the broadness of a molecular weight distribution [130]. For simplification, \overline{M}_x will in the following be denoted M_x .

3.3 Results and discussion

A basic reaction scheme for the anionic polymerization of PS-*b*-PDMS is presented in Figure 10. The synthesis took place under argon and was started with the initiation of PS with sec-BuLi in CHX and proceeded for 12-22 h in order to ensure full conversion to the living PSLi⁺, shown as 1. step in Figure 10. This was followed by step 2, which was the addition of D₃ in CHX, left until the orange color from PSLi⁺ was gone, indicated by a solution color change into a milky white color. In this step, a ring opening of D₃ takes place together with a set of alkylation reactions as

described by others [112]. At RT, this took at least 6 h hence the reaction was typically left overnight. For two samples, this took place at 50°C and the reaction time was shortened to 1.5 h. In step 3, THF was added in order to promote the polymerization of the ring-opened D₃. The ratio between CHX and THF was approximately 1:1. The reaction was left for 2 h at RT before being placed in an ethylene glycol bath, and chilled to 0°C or -16°C for 3-4 days. Lastly, in step 4, the reaction was terminated with CTMS. In Table 1 some specific synthesis parameters for the different syntheses can be found. The concentration of D₃ in the 1:1 CHX and THF mixture was for all synthesis kept at around 5% (w/w). A PDMS volume fraction between 0.25-0.35 was strived for while the desired molar mass was determined by the amount of initiator through eq. (1).

*Table 1: PS-*b*-PDMS synthesis details*

| Sample | PS polymerization time [h] | Temperature D ₃ ring-opening [°C] | Lifetime of PSLi ⁺ color after D ₃ addition [h] | Temperature D ₃ in CHX and THF [°C] | Total reaction time [h] |
|--------|----------------------------------|----------------------------------------------------|-----------------------------------------------------------------------------|------------------------------------------------------|----------------------------|
| SD42 | 17 | 21 | 24 | 0 | 113 |
| SD108 | 12 | 21 | 6 | 0 | 110 |
| SD64 | 20 | 50 | 1.5 | -16 | 96 |
| SD19 | 22 | 50 | 1.5 | -16 | 120 |
| SD38 | 18 | 21 | 24 | 0 | 114 |

Scheme 1

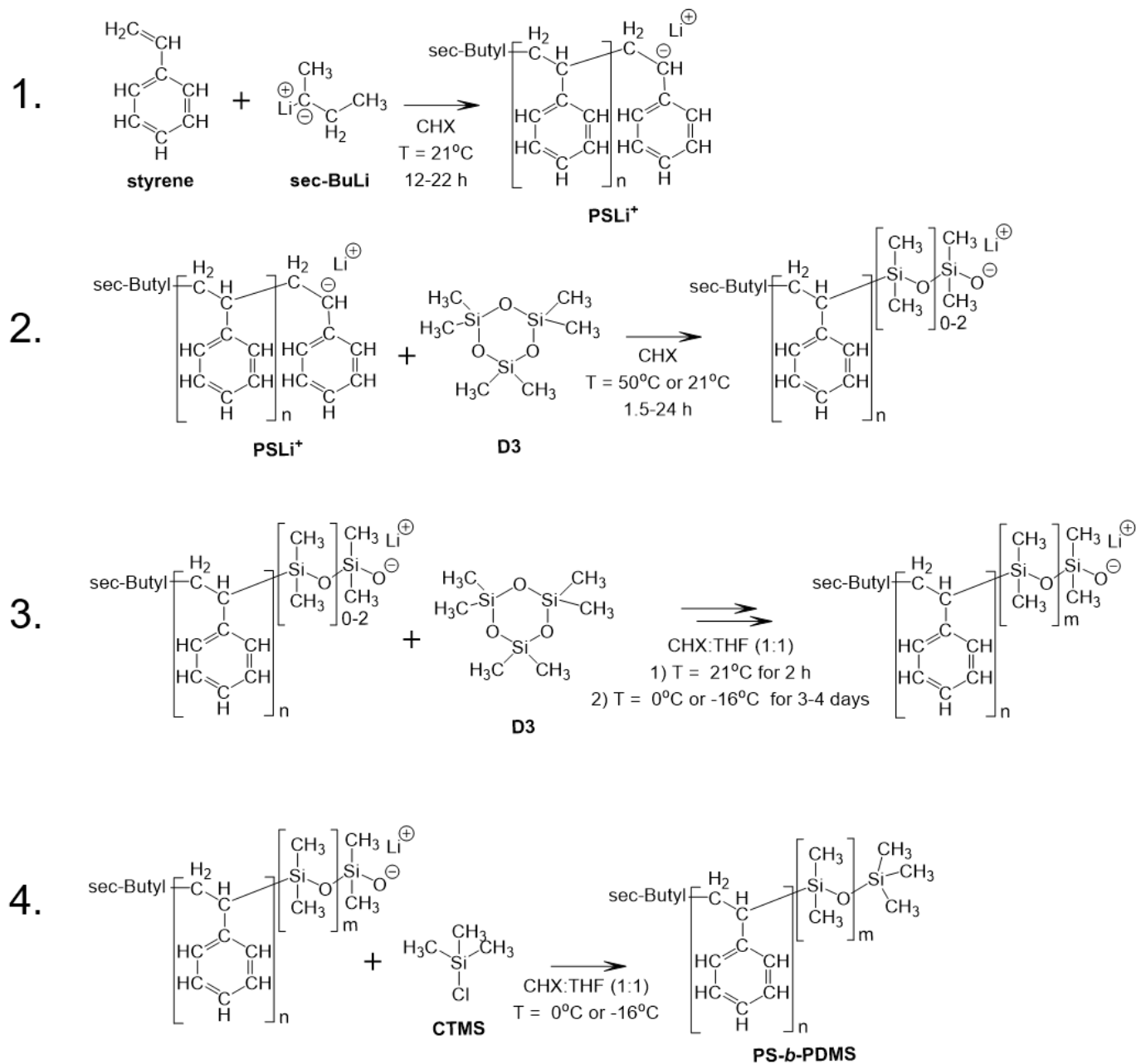


Figure 10: Reaction scheme for the anionic polymerization of PS-*b*-PDMS. For further details, the reader is referred to the main text.

3.3.1 ^1H -NMR analysis

For all syntheses, no excess styrene was found in the ^1H -NMR analysis, meaning the PS polymerization time had been sufficient to achieve full conversion of styrene to PS. However for SD64 and SD19 a shoulder at low retention volume in the RI signals from an aliquot of the PS polymerization was observed, see Appendix B2 or later in Figure 17. This phenomenon has been observed before in the polymerization of PS but has never been given much attention [118]. It could be caused by a dimeric coupling which can be formed in the presence of oxygen. The oxidation of PSLi^+ can give rise to a diverse array of products e.g. with alcohol and ketone chain-end functionalization [131]. This claim could be supported by the broad singlet resonances found in ^1H -NMR around $\delta^{\text{H}} = 4.7$ ppm which indicates a $-\text{OH}$ group. In appendix B3, a ^1H NMR spectrum of a PS aliquot showing this is found.

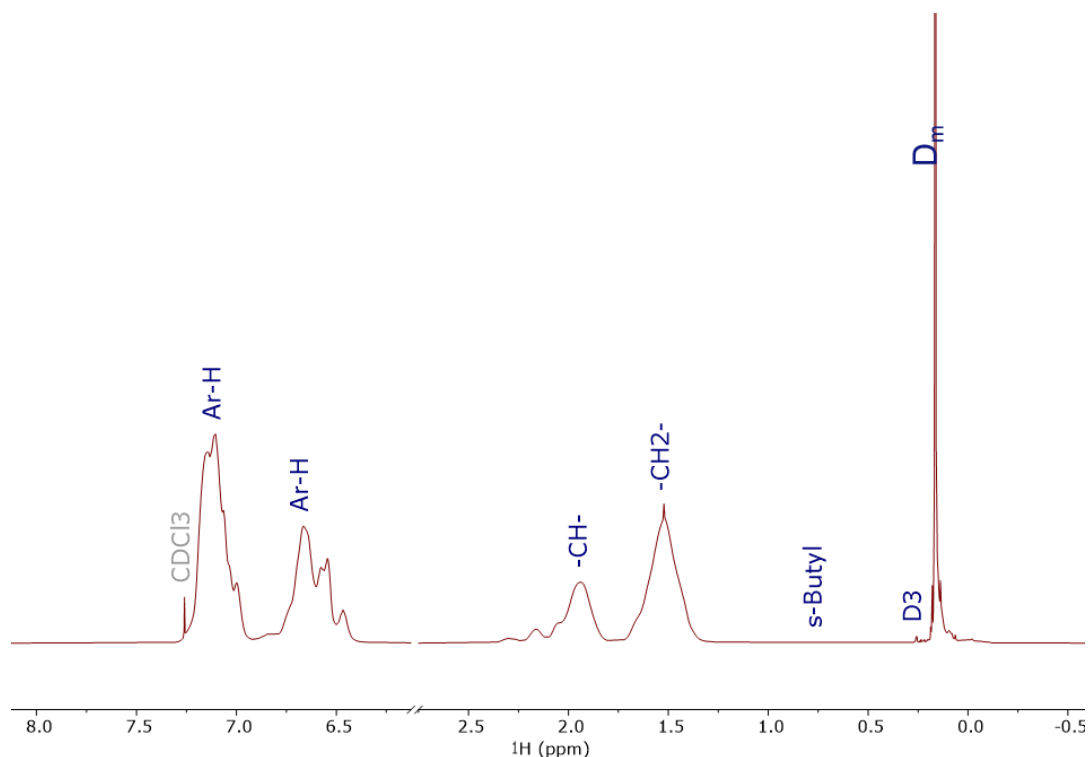


Figure 11: ^1H -NMR spectrum showing the characteristic resonance signals from PS (Ar-H, Ar-H, -CH-, -CH₂-) and PDMS (D_m) together with signals from the end-group s-Butyl and excess D₃. A small signal from CHX is seen overlapping with PS (-CH₂-).

In Figure 11, a typical ^1H -NMR spectrum of a synthesized PS-*b*-PDMS taken at 600MHz is shown. The signals labelled Ar-H, -CH-, -CH₂- belong to protons from PS while the signal labelled D_m is from the protons of the methyl groups in the siloxane backbone of PDMS. The signals labelled Ar-H and Ar-H belong to the protons of the aromatic rings, containing 3 and 2 protons respectively. The next signal (-CH-) and the following bumps ($\delta^{1\text{H}} = 1.7\text{-}2.3$ ppm) come from the proton of the tertiary carbon while signal -CH₂- is from the protons of the secondary carbon. These signals often contain signal overlaps from THF and CHX. Signal s-Butyl is two broad bumps from the protons of the end-group containing two methyl groups from sec-BuLi. The small signal around $\delta^{1\text{H}} = 0.26$ ppm indicates the presence of D₃ while the broadness of a small peak/shoulder found on the right side of the D_m signal indicates it comes from protons in a PDMS chain. However, it is well-known that siloxane sites close to the terminal sites in PDMS (D_i, D_j) give rise to individual signals and therefore create an overlap in this area [125]. Due to this large overlap of resonances around $\delta^{1\text{H}} = 0\text{-}0.32$ ppm, it is almost impossible to assign these only from ^1H -NMR and it further complicates the conclusion on rather PS-*b*-PDMS is present or just a PS/PDMS blend. When zooming in on this area, additional satellite signals can be found on each side of the main D₃ and PDMS signal which arise from the coupling to different silicon isotopes (^{28}Si , ^{29}Si and ^{30}Si).

The line widths found in the ^1H -NMR spectrum are much broader for the PS signals than the PDMS. This indicates that PS is more rigid than PDMS and has a longer T_2 relaxation (T_2^{nuclei}) since the full width at half maximum (FWHM) of a signal is found by $FWHM = \frac{1}{\pi T_2'}$ where $\frac{1}{T_2'} = \frac{1}{T_2^{\text{nuclei}}} + \frac{1}{T_2^{\text{instru}}}$. Here T_2^{instru} is the instrument (inhomogeneity and instability of the field) contribution to the line width. By looking at the linewidths of the different nuclei in the samples (e.g. in CTMS, D₃ and PDMS), a similar FWHM is found for CTMS, D₃ and PDMS, all are around 1.5-1.9 Hz. This justifies the assumption that the T_2 relaxation is similar for the silicon-containing compounds and hence the ^1H - ^{29}Si HMBC NMR experiment can be used for this system, which will be shown in sections 3.3.2 and 3.3.3.

In Table 2 is the results from the ^1H -NMR analysis presented. The PDMS volume fractions (f_{PDMS}) were calculated through the following equation

$$f_{PDMS} = \frac{x_{PDMS} \frac{M_{PDMS}}{\rho_{PDMS}}}{x_{PDMS} \frac{M_{PDMS}}{\rho_{PDMS}} + x_{PS} \frac{M_{PS}}{\rho_{PS}}} \quad (6)$$

where $M_{PDMS} = 74 \text{ g/mol}$, $\rho_{PDMS} = 0.97 \text{ g/cm}^3$ and $M_{PS} = 104 \text{ g/mol}$, $\rho_{PS} = 1.032 \text{ g/cm}^3$ [40]. The mole fractions, x_{PDMS} and x_{PS} were calculated from the ratio between the proton normalized intensities obtained from the ^1H -NMR analysis. An example of how to calculate x_{PDMS} is shown below in eq. (7)

$$x_{PDMS} = \frac{\frac{a_{PDMS}}{n_{PDMS}}}{\frac{a_{PDMS}}{n_{PDMS}} + \frac{a_{PS}}{n_{PS}}} \quad (7)$$

Here $\frac{a_{PDMS}}{n_{PDMS}}$ and $\frac{a_{PS}}{n_{PS}}$ denote the proton normalized integral values for PDMS and PS.

n_x is the number of protons belonging to the integrated value, a_x . For PDMS, the D_m signal was used while for PS, the Ar-H signal containing 2 protons was used since this signal contained no overlap signals with other species.

The number average molecular weight was calculated from the degree of polymerization (DP) with eq. (8) and (9) for each of the blocks, PS and PDMS (PDMS is shown as an example)

$$DP_{PDMS} = \frac{a_{PDMS} \cdot n_{end}}{n_{PDMS} \cdot a_{end}} \quad (8)$$

$$M_{n,PDMS} = DP_{PDMS} \cdot M_{PDMS} + M_{end,y} \quad (9)$$

Here a_x denotes the integral value obtained from ^1H -NMR belonging to the group of interest, $x = \text{PDMS, PS (Ar-H) or end-group}$, and n_x is the number of protons in that given group. The DP_x is then used to calculate $M_{n,x}$ here the $M_{end,y}$ is the molecular weight of the end-group used in the calculation of DP_x . The end group used depends on the NMR spectrum of interest. S-Butyl is usually easy to observe and without any peak overlap while $-\text{Si}(\text{CH}_3)_3$ often is impossible to observe and integrate in ^1H -NMR.

Therefore $M_{end,1} = 30.02$ g/mol, when using s-Butyl in ^1H -NMR and $M_{end,2} = 73.118$ g/mol when using $\text{Si}(\text{CH}_3)_3$ in ^1H - ^{29}Si HMBC.

When calculating the total M_n the DP calculated from PS and PDMS is used as follows

$$M_n = M_{end,1} + (DP_{PDMS} \cdot M_{PDMS}) + (DP_{PS} \cdot M_{PS}) + M_{end,2} \quad (10)$$

The M_n for each block can also be calculated from the total M_n , by multiplying with the volume fraction of the block e.g. f_{PDMS} .

*Table 2: Molecular characteristics of the synthesized PS-*b*-PDMS*

| Sample | $f_{PDMS, NMR}$ | x_{NMR} [%] | PS- <i>b</i> -PDMS $M_n, ^1H-NMR$ [g/mol] | PS- <i>b</i> -PDMS M_n, SEC [g/mol] | PS- <i>b</i> -PDMS M_w, SEC [g/mol] | PDI |
|--------|-----------------|---------------|-------------------------------------------------|---------------------------------------------|---------------------------------------------|-------|
| SD42 | 0.36 | 97 | 32215 | 46600 | 56200 | 1.206 |
| SD108 | 0.26 | 95 | 85940 | 119600 | 188700 | 1.578 |
| SD64 | 0.2 | 83 | 44821 | 64300 | 80400 | 1.25 |
| SD19 | 0.26 | 90 | 24980 | 18700 | 21000 | 1.123 |
| SD38 | 0.28 | 98 | 36058 | 37900 | 41200 | 1.089 |

The obtained D₃ %conversion, found in Table 2, described by the mole fraction of PDMS relative to D₃, x_{NMR} is >80% for all samples. However, for SD64 and SD19 the PDMS yield is a bit lower than for the others which is also reflected in the volume fractions, f_{PDMS} which are a bit lower than expected (should have been around 0.30). This suggests that the D₃ ring opening at 50°C for 1.5 h might not have been long enough to ensure the full opening of all D₃ before the polymerization into PDMS.

The molecular weight obtained from the ^1H -NMR end-group analysis is also presented in Table 2 with a comparison to SEC results. It is seen that the values obtained from SEC are way higher for most of the samples except for SD19 and SD38, which fits nicely. However, these three samples also show a high PDI and hence a broad distribution of different molecular weights which is challenging when doing end-group analysis. Additionally, the reported M_n of SD42, SD108 and SD64 are all approximately twice as high as the desired M_n calculated from the monomer masses

and initiator volume. This can be explained by the presence of impurities, such as water which must have consumed approximately half of the initiator. Additionally, this would also explain the high PDI values seen from these samples.

In general, all the PDI values are overestimated since no calibration of the peak broadening from the instrument was performed. However, SD19 and SD38 both show acceptable PDIs e.g. for BCP nanopatterning applications.

In Figure 12 is the raw refractive index increments shown for each sample. The negative signal at 2.8 mL is from the eluent while the signal in SD42, SD108 and SD64 at 2.2-2.4 mL is from a PDMS homopolymer, which, in toluene, has RI increments of the opposite sign as PS. The presence of the homopolymer creates further uncertainty on the molecular characteristics obtained from SEC since the signals from the homopolymer and BCP slightly overlaps. However, the formation of a PDMS homopolymer further confirms the presence of trace water, which is believed

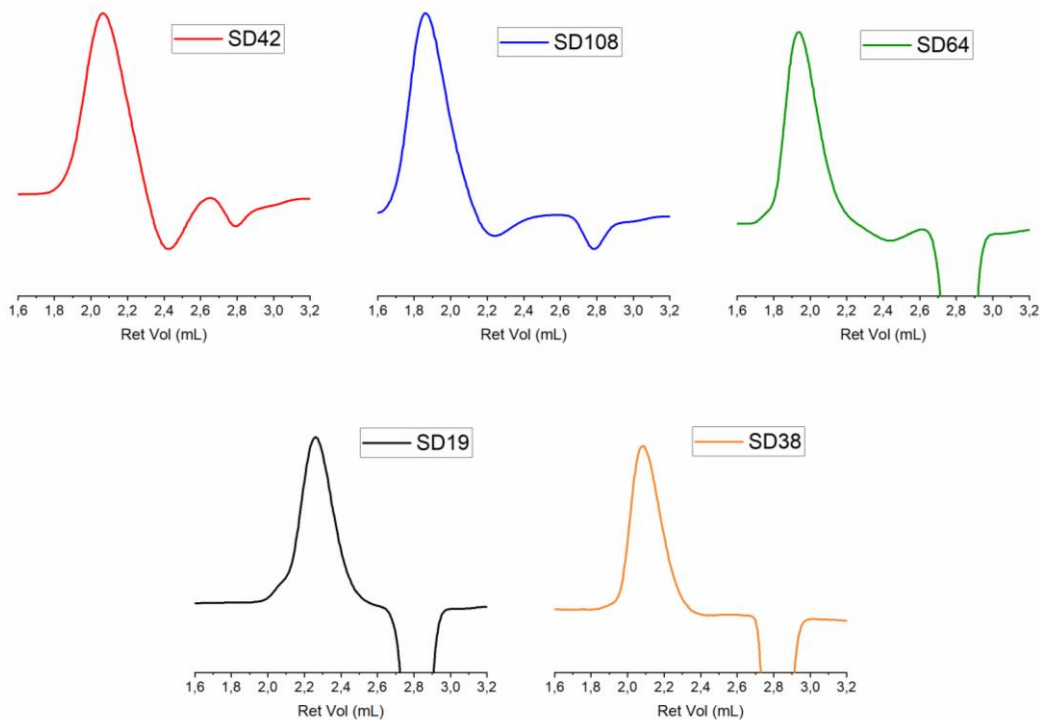


Figure 12: SEC traces of all samples. The negative RI signal at 2.8 mL comes from the solvent, toluene.

to originate from water in the D₃ monomer and result in the formation of siloxane diols that can propagate in both ends [94, 113]. The shoulder at higher retention volume found from PS aliquots of SD64 and SD19 seems to still be present for sample SD19, at approximately 2.1 mL. This indicates the presence of a PS homopolymer, however, due to overlap with the BCP signal this is hard to determine. The removal of impurities and homopolymers will be further discussed in section 3.3.1.

3.3.1 ²⁹Si-NMR analysis

Since ²⁹Si-NMR is very time-consuming because of the signal sensitivity, this measurement was only performed on a few samples, with one shown here. A ²⁹Si-NMR spectrum, which took more than one day to measure, is shown in Figure 13. From this, the different signals from the PDMS block can be assigned and M_n of the PDMS block can be calculated. This can be compared with the results from ¹H-²⁹Si and SEC and give a good idea of how well these experiments align with each other.

In Figure 13, the signal from the PDMS backbone, D_m ($\delta^{29}\text{Si} = -22.15$ ppm) together with two minor signals from the end-group, M ($\delta^{29}\text{Si} = 7.09$ ppm) and its neighboring siloxane, D_i ($\delta^{29}\text{Si} = -21.44$ ppm) are observed. The siloxane groups close to the terminal end (D_i and D_j) show slightly different chemical shifts than the siloxane backbone (D_m), due to the difference in the chemical environment. The signals from D_i and D_j are placed on each side of the D_m signal and in the shoulder on the right side of the D_m signal is the signal from D_j ($\delta^{29}\text{Si} = -22.28$ ppm)

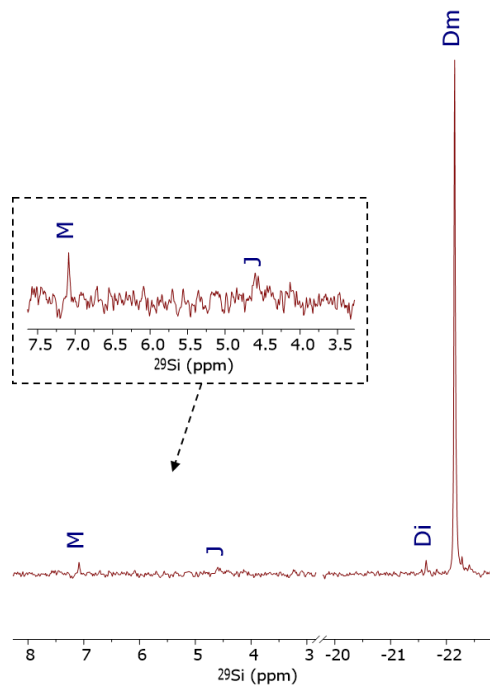


Figure 13: ²⁹Si-NMR spectrum of PS-*b*-PDMS measured on a 600MHz NMR instrument.

found. Additionally, a very small signal from the coupling between PS and PDMS is seen at $\delta^{29\text{Si}} = 4.5$ ppm and its presence was confirmed with the ^1H - ^{29}Si HMBC spectrum found in Figure 14.

A M_n for the PDMS block in relation to the end-group M was calculated from the integrated signals. From this calculation, a $M_n = 5096$ g/mol was found which is in the same order as the M_n found with ^1H -NMR, see Table 3. The M_n for PDMS calculated from ^1H -NMR based on the volume fractions seems to fit the best with the M_n found from ^{29}Si . On the other hand, the M_n found from ^1H -NMR based on the calculated DP for the PDMS block fits better with the SEC results. Furthermore, the obtained M_n value for PS-*b*-PDMS found with ^1H -NMR is around 10 kg/mol higher than the one found from SEC. However, again it is noted that SEC results are calculated without an instrument calibration and against PS standards, which is not ideal for BCPs. Lastly, the M_n for PDMS found from ^1H - ^{29}Si HMBC is almost the same as the one from ^1H - and ^{29}Si -NMR, verifying its potential for the characterization of silicon-containing compounds. With these results, it is argued that ^1H - ^{29}Si HMBC NMR experiments can be used for molecular weight characterization just like ^{29}Si .

*Table 3: Number molecular weight averages of a PS-*b*-PDMS sample calculated from different NMR spectra and SEC analysis for comparison*

| PDMS $M_n, ^{29}\text{Si-NMR}$ [g/mol] | PDMS $M_n, ^1\text{H-NMR}$ [g/mol] ^{a)} | PDMS $M_n, ^1\text{H-NMR}$ [g/mol] ^{b)} | PDMS $M_n, ^1\text{H-}^{29}\text{Si-NMR}$ [g/mol] | PDMS M_n, SEC [g/mol] ^{c)} | PS- <i>b</i> -PDMS $M_n, ^1\text{H-NMR}$ [g/mol] | PS- <i>b</i> -PDMS M_n, SEC [g/mol] |
|----------------------------------------------|--------------------------------------------------------|--------------------------------------------------------|---------------------------------------------------------|----------------------------------------------------|--------------------------------------------------------|----------------------------------------------------|
| 5096 | 3955 | 5226 | 5521 | 4068 | 41531 | 32300 |

a) Calculated from the DP found from end-group analysis with s-Butyl. b) Calculated from the volume fraction ($f_{\text{PDMS}} = 0.13$) and PS-*b*-PDMS M_n found with ^1H -NMR. c) Calculated from the volume fraction ($f_{\text{PDMS}} = 0.13$) found with ^1H -NMR and PS-*b*-PDMS M_n found with SEC

3.3.2 ^1H - ^{29}Si HMBC NMR analysis

A ^1H - ^{29}Si HMBC spectrum is presented in Figure 14. All signals are split into doublets, separated by approximately 7 Hz, coming from the $^2J_{\text{CH}_3\text{-Si}}$ coupling between the methyl protons and the silicon nuclei. The most intense signal is the one found at $(\delta^1\text{H}, \delta^{29}\text{Si}) = (0.18, -22.13)$ ppm from the coupling between protons of the methyl groups to the silicon found in the PDMS siloxane backbone, labelled D_m . Additionally, signals from its satellites are also observed and marked with * in the top ^1H -NMR. The signal from excess monomer D_3 is found at $(0.27, -8.45)$ ppm. Signal M corresponds to the TMS end-group, while J, label the signal confirming the presence of a covalent bond between PS and PDMS in PS-*b*-PDMS. In the same ^1H chemical shift range as signal J, a broad signal at $\delta^{29}\text{Si} = -21.6$ ppm is seen. This is believed to originate from J_i based on the signal location and the 1:1 ratio between the normalized integrated values of J and J_i . The small broad peak/shoulder seen most clearly in the ^1H -NMR trace is assigned to the D_j group. Its ^1H - ^{29}Si HMBC signal intensity largely overlaps with the D_m signal which limits its uses.

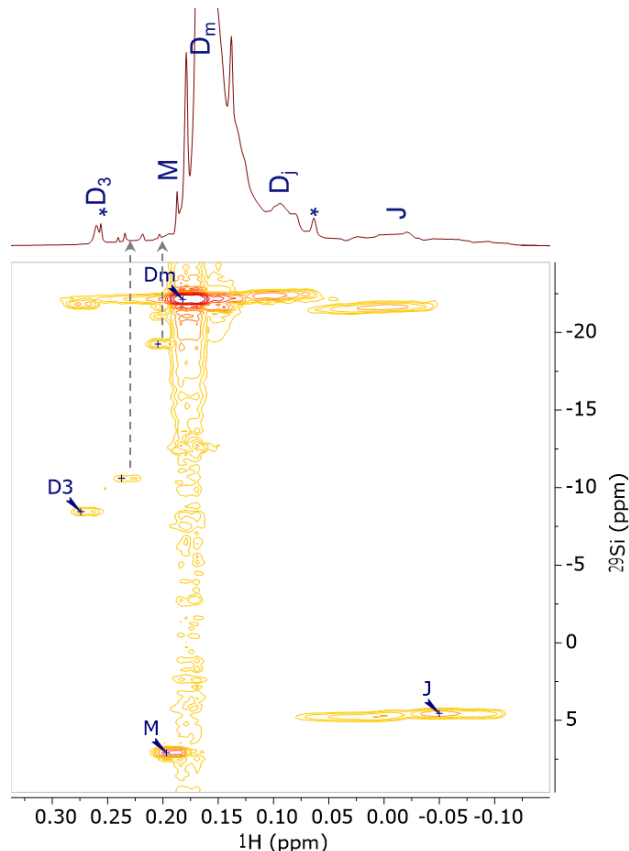


Figure 14: ^1H - ^{29}Si HMBC spectrum with ^1H chemical shift horizontally and ^{29}Si chemical shifts vertically. Signals from D_m with satellites marked *, D_j , M end-group, J block coupling and D_3 . At the top is the corresponding ^1H -NMR trace is found. The spectra was measured on a 600MHz NMR instrument.

Additionally, two minor signals corresponding to resonances in the ^1H -NMR spectrum are seen at (0.24, -10.60) ppm and (0.20, -19.25) ppm. The first signal probably arises from methyl groups in a M^{OH} which fits well with the presence of a minor signal around 4.75 ppm in ^1H -NMR. This indicates the presence of water and it was again observed for sample SD42, SD108 and SD64 which also could explain why the molecular weights found in Table 2 are almost twice the desired (M_n from initiator volume). The latter signal at (0.20, -19.25) ppm is believed to be from protons in a cyclic silicone oligomer, D_4 originating from backbiting reactions as has been reported before [117, 124]. This signal was only observed in samples with conversion rates $x_{\text{NMR}} \geq 90\%$.

M_n for the PDMS block was calculated from the integrated signal values and compared with ^1H -NMR and SEC results, as seen in Table 4. From these results, it is seen that the M_n values obtained from ^1H - ^{29}Si HMBC are way off the results from ^1H -NMR and SEC except for samples SD19 and SD38. Because of this, it is believed that the M_n obtained from ^1H - ^{29}Si HMBC NMR is very sensitive to the PDI of the BCP and cannot be used for BCPs with PDIs > 1.13 .

Table 4: Number molecular weight averages of the PDMS blocks calculated from different ^1H - and ^1H - ^{29}Si HMBC NMR spectra and SEC analysis for comparison.

| Sample | PDMS | PDMS | PDMS | PDMS |
|--------|----------------------------------------------------|----------------------------------------------------|---------------------------------------------------------|------------------------------------------|
| | M_n , ^1H -NMR [g/mol] ^{a)} | M_n , ^1H -NMR [g/mol] ^{b)} | M_n , ^1H - ^{29}Si -NMR [g/mol] | M_n , SEC-NMR [g/mol] ^{c)} |
| SD42 | 11231 | 11695 | 5403 | 16916 |
| SD108 | 21498 | 22507 | 4710 | 31322 |
| SD64 | 8451 | 8910 | 4273 | 12782 |
| SD19 | 6621 | 6575 | 6264 | 4922 |
| SD38 | 9581 | 10021 | 8209 | 10533 |

a) Calculated from the DP found from end-group analysis with s-Butyl. b) Calculated from the volume fractions and PS-*b*-PDMS M_n found with ^1H -NMR, Table 2. c) Calculated from the volume fraction found with ^1H -NMR and PS-*b*-PDMS M_n found with SEC in Table 2

3.3.3 Investigating kinetics with ^1H and ^1H - ^{29}Si HMBC NMR

The synthesis of sample SD19 was followed by taking small aliquots at different times during the reaction to investigate the reaction kinetics through ^1H -NMR and ^1H - ^{29}Si HMBC NMR. Each aliquot, except for the one taken from the PS solution which was terminated by MeOH, was terminated by triple excess of CTMS.

When comparing the ratio between the signal intensities of CTMS and D_3 from ^1H -NMR and ^1H - ^{29}Si HMBC, it is seen that they are almost identical. This again means that the assumption of a similar T_2 relaxation for the different nuclei is acceptable and that a difference in T_2 will have a very small influence on the volume integrals obtained from ^1H - ^{29}Si HMBC. However, for the measured sample aliquots a clear underestimation of the signal intensities from ^1H - ^{29}Si HMBC NMR compared to ^1H -NMR is observed, suggesting that ^1H - ^{29}Si HMBC, in this case, is not useful for quantitative analysis. This is among other things, believed to be caused by the relatively high amounts of CTMS and D_3 present in the samples, which makes the intensity integrations even more challenging. Because of this, the integrated values from the ^1H - ^{29}Si HMBC NMR spectra of the aliquots were only used qualitatively to compare the different aliquots.

This is seen in Figure 15, where the graph shows the ratio between PDMS and D_3 signal intensities found from ^1H and ^1H - ^{29}Si HMBC NMR plotted against the reaction time after PSLi^+ polymerization. Note that the x -axis is not linear. The black lines indicate the addition of a) D_3 monomer to the PSLi^+ polymerization, b) THF solvent and d) CTMS terminating agent to the reaction while c) indicate the cooling to -16°C . The conversion of D_3 to PDMS is also seen in the corresponding ^1H -NMR spectra to the right in Figure 15.

No polymerization of D_3 is observed before the promoter, THF, is added whereas after a rapid polymerization into PDMS is seen. The ^1H -NMR data shows that it takes less than 15 min to obtain around 70% conversion into PDMS which after 4 days at

-16°C increases to around 90%. A second thing to note is that the conversion percentage does not seem to change much from termination (d) to 15 min after termination suggesting that full termination happens in less than 15min and is rather stable for up to 2h after termination.

Figure 16 shows the ^1H - ^{29}Si HMBC NMR spectrum from the sample aliquot taken out right after THF addition. We observe the main signals from D_m (incl. satellites *), M and J which confirms the presence of PDMS covalently bonded to PS with end-

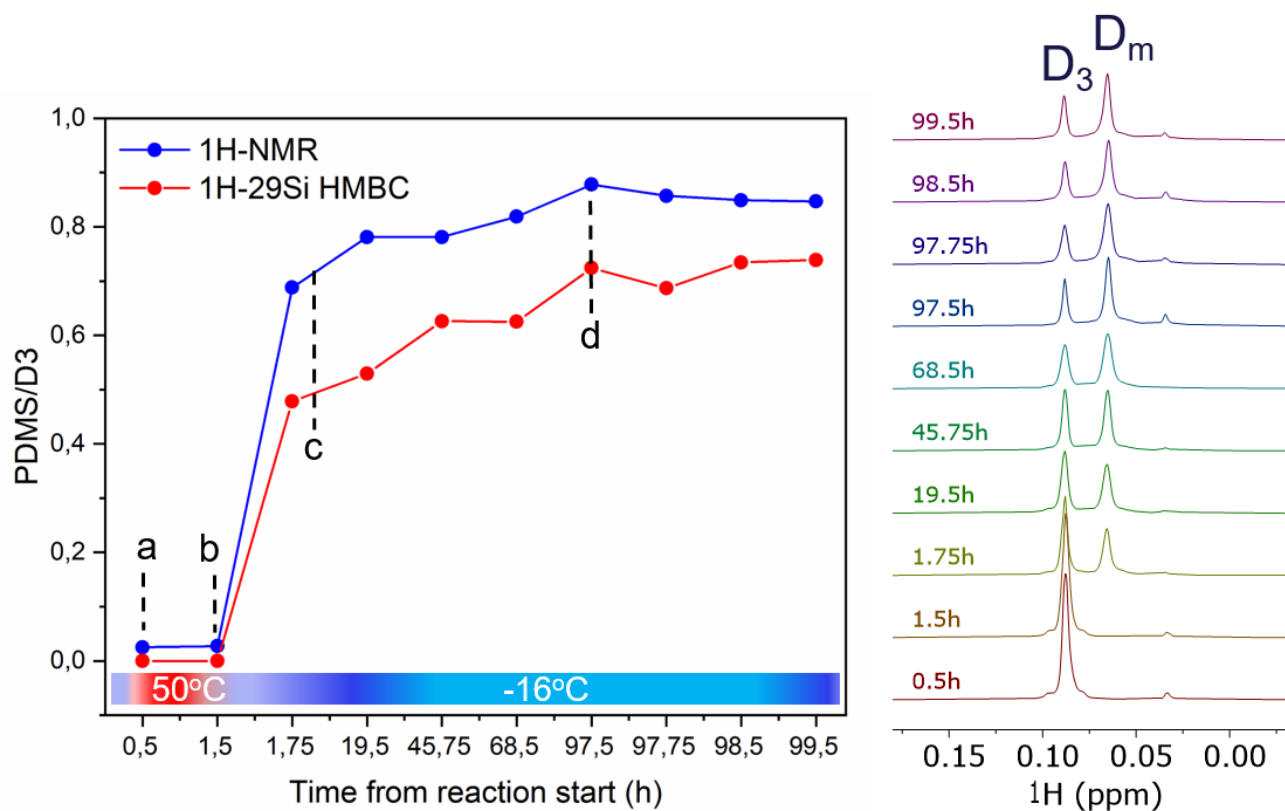


Figure 15: Graph showing the D_3 conversion found with both ^1H and ^1H - ^{29}Si HMBC NMR as function of reaction time after PSLi^+ polymerization. The corresponding ^1H -NMR spectra is found to the right, showing the signals from D_3 and D_m : PDMS. The black lines in the graph indicate a) when D_3 was added to PSLi^+ at 50°C, b) THF added at $T=25^\circ\text{C}$ and left for 2 h before c) the reaction was cooled down to -16°C and left until d) CTMS was added to terminate the polymerization.

group M. The signal in ^1H -NMR at $\delta^1\text{H} = 0.009$ ppm, seen in Figure 16, is a silicon-containing contaminant ($\delta^{29}\text{Si} = 10.9$ ppm) that is constant during the whole reaction and is believed to originate from the D_3 monomer.

Additionally, a signal from J_i is also seen together with the signal from the D_j groups. However, for the latter, it is tricky to see the splitting of the peak in the ^1H - ^{29}Si HMBC and it overlaps with the D_m signals so its integration is better done in the ^1H -NMR spectrum. Furthermore, a signal at $(\delta^1\text{H}, \delta^{29}\text{Si}) = (0.028, -21.89)$ ppm is seen which couples to a signal in the ^1H -NMR on the right of the M end-group signal. This signal is believed to originate from D_i groups in PDMS homopolymer and PS-*b*-PDMS since a comparison of its integral with the integration of signal J from the ^1H - ^{29}Si -HMBC NMR, results in a ratio beyond 1:1 (approximately 4.5:1). With this, the presence of PDMS homopolymer can be identified quickly without the need of SEC measurement. The same comparison were done with ^1H -NMR integrals but these were inconclusive due to peak overlap.

SEC measurements was performed on all aliquots and the results are shown in Figure 17

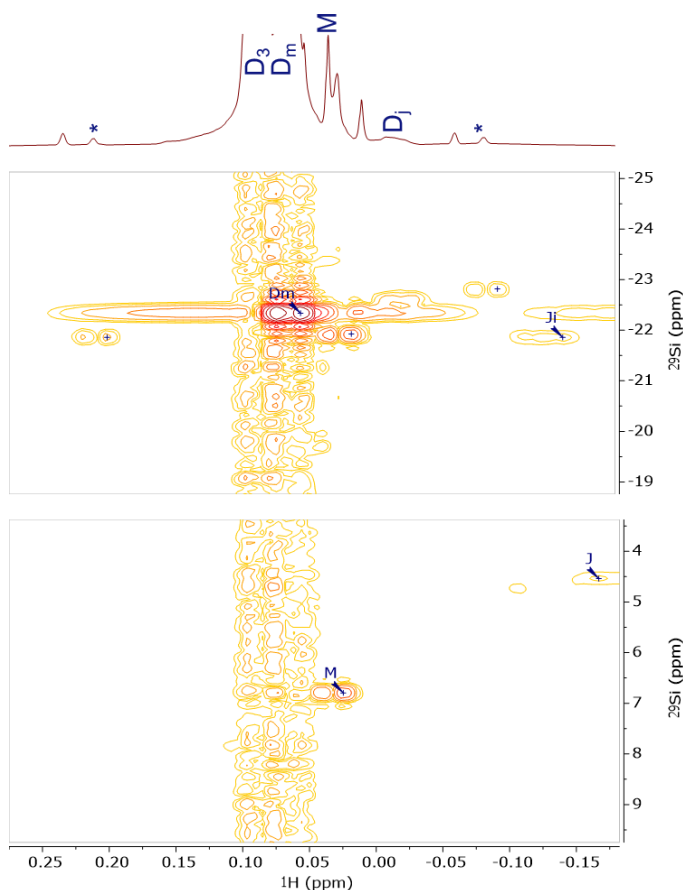


Figure 16: ^1H - ^{29}Si HMBC of the sample aliquot taken out right after THF was added. Signal from D_3 , D_m with satellites marked *, D_j , end-group M, and the PS-*b*-PDMS block coupling, J and J_i . At the top is the corresponding ^1H -NMR trace is found. This spectrum was measured on a 600MHz NMR instrument.

and in a table in appendix B4. As previously mentioned, a shoulder at high retention volumes was observed already in the PS aliquot and is still visible in the aliquots taken out before adding THF (0.5h and 1.5h). When THF is added (1.75h) and the polymerization of PDMS starts, the shoulder is swallowed by the PS-*b*-PDMS signal that moves to a slightly higher molecular weight, as also seen in the table in appendix B4. The RI signal stays more or less stable during the polymerization propagation at -16°C until the whole reaction is terminated after 97.5h. Here a negative RI signal from a low molecular weight PDMS homopolymer appears and does not seem to change in the following hours after termination. The molecular weight averages listed in appendix B4 are around the same values for all aliquots with a final M_n of 18700 g/mol which is very close to the value (15000 g/mol) anticipated from the initiator volume. The PDIs indicate a narrow PS-*b*-PDMS distribution that seems to decrease during the reaction, especially after termination (97.5h). However, this is probably due to the appearance of the PDMS homopolymer RI signal which overlaps with the PS-*b*-PDMS RI signal. Furthermore, the final PDI of 1.12 is again expected to be overestimated due to the lack of calibration parameters in the SEC analysis.

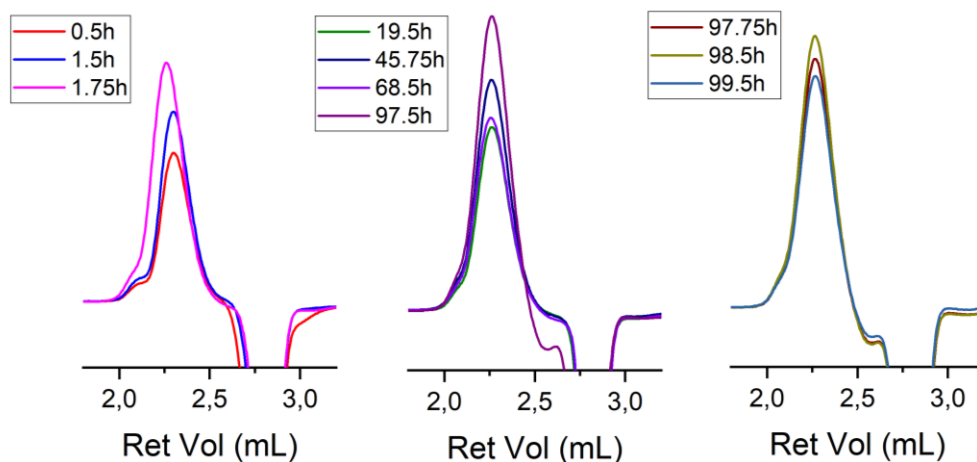
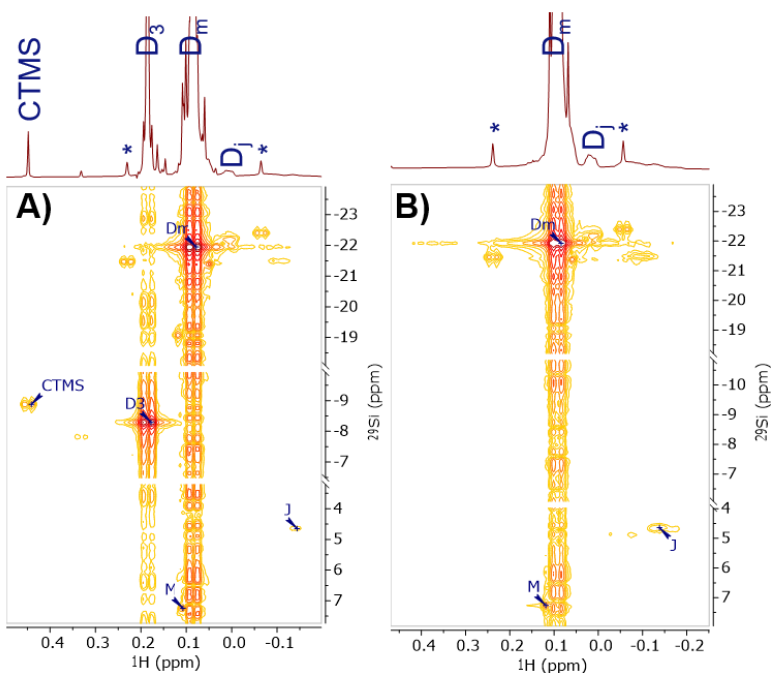


Figure 17: SEC RI data from SD19 aliquots.

3.3.1 Homopolymer removal

The presence of PS and PDMS homopolymers has previously been reported as byproducts from the synthesis of PS-*b*-PDMS and different fractionation procedures have been proposed [94, 96]. Here, since the main problem seemed to be the removal of PDMS homopolymer and the residue D₃, *n*-pentane, a slight PDMS favored solvent, was used to wash the samples. The washing resulted in a cloudy mixture with a white solid at the bottom, presumably PS-*b*-PDMS which was filtered from

the rest of the solution. In appendix B5 the SEC traces of SD108 from before and after the *n*-pentane washing is shown. From this, a clear removal of the negative RI increment around 2.2 mL is seen, indicating the removal of the PDMS homopolymer. Investigation with ¹H- and ¹H-²⁹Si HMBC NMR of both the solid and the liquid phase after washing confirmed the removal of the excess D₃ monomer and other impurities as shown in Figure 18. The PDMS mole fraction relative to the signal from the PS-*b*-PDMS junction, J in ¹H-²⁹Si HMBC does not change after washing in *n*-pentane which indicates that none of the BCP was lost. This is further confirmed from the ¹H-NMR



*Figure 18: ¹H-²⁹Si HMBC of SD19 before **A)** and after **B)** washing in *n*-pentane. With **B)** showing signals from CTMS, D₃, D_m with satellites marked *, D_j, M end-group, and the PS-*b*-PDMS block coupling, J and J_i. At the top is the corresponding ¹H-NMR traces found. These spectra were measured on a 400MHz NMR instrument.*

of the liquid phase where PS, PDMS and D₃ were present but from ¹H-²⁹Si HMBC no signal from the J block coupling at (δ^{1H} , δ^{29Si}) = (-0.11, 4.67) ppm was found which means the PS and PDMS signals originate from homopolymers, see appendix B6. Table 5 shows the molecular characteristics obtained after some of the samples were washed in n-pentane. The first thing to note is that the volume fractions now are way lower than the initial found values from Table 2 and actually in or close to the spherical morphology regime.

The obtained M_n values from the ¹H-NMR analysis fit nicely with the SEC analysis. This agrees well with the reduced solvent and impurity peak overlap observed from ¹H-NMR in the washed samples compared to the as-synthesized and highlights the importance of purification and complete drying. The PDIs are similar to the ones found prior to the washing and still indicate the presence of impurities during the synthesis.

*Table 5: Molecular characteristics of the synthesized PS-*b*-PDMS washed in pentane*

| Sample | $f_{\text{PDMS, NMR}}$ | $M_n, \text{1H-NMR}$ [g/mol] | M_n, SEC [g/mol] | M_w, SEC [g/mol] | PDI |
|--------|------------------------|---------------------------------|------------------------------|------------------------------|-------|
| SD42P | 0.14 | 46645 | 41600 | 52900 | 1.272 |
| SD108P | 0.17 | 111899 | 107900 | 170500 | 1.58 |
| SD19P | 0.19 | 22757 | 19200 | 22400 | 1.167 |

3.4 Summary

In this chapter, we have synthesized the silicon-containing BCP, PS-*b*-PDMS through sequential anionic polymerization of styrene and D₃. We obtained BCPs with number molecular weight averages (M_n) ranging from approximately 100 kg/mol down to 20 kg/mol and PDIs in the 1.6-1.08 range. We observed that the reaction time of the D₃ ring opening can be speeded up by applying heat for a couple of hours. Our results suggest that to ensure full D₃ ring opening reaction times longer than 1.5 h at 50°C is required. We have further shown what a powerful technique ¹H-NMR is for

molecular characterization and end-group analysis of BCPs, especially BCPs with $\text{PDI} < 1.13$. Additionally, we have shown the first demonstration of how ^1H - ^{29}Si HMBC NMR can be used as a complementary technique to ^1H -NMR and that it is a fast characterization method to e.g. reveal the direct coupling between two blocks in a silicon-containing BCP, such as PS-*b*-PDMS. From this, we also argue that ^1H - ^{29}Si HMBC NMR seem to be a valid way to obtain M_n values of the PDMS block when looking at samples with narrow PDIs (< 1.13). Lastly, we showed how homopolymers of PS and PDMS can be removed by washing the products with *n*-pentane. With these results, we have demonstrated the potential of NMR for molecular weight determination and characterization of polymers, such as block copolymer systems containing silicon. We hope that these findings will encourage polymer researchers to explore the many possibilities of NMR for polymer characterization.

.

4 Self-assembly of PS-*b*-PDMS on 2D materials

In the following chapter, the self-assembly of a PS-*b*-PDMS thin film on hBN together with the nanopatterning of hBN and a vdW heterostructure of hBN encapsulated graphene is presented. The main part of this chapter is based on the manuscript “*Nanopatterning of hBN via Block Copolymer Self-Assembly of PS-*b*-PDMS*”, Christina. Breth Nielsen, Anton Lyksborg-Andersen, Xiang Cheng, Tim Booth and Kristoffer Almdal, which is to be submitted (can be found in appendix E).

4.1 Introduction

For many of today’s technologies, such as data storage [30, 132], integrated circuits [20, 25, 55, 67, 100] and membranes [11-13], lithographic structuring is an essential step in device fabrication process. As devices have become smaller, specialized nanopatterning methods, such as electron beam-, ion beam- and deep UV lithography have risen. Most of these methods are limited by cost and lack of efficient upscaling [24, 27, 133]. However, block copolymer (BCP) nanopatterning has shown very promising results in terms of low cost, scalability, and efficiency in obtaining feature sizes from 100 nm to below 10 nm [55, 90, 134].

BCP nanopatterning typically uses thin films of BCP solutions to open a range of patterning morphologies driven by the thermodynamics of the BCP self-assembly mechanism. The key factors regarding BCP self-assembly in thin films are the block characteristics, substrate chemistry, interface interaction, and film thickness [13]. The interaction between the blocks is described by the Flory-Huggins interaction parameter (χ) which together with the degree of polymerization (N) governs the pattern feature size. Recent BCP nanopatterning studies have been focused on e.g. polystyrene-*block*-polydimethylsiloxane (PS-*b*-PDMS) which not only has a high χ -parameter but also shows good etch contrast between its constituent blocks [4, 6, 20, 47, 49, 90, 100].

Patterning lattices of antidots (holes) in 2D materials has been shown to be a viable route towards controllably introducing a tailored bandgap [9, 135]. BCP nanopatterning has previously been applied to perform such structuring on graphene and MoS₂ [15, 20, 25, 30, 55, 90, 100, 103]. However, despite the huge potential of BCP nanopatterning for the structuring of 2D materials, it has not expanded to other 2D compounds.

A common problem when doing BCP nanopatterning on 2D materials is the existence of polymer residues on the 2D material after the nanopatterning process. The presence of these has been shown to impact the electronic properties e.g. by introducing p-doping of graphene resulting in decreased device performance [15, 90, 103, 136]. These residues often come from the use of polymer brushes or random BCPs used on graphene or MoS₂, to functionalize their surfaces before the BCP nanopatterning process [15, 20, 30]. The brush layers help to obtain long-range order and to control the morphology orientation. However, it also adds additional steps to the BCP process which is not desirable when considering manufacturing [15, 100].

Besides the ordering, the brushes also decrease the possibility of dewetting and hence wetting layers at the top/bottom interfaces, which are often seen for BCPs with large surface energy differences such as PS-*b*-PDMS. The formation of wetting layers in the PS-*b*-PDMS system has been investigated towards different surfaces, including chemical vapor deposition (CVD) graphene, usually based on its water contact angle. The studies report the formation of wetting layers at the substrate/BCP and BCP/air interfaces [6, 41, 100]. We note that studies on the wetting of PS-*b*-PDMS towards mechanically exfoliated graphene are limited, although this remains the best way to obtain high-quality graphene [15, 136].

Problems regarding the conservation of the intrinsic properties arise when nanostructuring 2D materials, due to bad pattern quality, in the form of dangling bonds, edge- and line roughness, polymer residues, etc. [21, 137]. Previous studies have shown that encapsulation of 2D materials can limit these problems and thereby

maintain the wanted properties of pristine graphene. A good example is the van der Waals (vdW) heterostructure of hBN-encapsulated graphene [15, 20, 67, 102, 138]. hBN is an insulator that is structurally isomorphic to graphene and is a good candidate material for future separation technologies [139, 140]. It has been shown that graphene, sandwiched between two hBN flakes, can be nanopatterned with e-beam lithography and afterwards show the opening of a tunable band gap and persistent physical properties compared to pristine graphene [9]. However, to mimic this with a BCP nanopatterning process, we first need to know how the use of hBN affects the BCP nanopatterning process. This will include the effects arising from the difference in surface energy and the use of exfoliated flakes. To the best of our knowledge, BCP nanopatterning has never been studied on heterostructures or hBN.

In this chapter, we aim to investigate the BCP nanopatterning process on mechanically exfoliated hBN flakes using cylindrical forming PS-*b*-PDMS. Through cross-sectional scanning transmission electron microscopy (STEM) and atomic force microscopy (AFM), we study the cylindrical morphology and orientation together with the interactions at the different interfaces obtained through solvent vapor annealing (SVA). We demonstrate a 15 W oxygen plasma method to remove the PS block and simultaneously oxidize the PDMS into hard silicon oxycarbide cylinders (ox-PDMS) [20]. Finally, the pattern transfer into mechanically exfoliated hBN flakes is verified.

4.2 Experimental

4.2.1 Materials and sample fabrication

PS-*b*-PDMS (M_n : 37,9 kg/mol, PDI: 1.1 (SEC results measured against PS standards), f_{PDMS} : 0.28 (from H-NMR), $L_{0,\text{calc}}$: 24 nm from self-consistent mean-field (SCMF) theory, assuming $\chi = 0.265$ [88] and other values from [141]) was synthesized by living anionic polymerization. Polymerization of styrene in cyclohexane was initiated with sec-butyllithium and hexamethylcyclotrisiloxane was added after 18h. The reaction was left overnight at RT. The next morning THF was added and the reaction

was left to stir for 2h at RT before getting cooled to 0°C and left there for 3 days. Hereafter, the reaction was terminated with chlorotrimethylsilane. All solvents were purchased from research chemical suppliers and monomer and solvent purification was done as described elsewhere [129].

Si/SiO₂ (90nm) substrates were marked with an index mark system using optical lithography and deposition of Cr/Au in a conventional lift-off process. Crystals of hBN and graphene were purchased from HQ Graphene and exfoliated onto these Si/SiO₂ substrates with semiconductor die sawing tape (Nitto Denko) after pre-treatment of the wafers with an O₂ plasma (PlasmaEtch PE-50, 120W, -200 Torr, 5 sccm, 8-10 min) to improve adhesion. hBN/graphene/hBN stacks were made with CAB transfer [78]. The PS-*b*-PDMS was dissolved in cyclohexane with a 1 wt. % concentration and spin-coated at 3000 rpm, acceleration 500 rpm/s for 60s with a static dispense method onto the Si/SiO₂/hBN, leaving a thin film of approx. 35 nm. The film was solvent vapor annealed on a petri dish within a petri dish (approx. S/V = 0.68 [47]) with toluene (2.5 mL) and a lid on top for 20 min at RT.

Hereafter, the sample was subjected to an O₂ plasma etch (Moorfield Minilab 026, 15W, running pressure: 1.8x10⁻² mbar, 10 sccm, DC bias: 160 V, -20 min), removing the PS block and leaving the robust oxidized PDMS template on top of hBN. An annealing step at 500°C for 3h in 3% H₂/Ar was introduced to remove residual PS. An SF₆ plasma etch (Moorfield Minilab 026, 10W, running pressure: 1.8x10⁻² mbar, 10 sccm, DC bias: 128 V, 30-60s) removed the exposed parts of the hBN flakes and the ox-PDMS, leaving only the patterned hBN flakes.

4.2.2 Atomic force microscopy

Atomic force microscopy (AFM) is used to obtain surface topography at the atomic scale in three dimensions. It can be operated in different modes, however, for BCP film studies, AFM in tapping mode is desired since it is non-destructive and also provide phase contrast imaging that can give additional information about the

sample [142]. The AFM measurements were conducted on a Bruker Dimension Icon-PT instrument, in either soft-tapping air mode (height and phase) or with ScanAsyst mode (height). A standard tapping mode tip was used, and the typical acquisition parameters were 256 lines with a scan rate of 0.99 Hz. Scan sizes were typically between 500 nm and 4 μm .

4.2.3 Electron microscopy and focus ion beam processing

Electron microscopy techniques are powerful and often crucial when working on the nanoscale. They can produce high-resolution images on the atomic scale using highly focused electron beams. For this project, cross-sectional, micron-sized sample lift outs have been essential for the understanding of the sample. These cross-sectional lift outs were prepared using a Focus Ion Beam (FIB) processing method performed in a scanning electron microscope (SEM). The sample edges were painted with silver paint to reduce charges from building up and mounted on an SEM holder. The SEM/FIB processing was done on an FEI-Helios dual beam system with 5 kV and the sample preparation was done as described elsewhere [143]. All samples were coated with an electron beam deposited gas, Trimethyl(methylcyclopentadienyl)platinum(IV) (MeCpPtMe_3) before FIB milling. The nanopatterned hBN sample was coated with evaporated carbon and 1-2 nm gold before the e-beam coating to protect the surface from the harsh MeCpPtMe_3 e-beam deposition. The cross-sectional lift-outs were thinned with the FIB before during STEM measurement. Bright-field and high-angle annular dark-field (HAADF) STEM imaging and STEM-EELS measurements were conducted on a Titan Analytical 80-300ST TEM operated at 300 kV or 120 kV.

4.1 Results and discussion

The fabrication process is illustrated in Figure 19. No surface treatment was used before the spin casting of the PS-*b*-PDMS (27K/11K) BCP thin film onto a wafer with exfoliated flakes of 2D materials. The resulting film thickness, t_{film} , as determined by atomic force microscopy (AFM), was 30-40 nm, close to an integer multiple of the natural period (L_0). However, the presence of exfoliated 2D material flakes with different heights ranging from monolayers (4.1Å) to multilayers of hundreds of nm, produced inhomogeneities in the film thickness in different areas on the substrate.

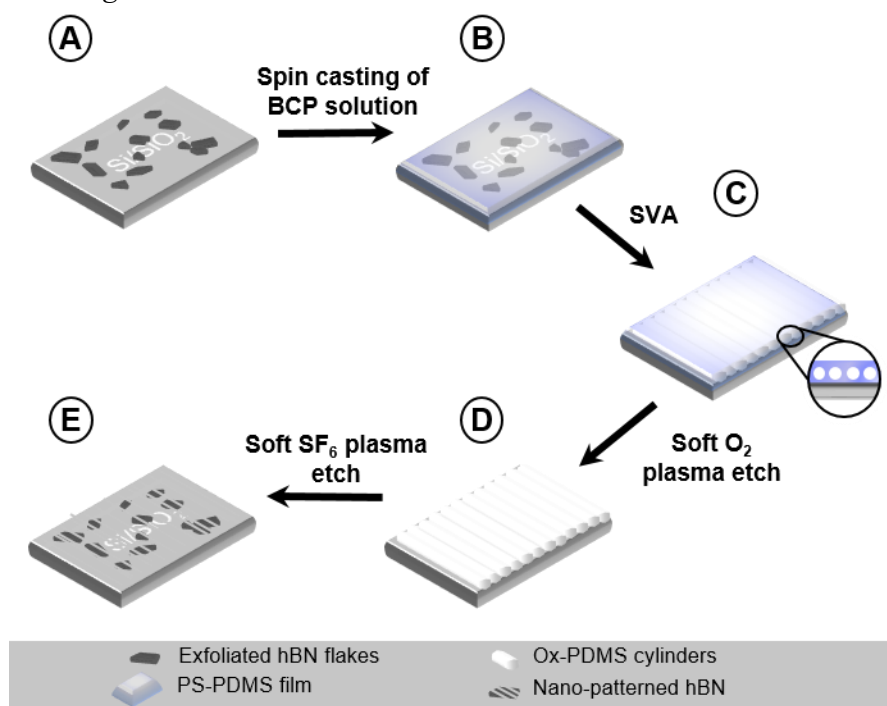


*Figure 19: Illustration of the BCP nanopatterning process. **A)** hBN flakes were exfoliated onto an argon plasma etched Si/SiO₂(90nm) substrate. **B)** A PS-*b*-PDMS (38K) solution was spin-cast with a static method onto the Si/SiO₂/hBN, leaving a thin film of approx. 30-40 nm. **C)** SVA in toluene for 20 min at RT. **D)** A O₂ plasma etch, removes the PS block and leaves a robust ox-PDMS hard template on top of hBN. **E)** A furnace annealing and a SF₆ plasma etch, removes the exposed parts of the hBN flakes and the ox-PDMS, leaving nanopatterned hBN flakes. Order depended heavily on the film thickness and it was expected to influence the ordering of the ox-PDMS cylinders over a large area.*

As reported for other cylindrical forming BCP systems, the equilibrium order depended heavily on the film thickness [37] and it was expected to influence the ordering of the oxidized PDMS cylinders over a large area.

The samples were annealed for 20 min in toluene vapor at RT [9, 81]. The ratio, S/V (S = surface area of the solvent, V = volume of air mixing with the solvent vapor) was kept at around 0.65 cm^{-1} . After SVA, terraces with thicknesses approximately 10 nm taller/deeper than the original thickness were formed on all samples. These were observed by both SEM- and AFM images, seen in Figure 20 and appendix C1 respectively.

4.1.1 PS-*b*-PDMS self-assembly on hBN

To investigate this further, SEM/FIB cross-sectional lift-outs were made which also allowed the investigation of the PS-*b*-PDMS wetting on hBN. Two lift-out regions were chosen from optical microscope images, one showing a varying film thickness on an hBN flake and one showing a smooth film on an hBN flake, see Figure 20A and appendix C2. Figure 20A shows an SEM image from the varying film thickness region. The dark terraces were, through AFM and the cross-sectional STEM images, found to contain ordered PDMS cylinders in a PS while the brighter parts showed a different morphology.

Figure 20B is a zoom-in from an area with a film thickness of 29 nm. Here the desired morphology with PDMS cylinders in a PS matrix is found with a periodicity, $L_0 \sim 35 \text{ nm}$ and a PDMS cylinder diameter of 15 nm. In previous cross-sectional studies of PS-*b*-PDMS films under SVA they observed an elliptic distortion of the PDMS cylinders which is discussed to originate from in-plane film strain formed by the solvent evaporation [4, 6]. This distortion is, however, not observed in this study. Going towards an area with a lower film thickness, the morphology changes. Figure 20C shows a zoom-in of an area with a PS-*b*-PDMS monolayer film thickness of 21.5 nm. Here, a lamellar morphology parallel to the hBN surface is observed. This pattern

could also be from a PDMS cylinder cut in half, with a diameter of 10 nm.

However, this would mean that the equilibrium morphology would accept film thicknesses ranging from around 35 to 21.5 nm which seems unreasonable when considering the systems morphology sensitivity towards thickness changes [6]. The presence of silicon in the dark grey areas of the PS-*b*-PDMS film was confirmed by energy electron loss spectroscopy (EELS), see appendix C3. STEM images from the smooth film region are found in appendix C2. Here a non-ordered multilayer PS-*b*-PDMS film on hBN was found.

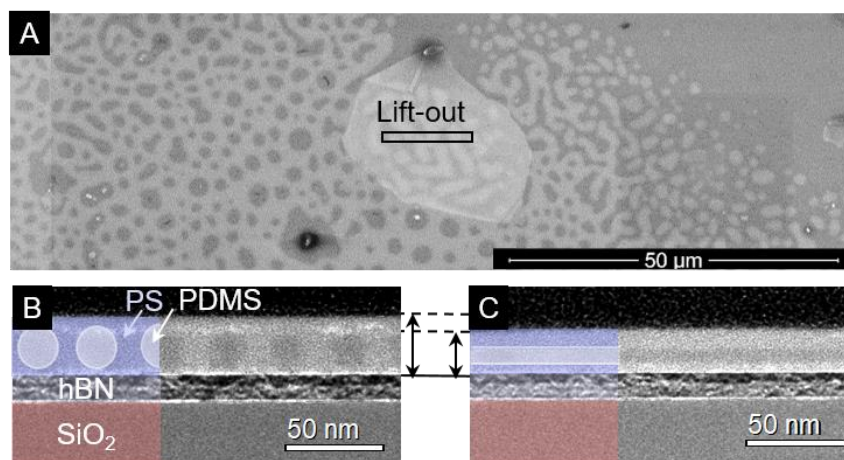


Figure 20: **A)** SEM image from before taken lift-out of hBN flake with a SVA PS-*b*-PDMS on top. The dark areas correspond to areas with horizontal PDMS cylinders in a PS matrix as seen in the cross-sectional STEM images of a sample lift-out with Pt/C protection on top of PS-*b*-PDMS on a hBN flake (12 nm thick)/SiO₂ (90 nm)/Si. **B)** zoom on an area with PDMS cylinders parallel to the hBN surface in a PS matrix and a film thickness of 29 nm. **C)** zoom on an area with PS-*b*-PDMS lamellae ordering parallel to the hBN surface and a PS-*b*-PDMS film thickness of 21.5 nm. The thickness difference between the two areas is illustrated with the arrows. The raw STEM images can be found in appendix C5.

In all cases, selective wetting towards PS at the hBN/BCP interface is observed. Additionally, no top- or bottom PDMS wetting layer(s) at either the BCP/air interface or the hBN/BCP interface is observed. This is a surprise, especially the fact that no PDMS wetting layer is observed at the BCP/air interface. The PDMS wetting layers are created because of the large difference in surface tension between PS (40.7 mN/m) and PDMS (19.9 mN/m) which leads to PDMS segregation at the interfaces [40]. Our findings are in contrast to previous observations with PS-*b*-PDMS on CVD graphene surfaces that have not been functionalized either thermally or by applying a polymer brush [58, 100]. The water contact angle for CVD graphene has been experimentally found to be around 68° but can be increased to 94.8° with a thermal treatment which results in the absence of a PDMS wetting layer at the graphene/BCP interface [100]. Similar increases in contact angles from 60° to 80° have been reported for exfoliated graphene when exposed to air over 4 days, whereas, for exfoliated hBN, a smaller increase is observed from approximately 82° to 88° [144]. Compared to CVD graphene, hBN has a slightly lower surface energy, which could explain the lack of a PDMS wetting layer at the hBN/BCP interface. The reason for the lack of a similar interface at the BCP/air interface is not clear.

The presence of PDMS wetting layers depends not only on the preferential interaction between the BCP and the substrate [6] but also on the film thickness [145] and the annealing procedure [90]. The lack of a PDMS wetting layer at the CVD graphene/BCP interface has been observed in one study using a combination of toluene solvent vapor- and thermal annealing (>45°C) [90]. They argue that the lack of the PDMS wetting layer is due to the toluene vapor pressure being high enough and slightly selective towards PS, to compensate for the PDMS segregation. However, these findings suggest that this compensation might already be realized by SVA in toluene at RT.

A lack of a PDMS wetting layer at the BCP/air interface is useful in this work since this means that plasma etching used to form the hard template can be performed in a single step with O₂ plasma. We used plasma powers of 10-15 W which are ideal for

2D material processes, but are an order of magnitude smaller than typical plasma powers for BCP templating [103, 134]. The O_2 process parameters were 10 sccm, 15 W, 20 min.

Figure 21A shows an AFM height image of an hBN flake edge with ox- PDMS on top after O_2 plasma etching. The presence of vertical and horizontal cylinders is seen on hBN whereas only horizontal cylinders are observed on SiO_2 . The top part of the hBN flake, which contains the largest number of vertical cylinders is thinner than the rest of the hBN flake, suggesting that the difference in BCP morphology is due to film thickness variations caused by the difference in flake thickness. Though, in general, a larger number of vertical cylinders was found on hBN flakes compared to SiO_2 which either means that hBN is somewhat non-selective towards the two blocks

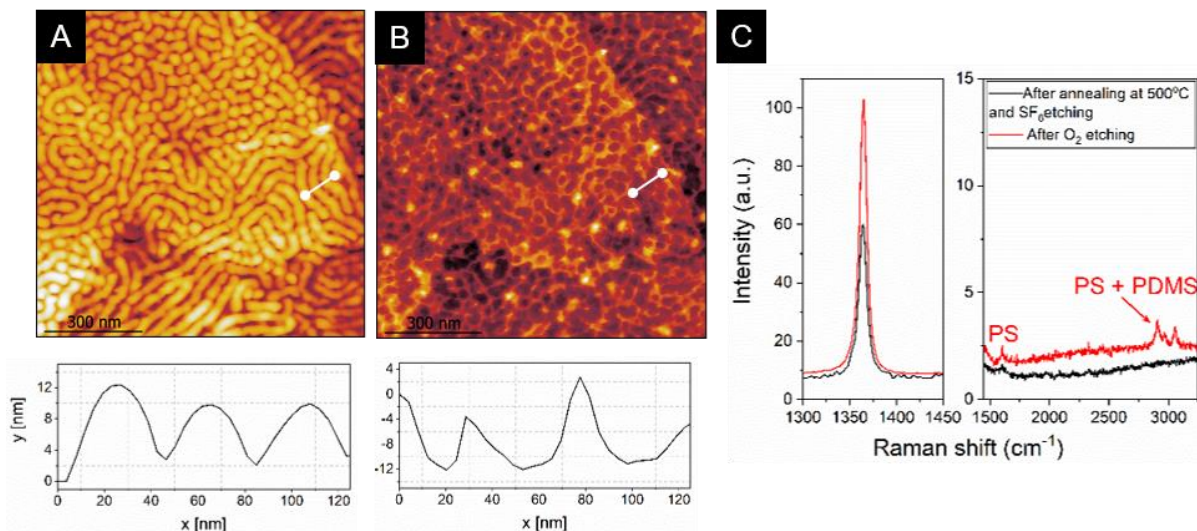
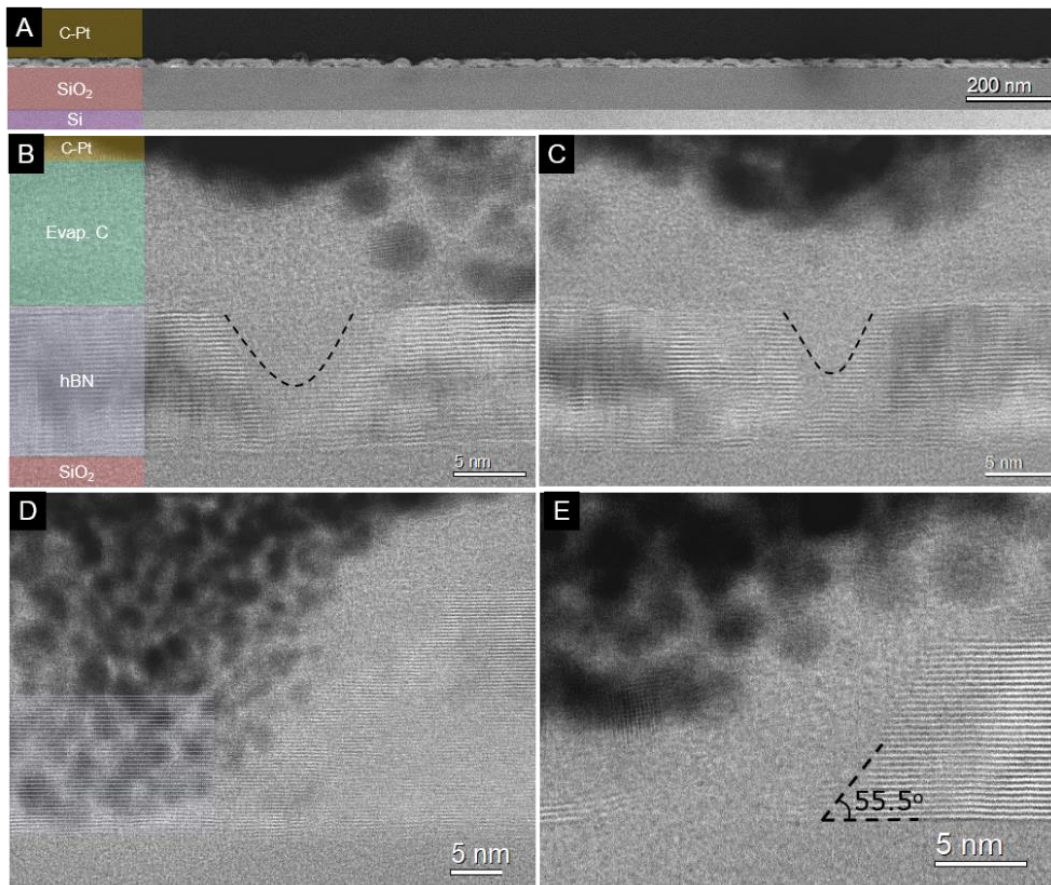


Figure 21: AFM height images at the edge of an hBN flake during the BCP lithography process. Height profiles from the white lines are shown beneath. A) After O_2 plasma etching, the height profile shows the contour of the ox-PDMS cylinders on top of an hBN flake. B) After furnace annealing and an SF_6 plasma etch, the height profile shows the inverted pattern into the hBN flake. C) Raman spectra of A) where PS is still present together with ox-PDMS after O_2 etching (red line) and B) after furnace annealing SF_6 plasma etching showing no presence of PS and PDMS seen (black line).

creating a perpendicular orientation or that a larger film thickness variation is seen on hBN compared to SiO₂. However, this was not investigated further. The height profile reveals 6-12 nm high cylinders and an $L_0 = 38.9$ nm, which is in accordance with the STEM cross-section results. Raman spectroscopic measurements after O₂ etching showed the presence of PS residues (Figure 21C). These residues have been shown to affect the electronic properties of 2D materials [15, 136]. To remove these residues, furnace annealing at 500°C under Ar/H₂ flow was performed. Finally, an SF₆ etching step (10 sccm, 10 W, for approximately 30 s) transferred the pattern into the hBN flakes, with the ox-PDMS acting as a template. Figure 21B shows an AFM height image of the same hBN flake edge after furnace annealing and SF₆ plasma etching. The height profile shows up to 15 nm deep holes. Additionally, from Raman spectroscopy measurements, the complete removal of both PS and PDMS after annealing and SF₆ etching is confirmed as presented in Figure 21C.

In Figure 22A a 1.5 μm overview image of the nanopatterned hBN flake, is shown. The platinum-containing protection layer reveals the non-ordered patterns, which is in good agreement with the aforementioned AFM and STEM images. The STEM images show the projection of the front of the cross-section which can be changed by changing the focus of the electron microscope and with this, it is possible to verify the origin of the patterns. Figure 22B shows a hole that continues when changing the focus, see Figure 22C. This indicates that an ox-PDMS mask with horizontal lying cylinders has been present prior to the SF₆ etching. Another thing to note is that there are no significant changes in the evaporated carbon layer which is a strong indication that all PS- PDMS residues have been removed, leaving a clean nanopatterned hBN surface.

Figure 22D and Figure 22E show STEM cross-sectional images from the same area of the lift out but with a different focus. These show a nanopatterned hole originating from a horizontal template pattern. The same is seen in Figure 22E together with an hBN etch angle of 55.5°. presence of hBN layers marked in Figure 22D is an indication that the pattern does not continue throughout the 100 nm cross-section



*Figure 22: Cross-sectional (S)TEM images of a sample lift out after annealing and SF_6 etching. **A)** and **B)** are images of the same area taken with different microscope focuses revealing a patterned hole that continues throughout the 100 nm cross-section. **C)** Shows an overview of the nanopatterned hBN flake. The amorphous carbon-Pt (C-Pt) protection layer helps to identify where the flake has been patterned. **D)** and **E)** are images of the same area taken with different microscope focuses showing a pattern that does not continue throughout the 100 nm cross-section. The blue lines in **D)** mark the hBN layers seen through the protection layer. Layers, Yellow: MeCpPtMe_3 , Green: Evap. C. = evaporated carbon, Blue: hBN, Red/Purple: SiO_2/Si . Raw STEM images can be found in appendix C6.*

and that it originates from an ox-PDMS template with vertical standing cylinders. Additional cross-sectional images can be found in appendix C4. Furthermore, in this study, angles of etched hBN sidewalls from 49-56° were observed; approximately 10° lower than the range of sidewall angles found in the literature [146, 147]. Our results suggest that a low-power plasma, results in a smaller sidewall angle than in the case of higher powers for similar chamber pressures. This lower sidewall angle is an advantage when considering using this process to nanopattern graphene in hBN/graphene/hBN stacks since it can provide an additional reduction in the feature size [147].

4.1.1 PS-*b*-PDMS self-assembly on hBN/Graphene/hBN

Initial tests on hBN/graphene/hBN stacks were done with the same process and resulted in pattern transfer. Figure 23A shows a STEM cross-sectional image of a stack with trilayer graphene encapsulated between a top layer hBN (16 nm) and a bottom layer hBN (85 nm). An indication of etch damage to the top layer hBN is seen

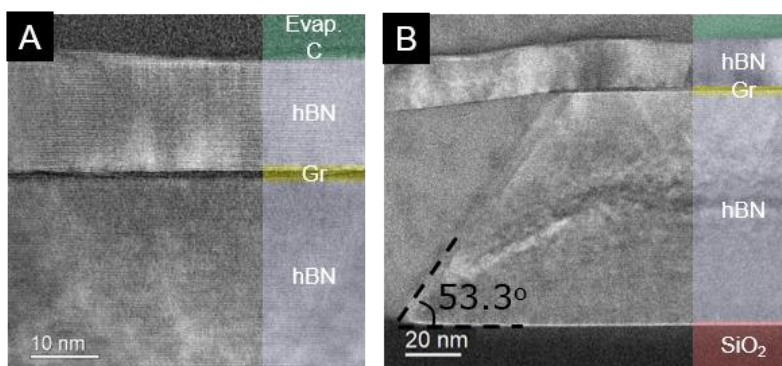


*Figure 23: Cross-sectional STEM images of a sample lift out after annealing and SF₆ etching of an hBN/graphene/hBN stack. **A)** Shows the atomic layers from hBN and graphene (Gr) in the stack. There is an indication of etch damage in the top hBN flake (16 nm). **B)** Shows that the top hBN flake has been shifted during the process due to bursting of trapped bubbles in the stack.*

and further analysis determined that the etch processes had been too long resulting in the complete removal of the stack in some areas. Figure 23B shows a STEM cross-sectional image where the top hBN layer has shifted several nanometers during the process. The bursting of the bubbles, trapped between the layers when producing the stack, causes this shift. In appendix, C7 optical images of the stacking process are found and here the presence of bubbles is seen. From these initial results, it is concluded that similar angles of etched hBN sidewalls around $53\text{-}56^\circ$ are found. Additionally, polymer residues were found beneath the bottom hBN layer which can be seen in appendix C8. These originate from the sample preparation and can be avoided.

4.2 Summary

In this chapter, we have demonstrated a BCP nanopatterning process that can be used to nanopattern mechanically exfoliated hBN flakes without requiring special pre-treatment, e.g. a polymer brush layer. Through cross-sectional lift-outs, the interactions between PS-*b*-PDMS and hBN were shown to allow the self-assembly of a monolayer of PDMS cylinders in a PS matrix parallel to the hBN flake. Notably, this occurs without the formation of PDMS wetting layers either at the substrate or air interfaces. After a single step of O_2 plasma etching, AFM images revealed the presence of both vertical and horizontal hard silicon oxycarbide cylinders lying on top of hBN. These patterns could be transferred into hBN flakes through an SF_6 etch step followed by furnace annealing, leaving a clean hBN surface that is ideal for device applications. Initial tests were performed on hBN/graphene/hBN stacks; however, some challenges were discovered e.g. concerning trapped bubbles in the stack resulting in a shift of the top hBN layer. With this study, we hope to pave the way for the application of BCP nanopatterning to structure mechanically exfoliated 2D materials and heterostructures other than graphene. This enables the patterning of a wider range of materials not only beyond the resolution limit of conventional nanolithography but also in a scalable manner.

5 PDMS nanofluidic channel fabrication on 2D materials

This chapter covers the latest part of the project, which was initiated at the National Graphene Institute (NGI), University of Manchester (UoM) in collaboration with colleagues from UoM and is still ongoing. The chapter is based on an idea for a nanofluidic device, fabricated through DSA of PS-*b*-PDMS combined with 2D materials. The chapter only covers the fabrication steps while initial fluidic test measurements are still to be performed. The specialized lithography pre-patterning and electron microscopy analysis was done in collaboration with trained colleagues from DTU and UoM.

5.1 Introduction

The field of fluidics studies the motion of fluids (gases or liquids) and their ability to control functions such as sensing, amplification and switching through the fluid stream much like electricity [148]. Fluidic device research gained momentum in the field of microfluidics, and with the emergence of nanotechnology, nanofluidics came into existence. Nanofluidics studies the flow of a fluid in and around objects where at least one dimension is limited to being below 100 nm. When operating at this scale, the objects show a high surface-to-volume ratio and different forces e.g. vdWs-, and electrostatic forces, start to play a key role and give rise to new physical phenomena [149].

Due to their ability to offer infinite possibilities in construction, atomic thinness, and precise control of interlayer distances down to the nano- and angstrom scale, 2D materials hold significant promise as materials for the development of nanofluidics. With graphene being impermeable to any liquids and gases, nanopores and nanochannels have allowed great prospects for graphene-based nanofluidic technologies such as gas separation membranes [12, 150] and water transport [19, 151, 152]. For instance, Å-sized capillaries made from graphene and its multilayers

have demonstrated an unexpectedly fast water flow rate [152]. Additionally, other 2D materials such as hBN and MoS₂ also showed promising gas flows [153] and water transport applications [17, 76].

The fabrication of 2D material-based nanofluidic devices usually requires high-cost lithography technologies. An alternative to this is to use block copolymer (BCP) self-assembly. BCP self-assembly has gathered massive interest due to its high potential as a template material for large-scale nanopatterning in the semiconductor industry [13, 27]. However, BCP self-assembly goes beyond the semiconductor industry and its ability to create nanopores and nanochannels can be utilized to create nanofluidic devices [23, 82, 83].

The BCP, polystyrene-*block*-polydimethylsiloxane (PS-*b*-PDMS) has been widely studied as a template material for the nanopatterning of various materials [39, 56, 90, 91] but it has never been studied as a fabrication route for PDMS nanochannels for nanofluidic devices. In PS-*b*-PDMS, the flexible block, PDMS is one of the most popular materials used in microfluidics due to its low cost, biocompatibility, elastomeric properties and optical transparency. Nevertheless, the intrinsic surface properties limit its use to applications requiring hydrophobic surfaces [154, 155].

It is known that the surface properties of PDMS can be modified from hydrophobic to hydrophilic through different processes, thermal treatment, use of coatings and plasma oxidation. An oxygen plasma treatment using a constant power of around 70 W for several minutes has been shown to produce hydrophilic, SiOH groups that do not recover back to their hydrophobic properties even after hours of air exposure [154].

Through the BCP nanopatterning process of cylindrical forming PS-*b*-PDMS, an oxygen plasma etching step is required to remove the PS block and simultaneously oxidize the PDMS cylinders into hydrophilic silicon oxycarbide (ox-PDMS) cylinder channels [39, 56].

In this chapter, we suggest a way to combine 2D materials with directed self-assembly (DSA) of PS-*b*-PDMS to produce a nanofluidic device with aligned ox-PDMS channels sandwiched between a top and bottom 2D material. The sagging and conformation of 2D materials to topographic substrates are believed to allow the introduction of nanofluidic channels in such a device [156]. We introduce soft graphoepitaxy using disposable positive-tone photoresist confinements to perform the DSA of PS-*b*-PDMS.

5.2 Experimental

The characterization techniques used in this chapter are the same as the ones referred to in the experimental section of chapter 4 (section 4.2). For this reason, these will not be elaborated further in the following section.

5.2.1 Materials and sample fabrication

PS-*b*-PDMS (M_n : 37,9 kg/mol, PDI: 1.1 (SEC results measured against PS standards), f_{PDMS} : 0.28 (from $^1\text{H-NMR}$), was synthesized by living anionic polymerization. The polymerization of styrene was initiated with sec-butyllithium in cyclohexane. After 18h hexamethylcyclotrisiloxane (D_3) was added and the reaction was left overnight at RT. THF was then added to promote the polymerization of D_3 and the reaction was left to stir for 2h at RT. Hereafter it was cooled to 0°C and left under stirring for 3 days. The reaction was terminated with chlorotrimethylsilane. All solvents for the synthesis were purchased from research chemical suppliers and monomer and solvent purification was done as described elsewhere [129].

Si/SiO₂ (90nm) wafers were either used as received or marked with an index mark system using optical lithography and deposition of Cr/Au in a conventional lift-off process. The wafers were cut into 1.5x1.5 cm dies and sonicated in acetone for 2 min, followed by isopropanol and DI water rinse. Graphite and hBN crystals were

purchased from Manchester Nanomaterials or HQ Graphene. They were exfoliated onto Si/SiO₂ substrates with semiconductor die sawing tape (Nitto Denko) after a plasma pre-treatment (NanoETCH, O₂/Ar, 8W, running pressure 1.5x10⁻² mbar, 8/16 sccm, 600s or PlasmaEtch PE-50, 120W, -200 Torr, 5 sccm, 8-10 min) to improve adhesion. After exfoliation, the substrates were taken for inspection under an optical microscope, to find suitable flakes for the topographic trench patterns made in polymer resists described below in section 5.2.2.

Formation of ox-PDMS cylinders through soft graphoepitaxy (DSA)

After the formation of the trench patterns, 0.75-1 wt. % PS-*b*-PDMS dissolved in cyclohexane was spin-coated on top of the patterns at 3000 rpm, acceleration 500 rpm/s for 60 s with a static dispense method. The samples were then solvent vapor annealed (SVA) in toluene (approx. S/V = 0.6-0.7 [47]) for 20 min to 20 h at RT with a setup similar to the one described elsewhere [4]. The samples were then subjected to an O₂ plasma etch (Moorfield Minilab 026 (3" cathode), 15W, running pressure: 1.8x10⁻² mbar, 10 sccm, DC bias: 160 V, 20 min or Moorfield NanoETCH (6" cathode), 30 W, running pressure: 1.2x10⁻² mbar, 13.5 sccm, DC bias: 216 V, 15-20 min). This will remove the PS block and oxidize the PDMS into hard silicon oxycarbide cylinders (ox-PDMS) on top of the 2D material. Hereafter, the polymeric resist was removed and the samples were rinsed as described below in section 5.2.2. Lastly, some samples were furnace annealed at 450-500°C for 1.5-3h in 3% H₂/Ar to remove residual PS and resist.

5.2.2 Topographic guiding patterns

Topographic trench patterns were produced after flake exfoliation by either direct laser writing, electron beam lithography (EBL) or thermal scanning probe lithography. The procedures for the different techniques are described below

Direct laser writing

Direct laser writing was done using, Suss Microtech Laser writer a photolithography technique using a 405 nm laser source to expose the desired trench pattern onto the substrate. After exfoliation, the substrates were spin coated at 3000 rpm, 1000 rpm/s for 60 s with Microposit S1805 positive resist resulting in a film thickness around 150-200 nm. The resist was baked on a hot plate at 110°C for 3 minutes. The main component in the S1805 resist is propylene glycol monomethyl ether acetate (PGMEA).

For the laser writing, lenses 4 or 5 where used with the 3% filter to produce trench patterns with width sizes ranging from 1.5-20 μm and spacing between each trench of (the mesas) $\leq 2 \mu\text{m}$ wide. The pattern creation was done with the pad/edge feature from the PhotonSteer software. After laser exposure, the patterned samples were developed in Microposit MF-319 developer for 50-60 s and afterwards thoroughly rinsed in deionized (DI) water.

Samples made with the laser writer were all prepared at the NGI in an ISO5/class 100 clean room at 20°C.

Electron beam lithography

EBL was done using a Raith eLINE Plus EBL system. The eLine is a dual-use SEM and EBL variable voltage exposure tool. The pattern fabrication was performed by EBL-trained colleagues with the following exposure parameters, aperture: 10 μm , acceleration voltage: 30 kV, current: 45.5 pA and dose: 160 $\mu\text{C}/\text{cm}^2$.

After exfoliation, the substrates were spin coated with a PMMA(950K), 4 wt. % in anisole solution, at 2000 rpm, 500 rpm/s for 60 s resulting in a film thickness around 150 nm. The sample was then baked on a hot plate at 180°C for 2 minutes before EBL exposure. After exposure, the samples were developed in IPA and rinsed in DI water.

Thermal scanning probe lithography

Thermal scanning probe lithography (t-SPL) was done using a NanoFrazor from Heidelberg instruments. This method uses a sharp tip, similar to an AFM tip, which is heated to 800-1200°C via resistively heated elements in the cantilever. The tip is then put in contact with a temperature-sensitive resist, which will be decomposed in nanometer-sized areas and a wide range of patterns can be obtained [157].

After exfoliation, the substrates were spin coated at 2000 or 6000 rpm, 500 rpm/s for 60s with the AR-P 617.03, Poly(methylmethacrylate-co-methacrylic acid), in short, PMMA/MA (67%/33%) 3 wt. % in Propylene glycol methyl ether (PGME) resulting in a film thickness around 140 or 90 nm. The film was baked on a hot plate at 180°C for 5 minutes. Trench patterns, 10-20 μm in length and 1-2 μm in width were produced with a

Trench transfer into 2D materials

In some cases (for route 1, described in section 5.3), the produced trench patterns were transferred into the 2D materials via a plasma etching step (described as route 1 in section 5.3). For graphite flakes, this was done in a Moorfield NanoETCH system in an O_2/Ar gas mixture (8W, running pressure: 1.2×10^{-2} mbar, 8/16 sccm, 30s +10s for each graphene layer, returned to base pressure after each cycle). For hBN samples, this was done in a Moorfield Minilab 026 with SF_6 gas (20W, running pressure: 7.7×10^{-3} mbar, 5 sccm, DC bias: 30 V, 10-100s). For these SF_6 gas parameters, the etch rate of hBN, PMMA and PMMA/MA was found to be 2.25, 0.64 and 0.75 nm/s, respectively.

The resists were usually removed after the BCP nanopatterning process by putting the samples in 1) acetone, 2) isopropanol (IPA) and 3) DI water.

5.2.3 Transfer methods

Si/SiO₂ substrates containing exfoliated graphene or hBN flakes were searched for smooth thin flakes that could be transferred on top of the flakes containing ox-PDMS cylinders (target flake). Graphene flakes were transferred by a wet transfer similar to the one described in [77]. A PMMA (950K, A4) is spin coated on the Si/SiO₂ substrate containing the flakes that need to be transferred. The PMMA-covered sample is then subjected to a potassium hydroxide (KOH) solution overnight in order to etch the SiO₂ layer slightly and free the PMMA/2D flake layer which can be caught by a membrane.

hBN flakes were transferred by a dry transfer using cellulose acetate butyrate (CAB) as described in [78]. Here a CAB solution is spin coated on the substrate containing the flakes for transfer and baking. The flake for transfer is cut out with a scalpel. Adding a drop of water will wedge the substrate and slowly lift the CAB with the flake from the SiO₂ substrate. The CAB with the flake for transfer is picked up by a glass slide with PDMS and ready to be dropped down on the target flake.

After having the flakes for transfer on either PMMA membranes or CAB, the actual transfers to the target flakes are done under an optical microscope and with a micro-manipulator. The two flakes are aligned and afterwards, the transferred flake is dropped down on the substrate with the target flake while a bake, below but close to the T_g of PMMA or CAB, ensures good adhesion between the two flakes. After the transfer, the substrate is rinsed in ethyl acetate (only for CAB), acetone and IPA.

5.3 Results and discussion

The proposed nanofluidic device composed of hard silicon oxycarbide cylinders (ox-PDMS) encapsulated in 2D materials is illustrated in Figure 24A and B. Closed nanochannels wherein e.g. water- and ion flow can be measured, will be created with the ox-PDMS cylinders and the 2D materials as walls. Since the oxygen, plasma step

suggested by the BCP nanopatterning procedure in chapter 4 is plus 15 minutes, the ox-PDMS channels are expected to withstand a hydrophilic surface [154]. The black arrows and dotted lines indicate how a flow e.g. of ions can pass through the ox-PDMS/2D material channels and out through a small hole in the SiN membrane and then be measured.

The first step in the fabrication of this device is to produce a bottom 2D material with highly ordered ox-PDMS cylinders over a large area, around $1.5\ \mu\text{m}$ times $10\ \mu\text{m}$ or bigger. By pre-patterning, the bottom 2D material with topographical guiding patterns made from disposable resists, a DSA of PS-*b*-PDMS can be performed on top of the 2D material. This will provide a high degree of ordering over areas limited by the trench dimensions.

The topographical guiding patterns, in the form of multiple trenches aligned next to each other, were produced using three different lithography techniques described in section 5.2.2. Hereafter, two routes were tested for the DSA of PS-*b*-PDMS to obtain highly ordered ox-PDMS cylinders over large areas, on exfoliated 2D materials as illustrated in Figure 25. Route 1 (1A-1C) included a pattern transfer into the 2D material done by either an O_2 or SF_6 plasma etch dependent on the 2D material (1A).

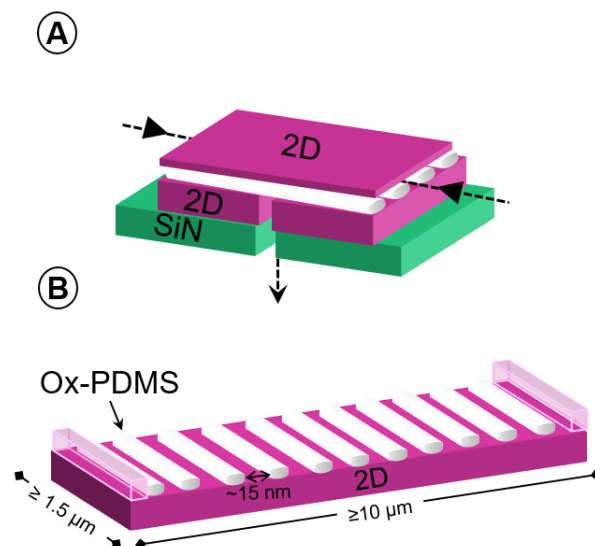
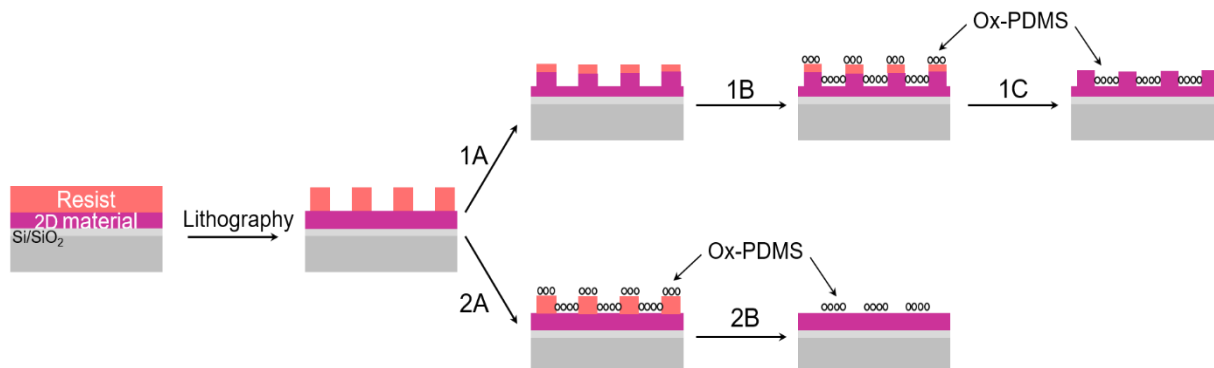


Figure 24: Sketch of a nanofluidic device.

A) Shows the ox-PDMS cylinders encapsulated in between 2D flakes creating narrow channels. The device is placed on a SiN membrane with a $1\ \mu\text{m}$ in diameter hole used for various flow measurements. **B)** Shows the optimal design of the bottom 2D material with ox-PDMS cylinders on top. The transparent walls represent the topographic pre-patterns.



*Figure 25: Schematic showing the two routes, 1. (1A-1C) and 2. (2A-2C) to obtain highly ordered ox-PDMS cylinders over large areas, on exfoliated 2D materials. The lithography step is described in the experimental section, 5.2.2. Route 1. Step 1A) O₂ or SF₆ plasma etch to transfer the trench pattern into the 2D material flake. 1B) Formation of ordered ox-PDMS cylinders via DSA of PS-*b*-PDMS using the trench patterns. 1C) Resist and excess BCP removal. 2A) Formation of ordered ox-PDMS cylinders through the DSA of the PS-*b*-PDMS directly done with resist trench patterns. 2B) Resist and excess BCP removal.*

The next step was the formation of ordered ox-PDMS cylinders via DSA of PS-*b*-PDMS using the trench patterns (1B). Lastly, the resist from the lithography process was removed together with excess BCP on the mesas (1C). In route 2 (2A-2B) the formation of ordered ox-PDMS cylinders through the DSA of the PS-*b*-PDMS was done directly with the trench patterns made in the resist (2A).

Hereafter the resist and excess BCP were removed (2B). Route 1 resulted in ox-PDMS cylinders inside trenches of the flake while route 2 resulted in periodic areas (width around 1-2 μm) on the flake containing ordered ox-PDMS cylinders.

Optical microscope images of flakes pre-patterned by the different techniques and taken through routes 1 or 2 are found in appendix C1-3 and an example is seen in Figure 26A-D. It is noted that even from optical microscope images, the BCP seem to stay after the resist removal, see Figure 26D.

To achieve a monolayer of highly ordered cylinders, the trench depth should be approximately 1-1.5 times the natural period (L_0), of the BCP [158]. For graphite flakes, this meant etching approximately 100 layers (34 nm) and around 120 layers (40 nm) for hBN.

In principle, during the SVA process, the PS-*b*-PDMS should migrate into the trenches leaving no PS-*b*-PDMS on the mesas [39, 158]. However, from initial experiments, where the resist was removed right after step 1A, the presence of ox-PDMS cylinders was found both in the trenches and on the mesas as seen in appendix D4. Waiting with the resist removal until after the formation of ordered ox-PDMS

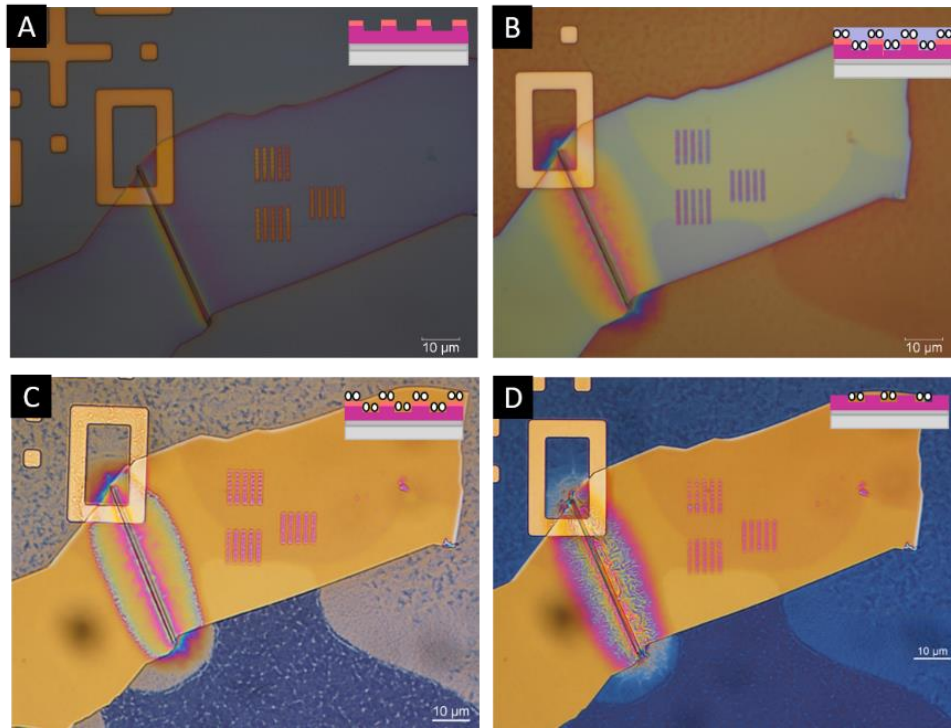


Figure 26: Optical microscope images of an hBN flake with trenches made through thermal scanning probe lithography. A) After a SF_6 etch have transferred the trench pattern into the flake, step 1A. B) After SVA of the BCP thin film, step 1B. C) After O_2 etch to remove PS, step 1B. D) After resist removal, step 1C.

cylinders, left no ox-PDMS cylinders on the mesas as seen later in Figure 29A. Additionally, from optical microscope images taken during all the steps in the DSA process, no terrace formation inside the trenches was observed.

In the following sections, samples made using the three different lithography techniques, E-beam, direct laser writing and t-SPL are presented.

5.3.1 Trench patterns made with E-beam lithography

A graphite flake pre-patterned with e-beam lithography and subsequently taken through route 1A was produced with trench width sizes ranging from 200-500 nm and mesa widths of approximately 500 nm. Figure 27 shows SEM and cross-sectional STEM images of the flake. It should be noted that most of the resist was removed doing step 1A and as seen in Figure 27A the mesas have not been free from BCP residues. Figure 27B and Figure 27C show the ordering of cylinders parallel to a 200 nm and 500 nm trench respectively. This orientation of the ordering suggests that the graphite walls favor either PS or PDMS. It is clear, that there is a big variation in the patterns even over small areas ($<1\ \mu\text{m}$) as seen in Figure 27A. However, the cylindrical ordering seems to only be present in the trenches while a disordered- or spherical forming state is found on the mesas. Figure 27D is a cross-sectional STEM image showing the presence of nanopatterned graphite. The patterning is most pronounced in the trenches and a magnified image of this area is seen in Figure 27E. For the graphite patterns, a period of 34 nm and a height of 54 nm was found and no indication of a silicon-containing polymer was observed. This indicates that the oxygen plasma procedure when removing the PS block was too harsh, etching through the graphite while the ox-PDMS cylinders acted as a hard template until also etched away leaving no polymer residues. Although this was not intentional, it demonstrates a way to obtain residue-free nanopatterning of multilayer graphene.

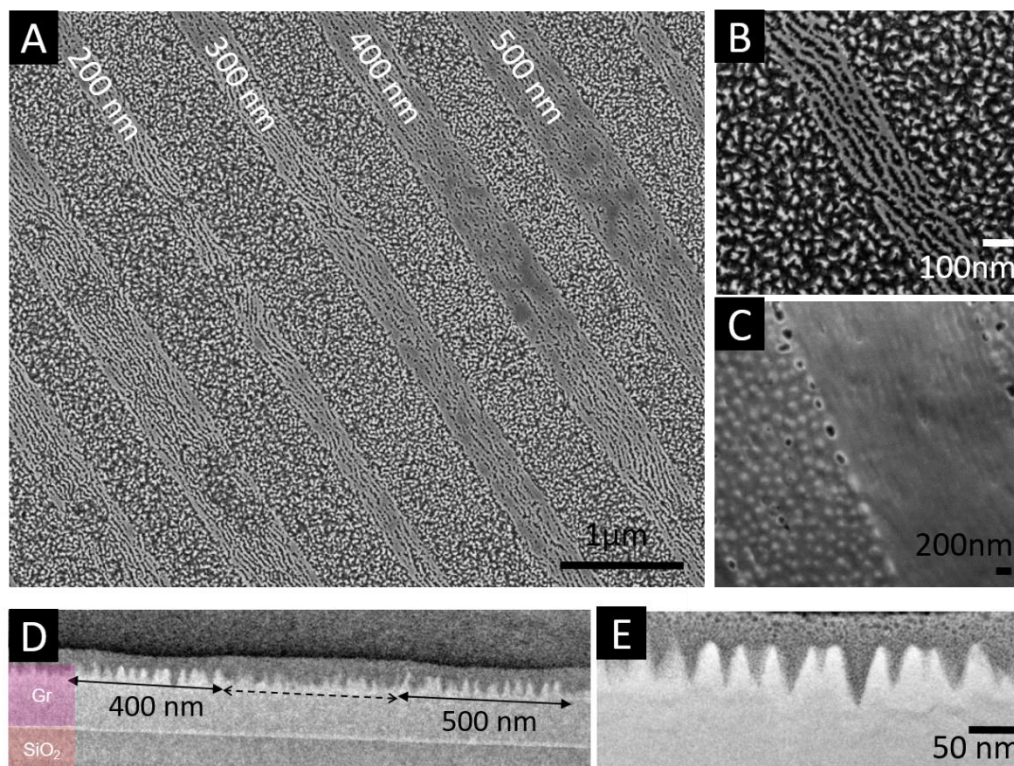


*Figure 27: Graphite flake after e-beam lithography and route 1. SEM images **A)** showing the different trench widths (200-500 nm) and the ox-PDMS ordering. Ox-PDMS ordering in **B)** a 200 nm trench and **C)** a 500 nm trench. Cross sectional STEM images showing **D)** nanopatterned graphite in the 400 and 500 nm trenches and **E)** graphite patterns with a period of 34 nm and a height of approximately 54 nm. The dotted line in **D)** indicate the mesa.*

On another sample, hBN flakes were pre-patterned with e-beam lithography and subsequently taken through route 1. For this sample, the PMMA resist survived the SF_6 etching of the hBN (step 1a) and the mesa heights were found to be around 100-150 nm after step 1a with so-called batwings at the mesa/trench edges [159]. These heights were expected to produce PS-*b*-PDMS bi- or trilayers. Figure 28, shows an AFM height and phase image of one of the hBN flakes with a trench width of around 1.75 μm . In contrast to the graphite sample, this shows non-selective sidewalls which resulted in highly ordered cylinders with a period of 38.2 nm, oriented perpendicular to the trench walls as seen most clearly in the AFM phase image in Figure 28A. The

non-selective sidewalls are suggested to be due to the presence of PMMA, which has been reported to be non-selective towards PS-*b*-PDMS before [42]. Notably, from the height image, the surface in the trenches is uneven with areas of varying heights, some around 50 nm higher than others, see Figure 28B. This height difference was already seen from an optical microscope inspection of the trenches, see appendix D1. The height difference could originate from the SVA process which might affect the residue resist, leaving resist residues beneath or on top of the trenches. Another more plausible explanation is that the trenches were too deep (100-150 nm) resulting in the formation of a multilayer PS-*b*-PDMS film, which is responsible for the unevenness. A schematic of this is found in appendix D5. From the optical microscope images, found in appendix D1, interesting micropatterns are observed including what

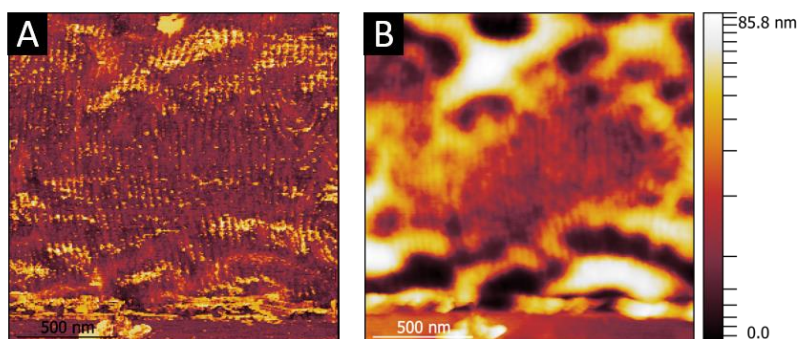


*Figure 28: AFM **A)** phase and **B)** height images of ox-PDMS cylinders formed in an hBN trench made from EBL. The perpendicular alignment of the cylinders is believed to originate from the presence of PMMA at the sidewalls.*

look like bridges between the trenches. This phenomenon was only observed on samples with PMMA(950K) resist and seem to appear after the SVA procedure, suggesting an interaction between the PMMA resist layer and the PS-*b*-PDMS during this process. However, this was not further investigated.

5.3.2 Trench patterns made with photolithography

Trench patterns made with direct laser writing were in general bigger than $1.5\ \mu\text{m}$ and the width precision was limited due to the instrument resolution. To find the optimal trench width, different width sizes from $1.5\ \mu\text{m}$ to $20\ \mu\text{m}$, were investigated. It was found that for trench widths larger than $2\text{-}2.5\ \mu\text{m}$, the BCP film started to become inhomogeneous and form terraces resulting in low-ordering or disordered structures. Therefore, trench widths were kept around $1.5\text{-}2\ \mu\text{m}$.

With the laser writer, only samples with graphene flakes were prepared through route 1. Figure 29 shows SEM images of a trench made on a graphene flake through laser writing and route 1. Figure 29A shows that the mesas are free of any BCP microstructure residues after resists removal. This was the case for all samples with trenches made from laser writing. Figure 29B shows an SEM image of the trench wherein, non-ordered horizontal ox-PDMS cylinders are found. The orientation of the features indicates non-selective sidewalls. Again, this was believed to be caused by the resist whose main component is PGMEA. A narrow area containing a higher concentration of defects is observed at the edges of the trench patterns. This is caused

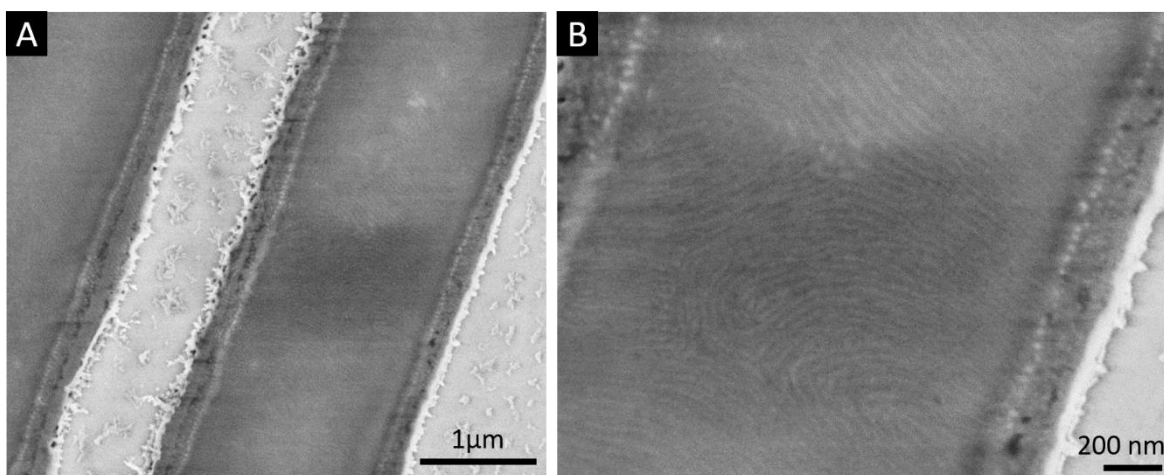
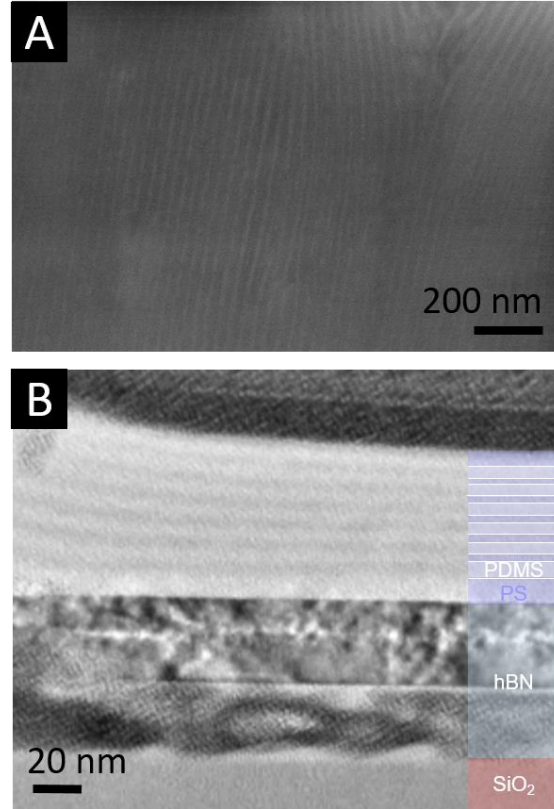


Figure 29: Trench with ox-PDMS made through route 1 in graphene with laser writing. A) The mesas are free of BCP residues. B) non-ordered ox-PDMS cylinders are found inside the trenches.

by the roughness of the trench edges originating from the lithography procedure. The trenches, with the ox-PDMS cylinders, were observed to be approximately 30 nm higher than the mesa centers and further AFM measurements showed the presence of 50 nm high batwings at the mesa/trench edges. The height difference between the trenches and mesas indicates the presence of a multilayer PS-*b*-PDMS film inside the trenches. This will be further investigated below.

Samples with hBN flakes were prepared with laser writing through route 2. Figure 30A shows an SEM image of nicely ordered ox-PDMS cylinders, again normal to the trench length. The ordering extended beyond 2.5 μm of the length with minimal defects. However, from AFM images, the trenches were again found to be higher than the mesas (around 100 nm). In Figure 30B a TEM image of a cross-sectional lift-out reveals the presence of a multilayer film of PS-*b*-PDMS. The lift-out was made perpendicular to the trench lengths and hence parallel to the ox-PDMS ordering. The dark lines in the multilayer on top of the hBN flake represent the PDMS cylinders with a 13nm layer spacing $\sim L_0/2$. The 76.4 nm thick film, corresponding to 6 layers of PDMS cylinders, survived a total of 30 W O_2 etching for 20 min with a resist removal



*Figure 30: Images from trenches made with laser writing through route 2. A) SEM image of highly ordered ox-PDMS cylinders on top of an hBN flake. B) Cross-sectional TEM image of same flake as is A) showing the presence of multilayer PS-*b*-PDMS on top of hBN.*

step after the first 10 min. The hBN flake beneath also survived in the areas where the trenches were. However, after resist removal, the part of the hBN flake that was the mesas did not survive the subsequent etching. Additionally, from Figure 30B it is noted that hBN favors PS wetting at the hBN/BCP interface which is in agreement with the results found in section 4.1.1.

For many of the samples with trenches made from laser writing, a difference in the orientation of the ox-PDMS cylinders (vertical or horizontal) was observed. This was seen from flake to flake, and even sometimes from trench to trench. The shift in the orientation of the ox-PDMS cylinders could be caused by the presence of an underlying non-selective layer, possibly the resist, or a change in film thickness from the optimal $\sim L_0$ as described previously [36]. Considering that all resist residues should have been removed during the development and/or the etching step 1a, the latter seems to be the most plausible.

In some trenches, the coexistence of horizontal and vertical ox-PDMS cylinders was observed. Often the horizontal alignment was seen at the trench edges and when going towards the center of the trench, this alignment turned into a vertical orientation, see appendix D6. This again indicates that the shift in orientation is caused by changes in the film thickness. The domain periods found for the vertical cylinders were in general a bit lower (33.2 nm) than the period in the horizontally aligned cylinders (36.5 nm), but still close to L_0 found from STEM analysis in section 4.1.1.

However, it is noted that a previous study using PGMEA as a solvent during the SVA process has reported a shift in the morphology of PS-*b*-PDMS from cylindrical to spherical [4]. It might be that a similar thing occurs in this case during SVA since PGMEA is present through the resist. However, the majority of the trenches made from laser writing showed horizontal cylinders, indicating the presence of PGMEA had no influence during SVA.

5.3.1 Trench patterns made with t-SPL

Samples with trenches made from t-SPL only concerned hBN flakes. Trench widths of 1, 1.75 and 2 μm were made with lengths ranging from 10-20 μm . No big difference was observed in the order when changing the trench widths. The use of t-SPL made it easier to control the actual depths of the trenches, especially for route 2 samples. Etch rates of PMMA/MA and hBN in SF_6 gas (20W, 5 sccm, DC bias: 30 V) were found to be 0.75 nm/s and 2.25 nm/s, respectively. An initial SVA test in PMMA/MA resist trenches on hBN showed a very bad ordering of the ox-PDMS cylinders compared to previous results in trenches of PMMA resist seen in section 5.3.1. This suggests that the presence of MA reduces the mobility of the BCP during SVA which would mean longer SVA times are required. Samples with SVA times of 20 min, 30 min, 1h, 3h and 20h were made. Figure 31A shows an AFM height image from an hBN flake patterned with t-SPL through route 1 with an SVA step of 1h. Highly ordered ox-PDMS cylinders, parallel to the trench length, are observed inside the trenches. This suggests that the hBN sidewalls favor one of the blocks, probably PS as previously observed through cross-sectional lift outs. However, in general, for most of the trenches made with t-SPL, the alignment of the cylinders was found to vary from trench to trench and within the trenches showing mixtures of parallel and

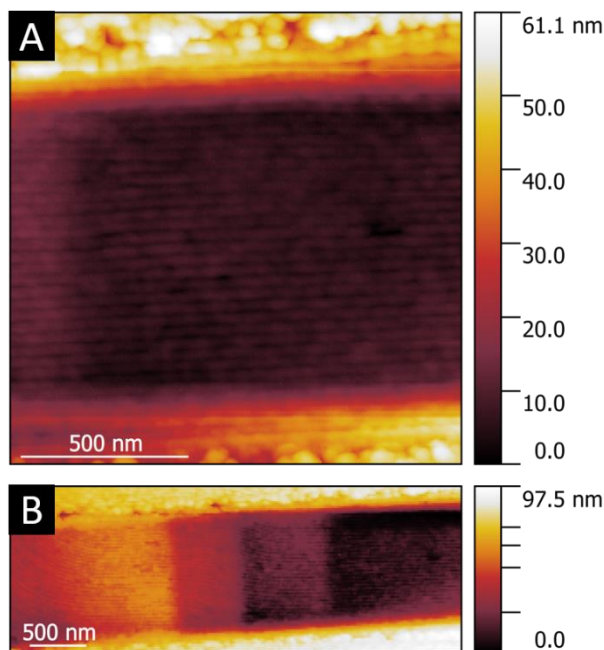


*Figure 31: AFM height images taken before resist removal **A)** showing the ordering of ox-PDMS cylinders in an hBN trench made from route 1 after 1h SVA. **B)** showing how the ox-PDMS ordering extents more than 3 μm of the length of the trench*

perpendicular alignment. This is believed to be caused by the presence of residue PMMA/MA resist. Furthermore, no difference in the ox-PDMS cylinder orientation was found for any of these samples.

It was found that 20 and 30 min SVA was too short for these samples to obtain the desired ordering. However, for SVA times of 1h or longer, improved ordering over long ranges ($>1\text{ }\mu\text{m}$) was observed as seen in Figure 31B. Here the parallel alignment extends along the length of the trench for more than $3\text{ }\mu\text{m}$. The bumps seen inside the trench originate from the feedback mechanism in the t-SPL patterning. When the patterning is initialized, the t-SPL system learns from a feedback mechanism to improve its patterning while running. The outcome of this is a slightly uneven patterning at the beginning of the patterning process. With that said, the ordering and defect concentration of the ox-PDMS cylinders does not seem to be influenced by this.

The possibility of removing the PMMA/MA resist after the O_2 plasma etching was observed to be dependent on the etching time. Samples etched for less than 15 min were found to lose both the resist and the BCP when dipped in acetone. However, when etched for 15 min or more, the BCP patterns stayed. Figure 32A shows an AFM height image and a vertical profile of an hBN flake before resist removal. The presence of 30-50 nm resists on the mesas is observed together with batwings from the t-SPL process. Figure 32B shows an AFM height image and vertical profile of the same flake after resist removal. Most of the residues from the mesas are removed and the batwings are cut down a bit. The cylindrical patterns inside the trenches do not seem to change with the removal of the resist. Nevertheless, some residues still remain, but were found to be reduced significantly after a furnace annealing step at $450\text{-}500^\circ\text{C}$ in a flow of 3% H_2/Ar . For the flake shown in Figure 32, the trenches are believed to contain 2 or more layers of cylinders due to the 20 nm height difference between the mesa and trenches seen after resists removal. This could also explain the lower ox-PDMS pattern quality which previously has been observed to be a consequence of the presence of cylindrical bilayers [4].

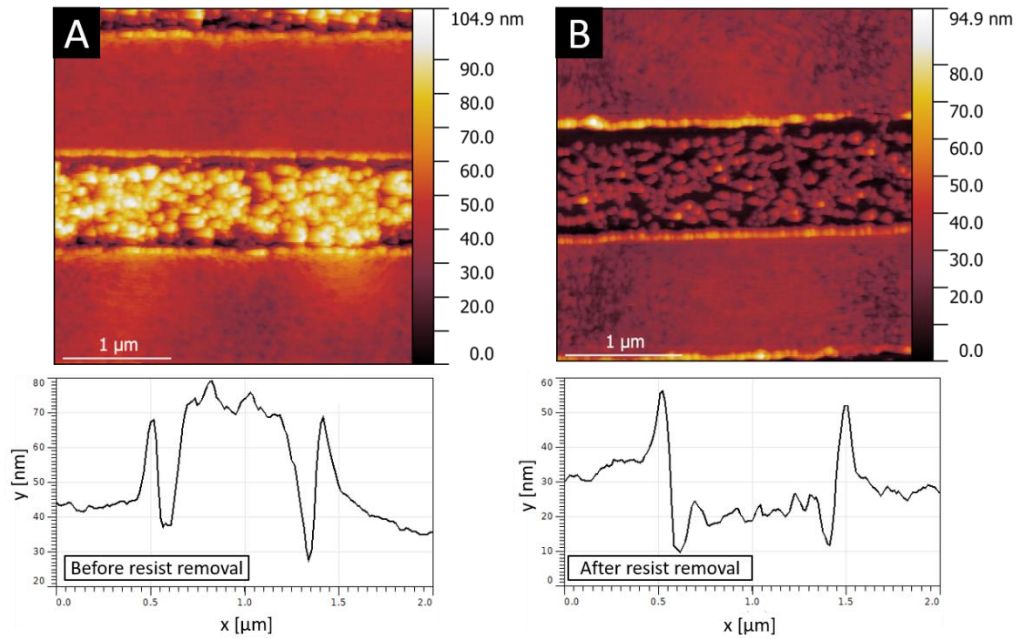


*Figure 32: AFM height images of a sample **A)** before resist removal and **B)** after resist removal. The bottom graphs show the vertical profiles from each of the two images.*

5.3.2 Transfer

To fabricate the desired nanofluidic device explained in section 5.3, it is necessary to investigate the transfer of 2D materials on top of these ox-PDMS patterns as well as the transfer of the ox-PDMS patterns to other substrates.

First, it was investigated how graphene of different thicknesses would conform to the trench samples and enclose the ox-PDMS channels. Figure 33A shows an optical microscope image of two graphene flakes with various layers thicknesses which were used for the transfer to hBN trench samples fabricated through route 2 with laser writing, see Figure 33B. The graphene flakes were transferred on top of the trench samples through wet transfer as described in section 5.2.3. Figure 33C shows the result of the transfer after annealing at 150°C and cleaning in acetone.

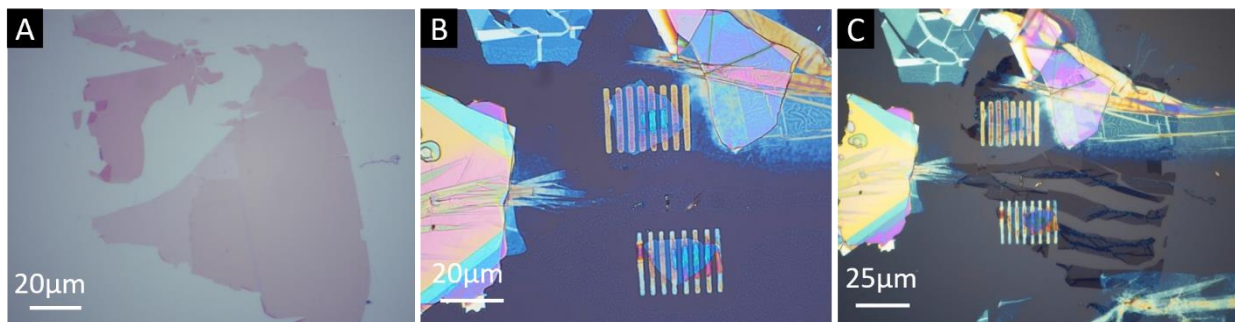


Figure 33: A) Optical microscope image of large graphene flakes with different layer thicknesses used for transfer to trench samples seen in B). B) Optical microscope image of hBN flake with trenches made from laser writing containing ordered ox-PDMS cylinders. C) Optical microscope image of same area as seen in A) just after wet transfer of the graphene flake.

The first thing to notice is that the graphene flakes were ripped apart doing the annealing step which is very surprising when considering the mechanical strength of graphene. Even more surprising is that, the cracking does not seem to be caused by the few nm tall trenches since the direction of the cracks is perpendicular to the trench length. However, the presence of other polymer residues (as seen in Figure 33B) which swells doing the thermal annealing might be the explanation for the cracks.

Fortunately, some areas with trenches were covered by graphene and the conformation to the surface was investigated by AFM imaging. Figure 34A shows an AFM height image of a trench containing ox-PDMS cylinders, aligned normal to the trench walls which is clear from the AFM phase image seen in Figure 34B. From the top right corner and down the diagonal a graphene flake covers the trench. The flake is nicely conformed to the trench surface and the ox-PDMS cylinder patterns are observed through the graphene flake cover. Height profiles from an area not covered by the graphene flake and an area covered by the graphene flakes are shown in Figure 34C and D. From these, the periodicity of the ox-PDMS cylinders are observed in both

areas concluding that graphene sags in-between the ox-PDMS cylinders creating small nm channels for future fluidic devices.

Another transfer of an hBN flake to an hBN flake containing trenches made with t-SPL through route 1 was performed. An optical microscope image of the result is found in appendix D7. The transferred flakes only covered parts of the trenches and the conformation of the hBN flake to the trench surface was investigated by AFM. Figure 35A shows an AFM height image of a bottom hBN flake containing trenches with ox-PDMS cylinders with a transferred hBN flake on top. From this image, the conformation of the hBN flake to the trench/mesa surface is clear and further confirmed by the two vertical height profiles from different areas (non-covered and covered by top hBN). Figure 35B is an AFM phase image showing the edge of the top hBN covering ox-PDMS cylinders. From this, no conformation of the top hBN to the ox-PDMS cylinders is observed. However, this is likely due to the thickness of the transferred hBN (~ 30 nm) which ideally should have been a few times smaller than the distance between the cylinders.

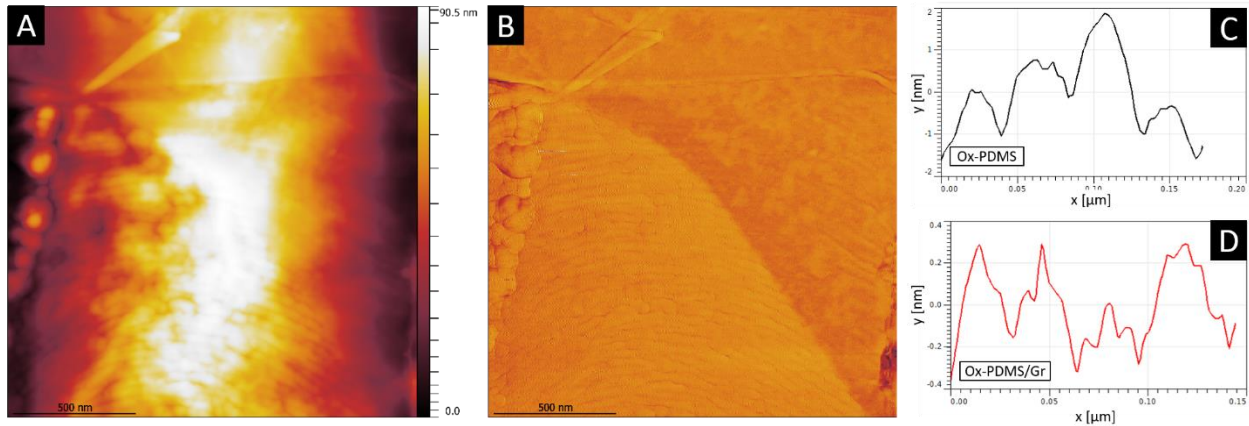


*Figure 34: AFM **A)** height and **B)** phase images of a trench with ox-PDMS cylinders normal to the trench walls. A graphene flake covers almost half of the trench, from the top right corner and down to the middle. **C)** Height profile from an ox-PDMS area not covered by graphene. **D)** Height profile from an ox-PDMS area covered by graphene.*

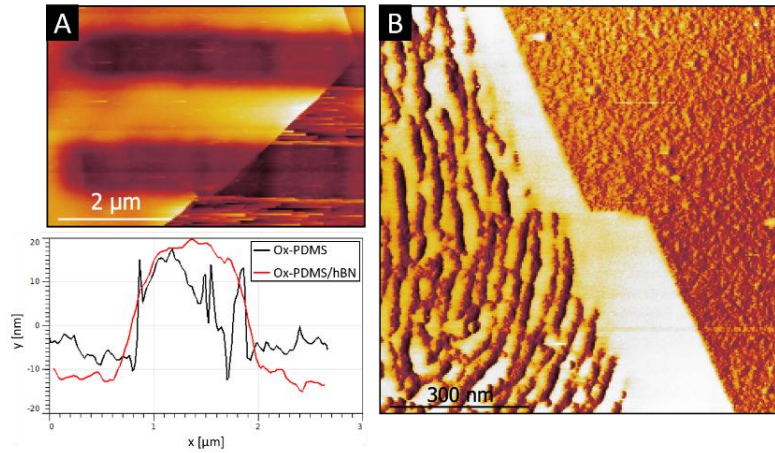


*Figure 35: AFM **A)** height image of an hBN flake containing trenches with ox-PDMS cylinders with a transferred hBN flake on top (from the left). The graph show two vertical height profiles, one from the area where the trenches and mesa is not covered by the top hBN flake (black) and one from the area where the trenches and mesa is covered by the top hBN flake (red). **B)** Phase image from the edge of the top hBN flake covering the ox-PDMS cylinders.*

Lastly, the transfer of the 2D materials containing the ox-PDMS cylinders was investigated to see if the patterns could survive a transfer procedure. For this, a wet transfer of a flake containing ox-PDMS cylinders was performed as described in section 5.2.3. The initial trial suggest that the patterns can survive; however further experiments need to be conducted to make sure the pattern quality is not damaged. Alternatively a dry etch process might be considered.

5.4 Summary

In this chapter, we have demonstrated the initial steps in the fabrication of a nanofluidic device where silicon oxycarbide nanochannels are sandwiched in-between 2D materials. As the first step, we have investigated possible routes for the DSA of PS-*b*-PDMS, for the first time utilizing disposable positive-tone photoresist and different lithography techniques for soft graphoepitaxy. With these, we obtained ordered silicon oxycarbide (ox-PDMS) cylinders on exfoliated 2D materials and

showed that the patterns persist even after resist disposal. Further, we have reported some challenges, arising from non-optimal trench depths such as the creation of PS-*b*-PDMS multilayers. We further showed how trenches in graphite are selective towards one of the blocks and additionally demonstrated a way to nanopattern multilayer graphene leaving no polymer residues. From our experiments using different lithography techniques, we found that the topographical guiding patterns created using thermal scanning probe lithography (t-SPL), were the most manageable in terms of dimensions. After optimizing the SVA and O₂ etching procedures, this process provided highly ordered ox-PDMS cylinders extending 1 μm times 3 μm on exfoliated 2D materials which can be used in the fabrication of a nanofluidic device combining BCPs and 2D materials. We further showed that these ox-PDMS patterns on 2D materials can be encapsulated by the transfer of another top 2D material. Especially, with the transfer of a top graphene flake, we demonstrated how graphene conforms to the ox-PDMS patterns, which is promising for the creation of a device with nanofluidic channels. With these results, we are one step closer to the fabrication of our suggested nanofluidic device.

6 Conclusion

In conclusion, this thesis has explored the possibilities for BCP nanopatterning of 2D materials as a scalable alternative to high-cost lithography techniques. The thesis has been focused on the synthesis and characterization of a silicon-containing BCP along with its BCP nanopatterning process and applications in combination with 2D materials. The sequential anionic polymerization of PS-*b*-PDMS using monomeric styrene and D_3 has been presented. The molecular weight averages of the synthesized products were determined using standard size-exclusion chromatography (SEC) and compared to a novel method utilizing nuclear magnetic resonance (NMR) for the characterization of silicon-containing BCPs. For the first time, the characterization of PS-*b*-PDMS using a combination of 1H -NMR and 1H - ^{29}Si HMBC NMR has been presented and has shown promising results for narrow-distributed PS-*b*-PDMS products with molecular weights ranging from 19-38 kg/mol.

With the polymerization of narrow distributed PS-*b*-PDMS, the BCP nanopatterning process on 2D materials could be investigated. The BCP nanopatterning process revealed a monolayer of PDMS cylinders in a PS matrix on the surface of mechanically exfoliated hBN flakes with no PDMS wetting layers at any of the interfaces. After the formation of the hard silicon oxycarbide cylindrical template, the pattern was transferred into the hBN flake resulting in a clean, polymer-free nanopatterned hBN surface. Additionally, initial trials on hBN-encapsulated graphene heterostructures showed promising results for the use of the BCP nanopatterning process on such structures.

Lastly, the conjunction of BCPs and 2D materials for the fabrication of a nanofluidic device was investigated. The initial steps in the fabrication of silicon oxycarbide (ox-PDMS) nanochannels sandwiched between 2D materials were demonstrated with soft graphoepitaxy utilizing a disposable positive-tone photoresist for the first time. Through the exploration of the different lithographic techniques, the topographical guiding patterns created using thermal scanning probe lithography (t-SPL) were

found to give the most reliable fabrication results. With these topographical guiding patterns and the aforementioned BCP nanopatterning process, highly ordered ox-PDMS cylinders extending $1\ \mu\text{m}$ times $3\ \mu\text{m}$ on exfoliated 2D materials were produced. Furthermore, the encapsulation and transfer of the ox-PDMS cylinders showed promising results for the fabrication of a nanofluidic device combining ox-PDMS nanochannels and 2D materials.

Our goal has been to establish a path for utilizing BCP nanopatterning to nanopattern or integrate BCPs not only in relation to graphene but also to other mechanically exfoliated 2D materials and heterostructures. With this approach for BCP nanopatterning, a broader range of applications can be envisioned and implemented in a scalable manner which holds great promise for future nanotechnology.

6.1 Outlook

Some of the explored research in this thesis has opened up new project ideas and possible follow-up experiments which are described in the following.

Concerning the synthesis of PS-*b*-PDMS, in situ NMR experiments using ^1H - and ^1H - ^{29}Si HMBC NMR could be performed to further understand the reaction kinetics of this polymerization. This would require a more complex setup since the reaction should be performed in an NMR tube.

Regarding the BCP self-assembly on 2D materials, many other experiments could be performed to investigate other applications. As an example, experimenting with BCPs of various volume fractions, different annealing solvents, and annealing methods can yield new morphologies and orientations, such as spheres and vertical cylinders. Additionally, this could be combined with the findings from the directed self-assembly (DSA) method used for the fabrication of highly ordered silicon

oxycarbide channels and give rise to applications more suited for the semiconductor industry.

The initial work presented on the nanofluidic device fabrication is still ongoing and cross-sectional lift outs of the silicon oxycarbide channels sandwiched between hBN are expected to reveal the presence of nanofluidic channels. Furthermore, to investigate the possibilities and performance of such a device, transport measurements are needed.

The DSA process using t-SPL was performed on an hBN-encapsulated graphene heterostructure without any trapped bubbles, with the goal of nanopatterning graphene through BCP templating. After pattern transfer into graphene, initial AFM results showed promising highly ordered structures. However, this sample was destroyed doing FIB processing and unfortunately, the cross-sectional lift-out did not reveal anything of interest due to a non-ideal FIB procedure. A redoing of this sample would be ideal to further demonstrate the strength of BCP nanopatterning on van der Waals heterostructures.

Appendix

A. Conference contributions

Nanopatterning of 2D materials By Block Copolymer Self-Assembly

Christina Breth Nielsen, Anton Lyksborg-Andersen, Tim booth and Kristoffer Almdal

Oral presentation, EUPOC (2022)

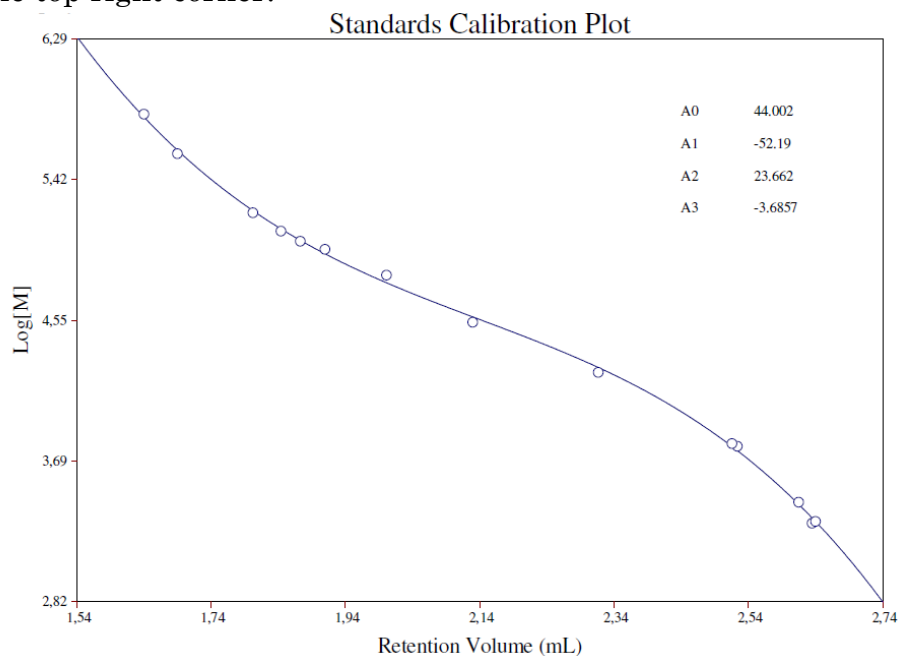
Nanopatterning of 2D materials By Block Copolymer Self-Assembly

Christina Breth Nielsen, Anton Lyksborg-Andersen, Max Rimmer, Radha Boya, Tim booth and Kristoffer Almdal

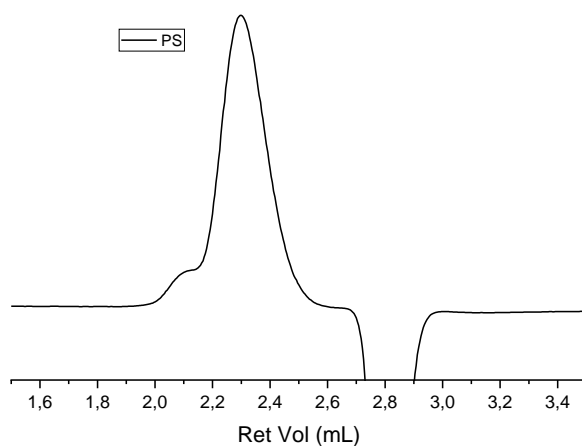
Poster presentation, MNE (2022)

B. Anionic polymerization of PS-b-PDMS

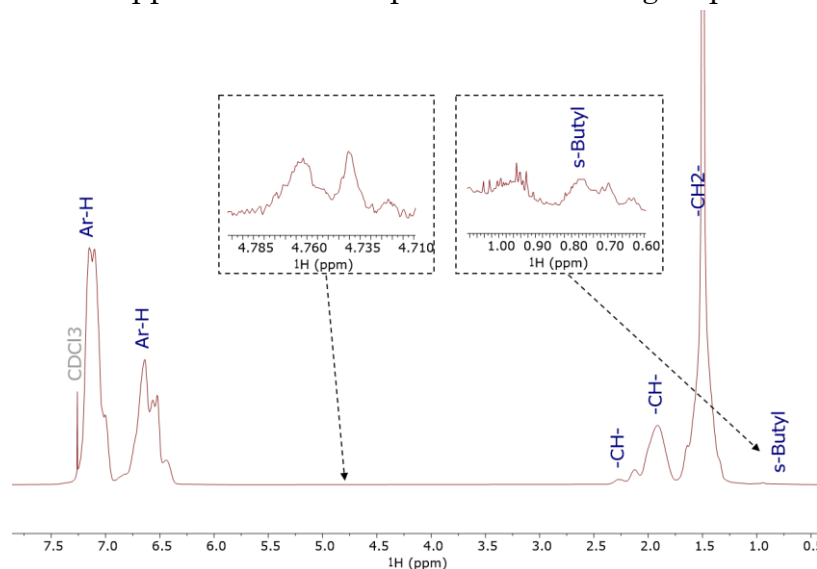
B1: Example of a calibration curve made from SEC measurements of narrow PS standards. It shows $\log(M)$ as function of the retention volume found for each PS standard. A 3rd polynomial function has been fitted and the 4 coefficients are shown in the top right corner.



B2: RI signal from the PS produced in SD19. A shoulder at higher molecular weights is found and believed to originate from a dimeric coupling formation.



B3: ^1H -NMR spectrum of the PS aliquot produced in SD64. The broad resonance signals around $\delta = 4.7$ ppm indicate the presence of $-\text{OH}$ groups.

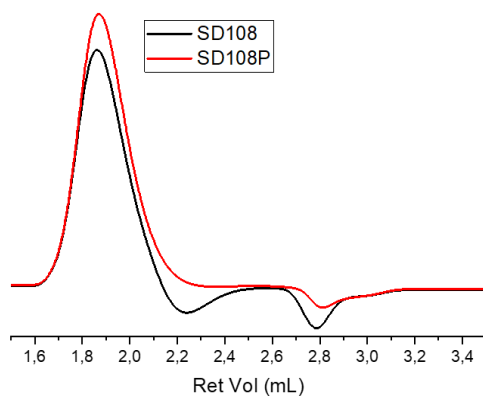


B4: Molecular weight averages of SD19 aliquots measured with SEC RI data.

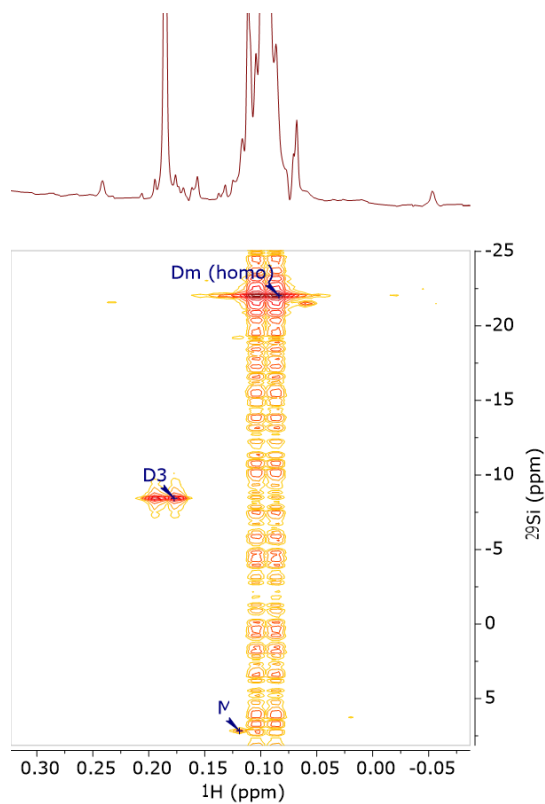
| Reaction time [h] | χ_{NMR}^* | M_n [g]/[mol] | M_w [g]/[mol] | PDI |
|----------------------|-----------------------|-----------------|-----------------|------|
| PS | - | 17100 | 20200 | 1.18 |
| 0.5 | 0 | 16900 | 19700 | 1.17 |
| 1.5 | 0 | 17000 | 20000 | 1.17 |
| 1.75 | 0.733 | 20000 | 23100 | 1.16 |
| 19.5 | 0.771 | 19900 | 23000 | 1.16 |
| 45.75 | 0.834 | 20200 | 23400 | 1.16 |
| 68.5 | 0.833 | 20400 | 23600 | 1.16 |
| 97.5 | 0.887 | 20900 | 23700 | 1.13 |
| 97.75 | 0.868 | 20600 | 23300 | 1.13 |
| 98.5 | 0.892 | 20600 | 23300 | 1.13 |
| 99.5 | 0.895 | 20500 | 23300 | 1.13 |
| SD19 | 0.898 | 18700 | 21000 | 1.12 |

* D3 conversion to PDMS from ^1H -NMR

B5: RI increments before (SD108) and after (SD108P) the sample was washed in n-pentane.

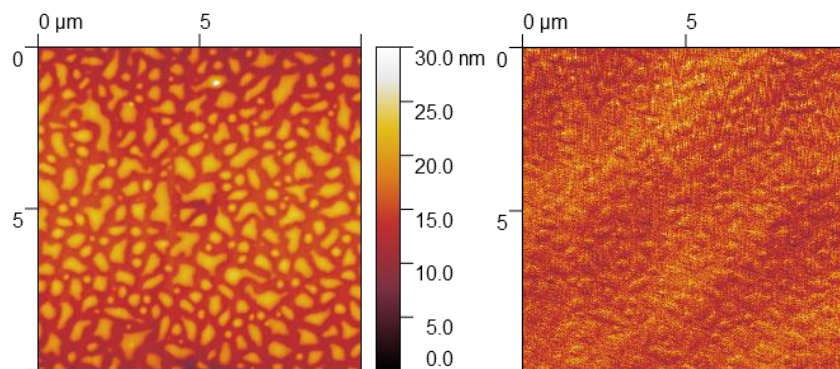


B6: ^1H - ^{29}Si HMBC of liquid phase from the washing of sample SD19 in n-pentane. Signals from PDMS homopolymer, $\text{D}_m(\text{homo})$, and its end-group, M is seen together with a signal from D_3 .

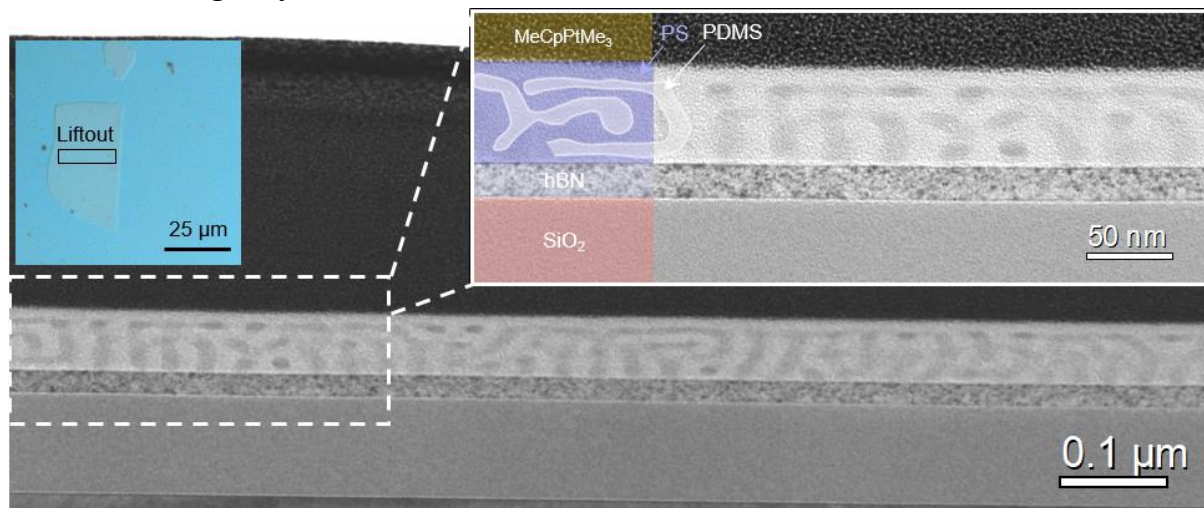


C. Self-assembly of PS-*b*-PDMS on 2D materials

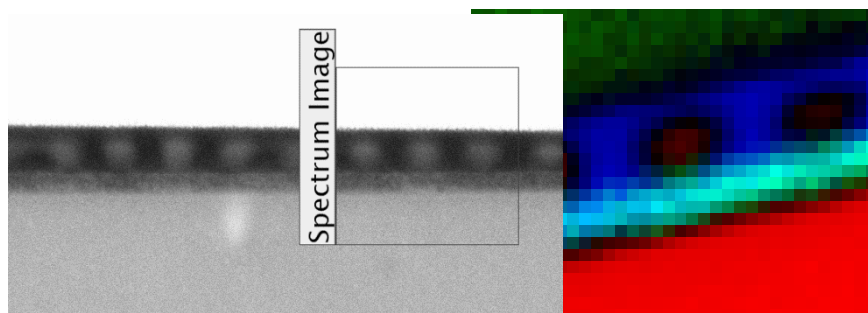
C1: AFM height (left) and phase (right) images revealing ~10 nm tall terraces (islands) appearing after SVA.



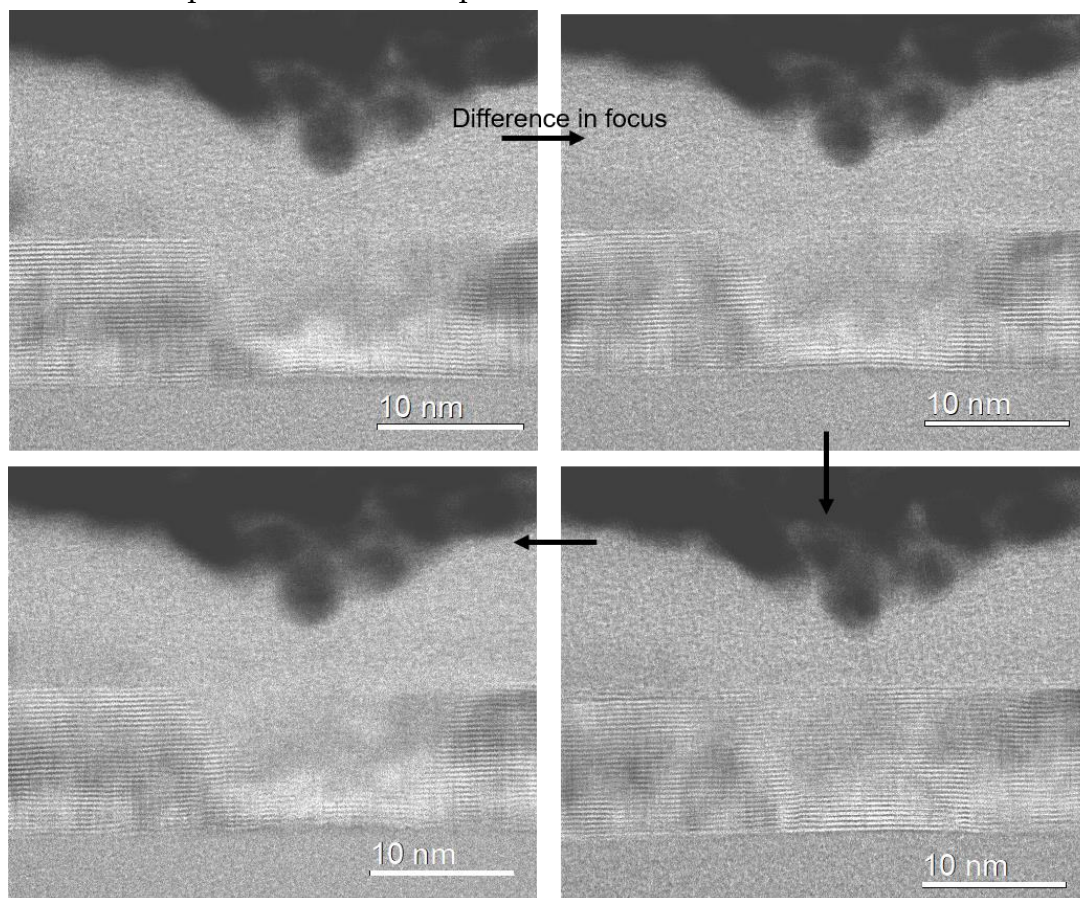
C2: Cross-sectional STEM image of a sample lift-out from smooth region with MeCpPtMe₃ protection on top of PS-*b*-PDMS on a hBN crystal (20 nm thick)/SiO₂ (90 nm)/Si. Figure show a large area with a PS-*b*-PDMS film of 60 nm thickness. The inset shows a optical microscope picture of the crystal where the lift-out was taking from. In the zoomed area it is clear to see that the PDMS cylinders are not ordered and more resembles boiled spaghetti in a PS matrix. However, again no PDMS wettings layers are observed.



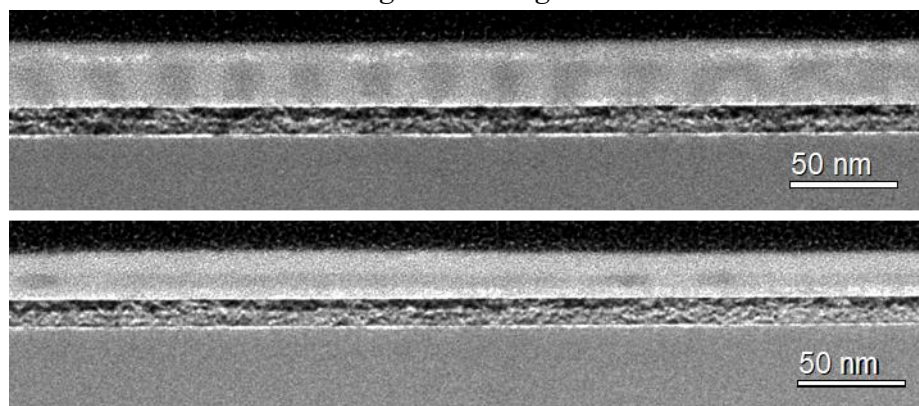
C3: Energy Electron Loss spectrum (EELS) with least square fitting from varying region showing the different elements present from the visible edges (boron and silicon). Turkis= B, Red=Si.



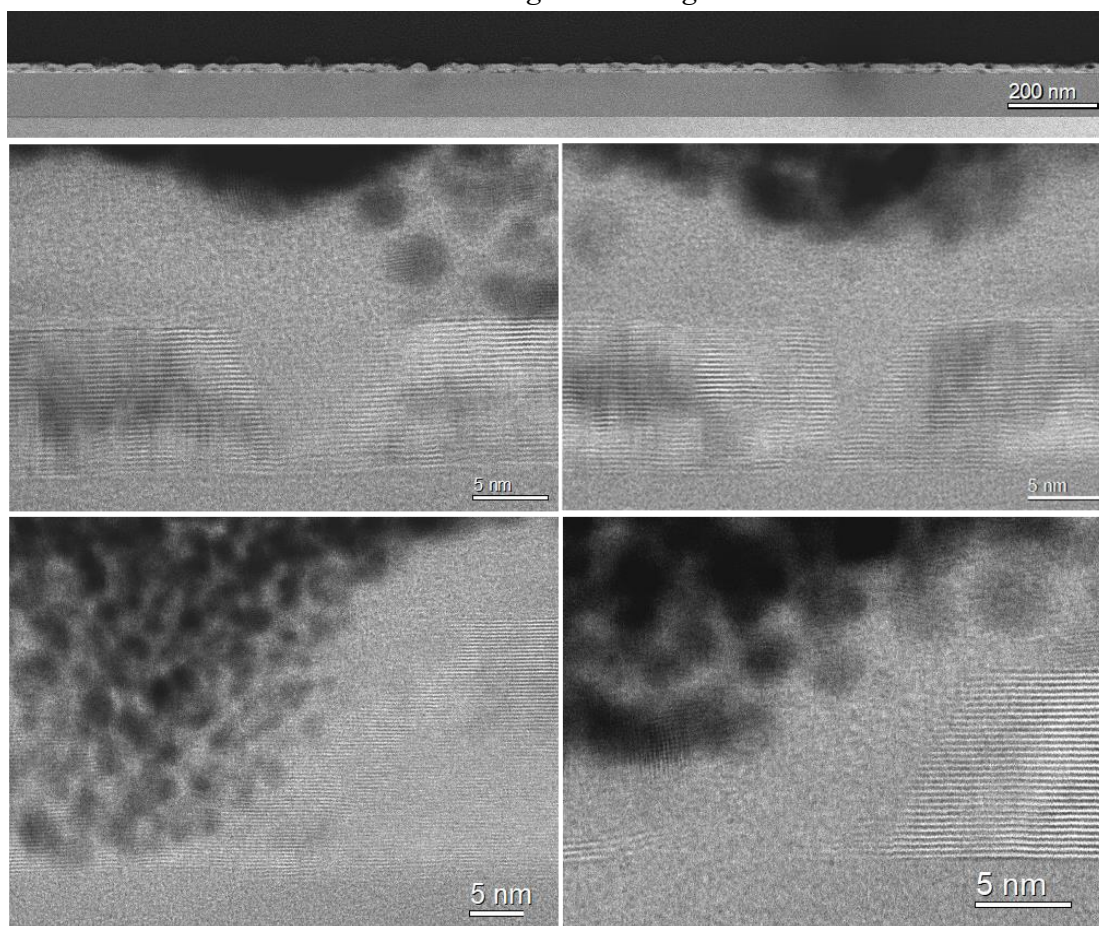
C4: STEM images after SF_6 in hBN of the same area with different microscope focus. Each image show a different projection of the 100 nm thin lift-out and hence confirm the presence of a hole pattern.



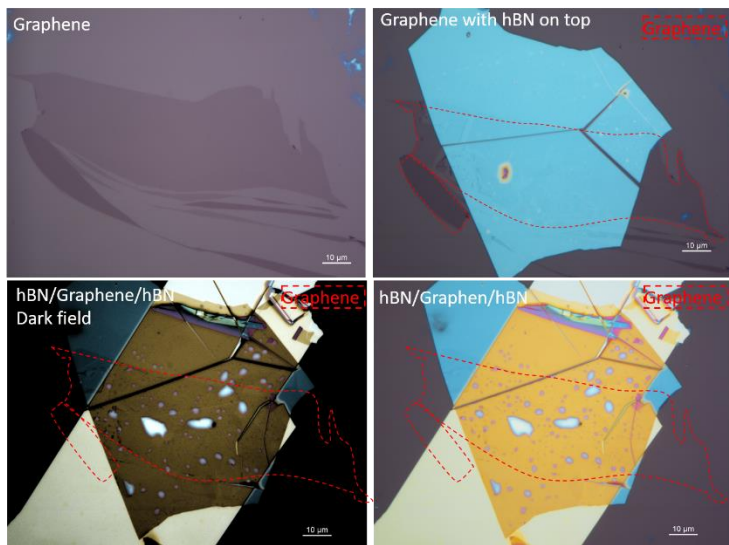
C5: Raw cross-sectional STEM images from figure 20



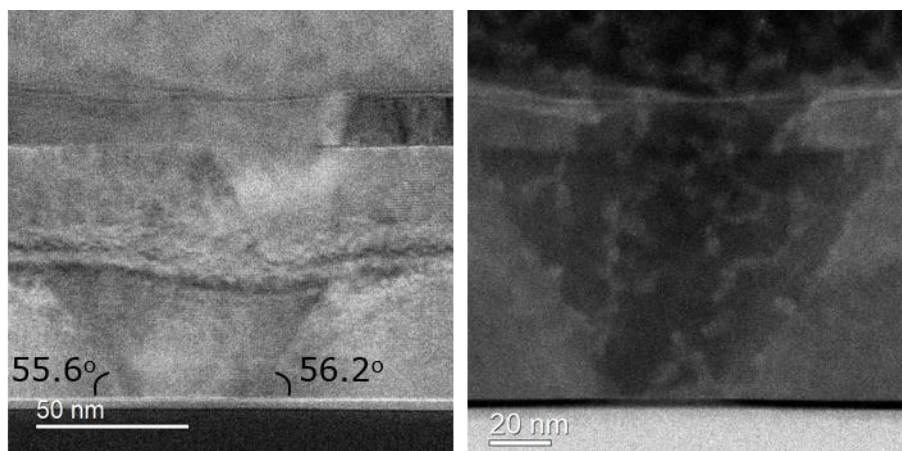
C6: Raw cross-sectional STEM images from figure 22



C7: Optical microscope images of the hBN/Gr/hBN stacking process. The two bottom images show the hBN/Gr/hBN stack in dark field mode (left) and bright field mode (right) and here the presence of bubbles is clearly seen as bright spots in both images.

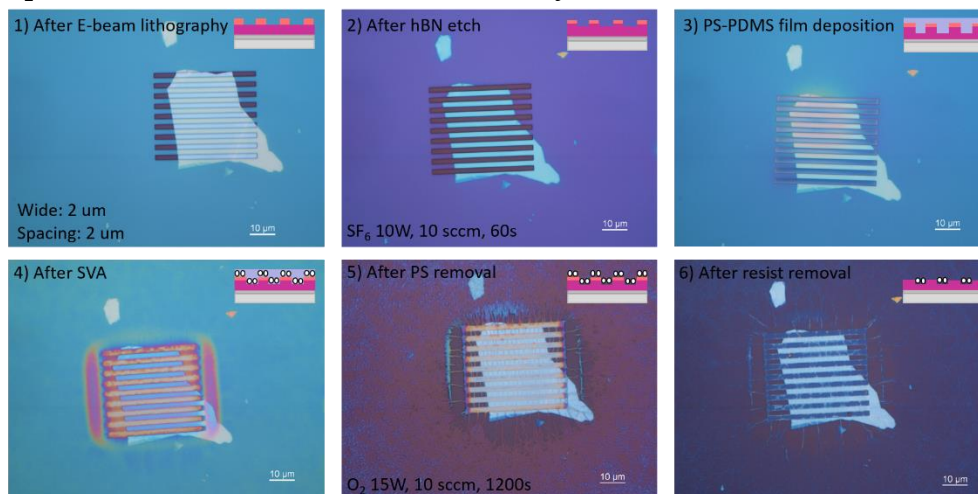


C8: BF (left) and HAADF (right) STEM images from a hBN/Gr/hBN stack showing etch angle around $55-56^\circ$ and the presense of a polymer layer (black layer in HAADF) beneath the bottom hBN flake. Additionally, the shift of the top hBN flake is also observed here.

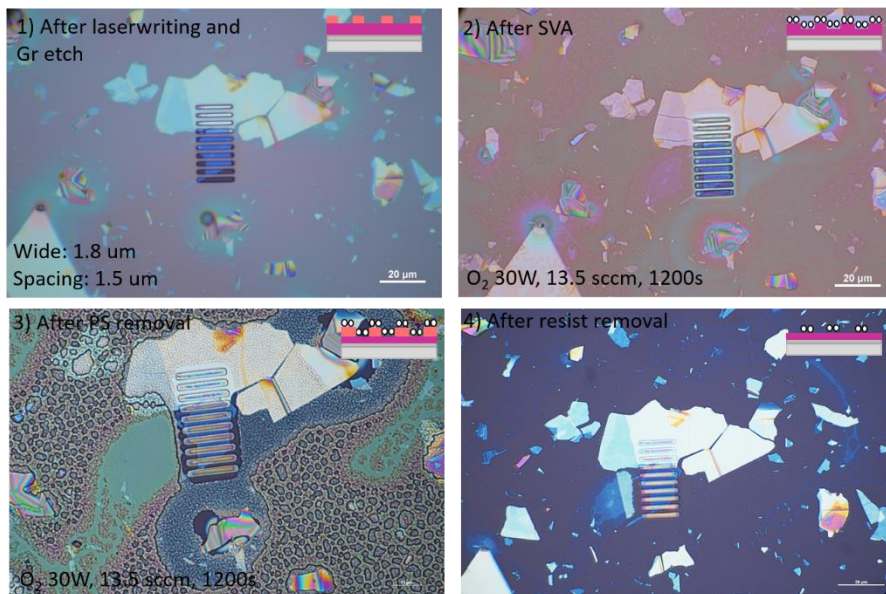


D. PDMS nanofluidic channel fabrication on 2D materials

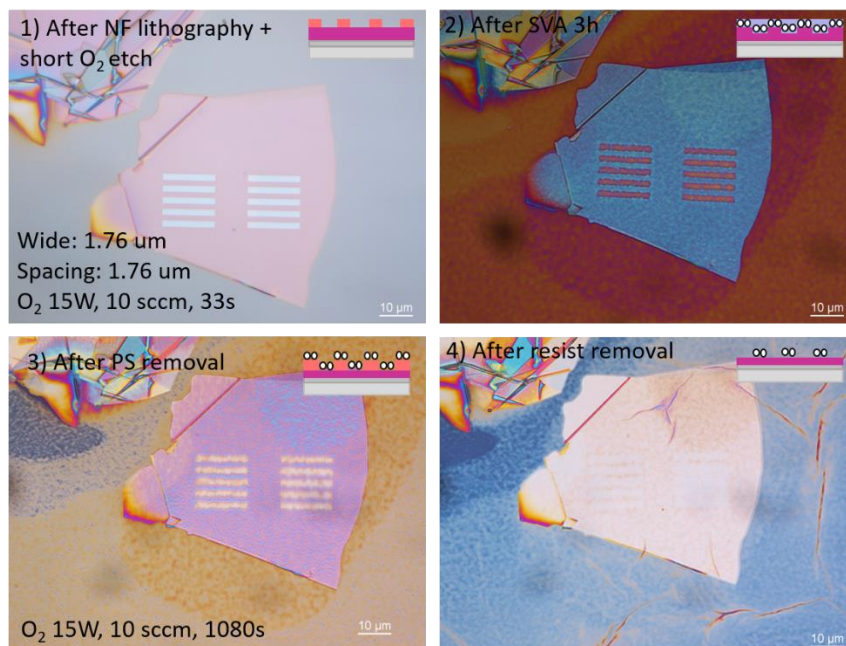
D1: DSA process, route 1, in trenches made by EBL.



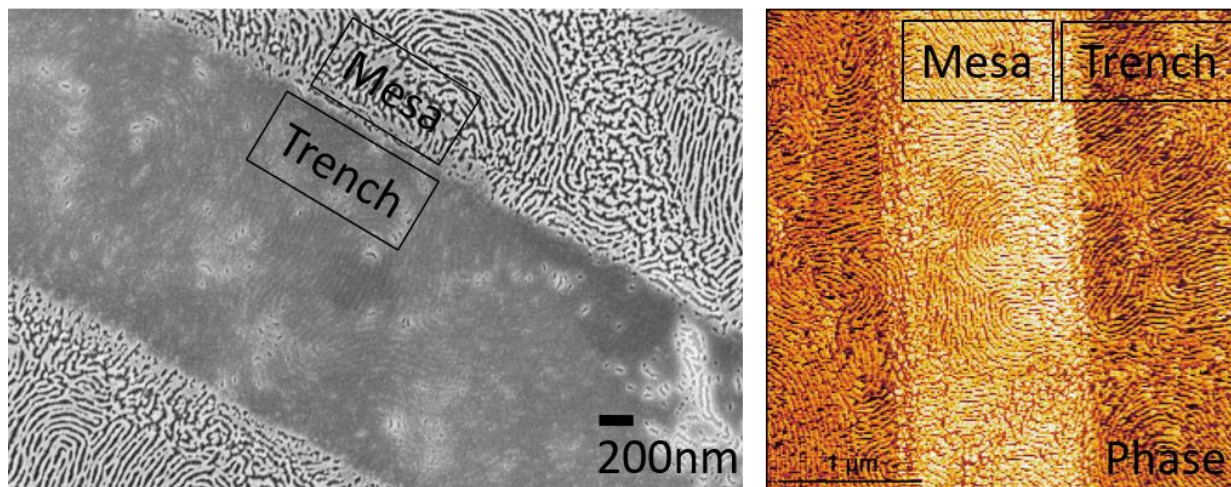
D2: DSA process, route 2, in trenches made by direct laser writing



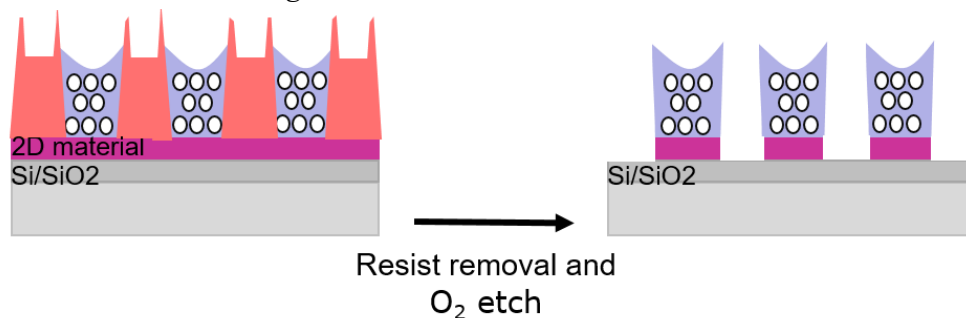
D3: DSA process, route 2, in trenches made by t-SPL



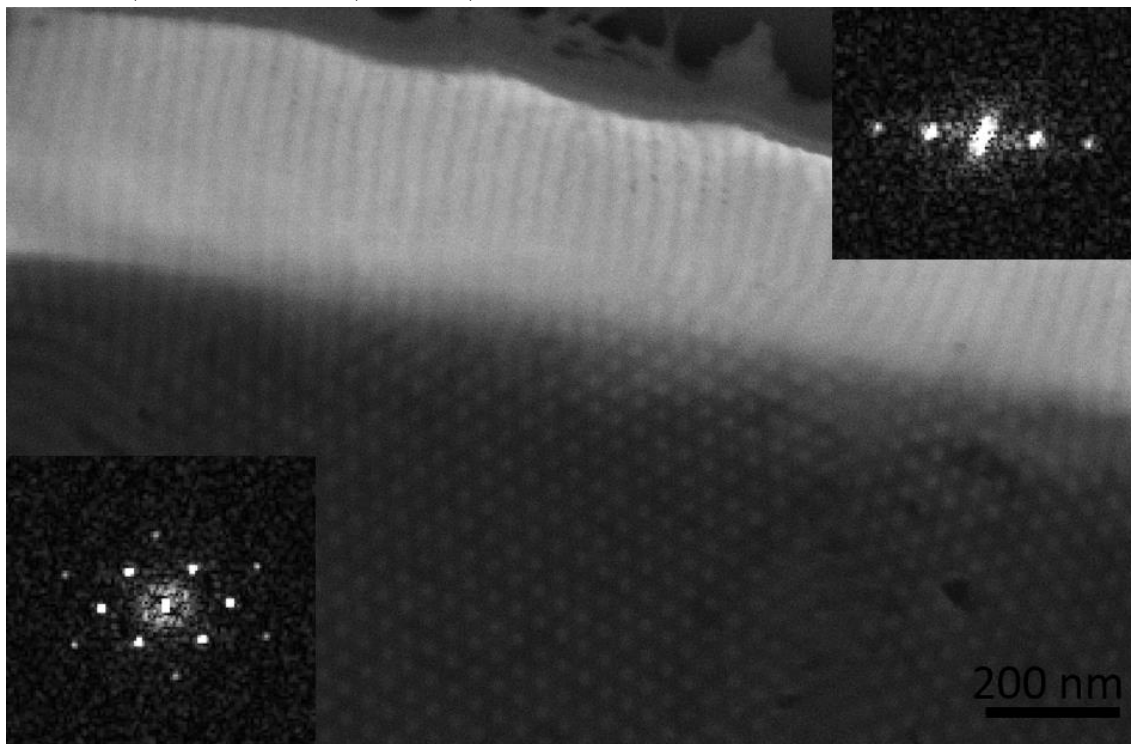
D4: SEM (left) and AFM phase image of graphene flake patterned with laser writer through route 1 with the resist removed right after step 1a. BCP microstructure is found in the trenches and on the mesas.



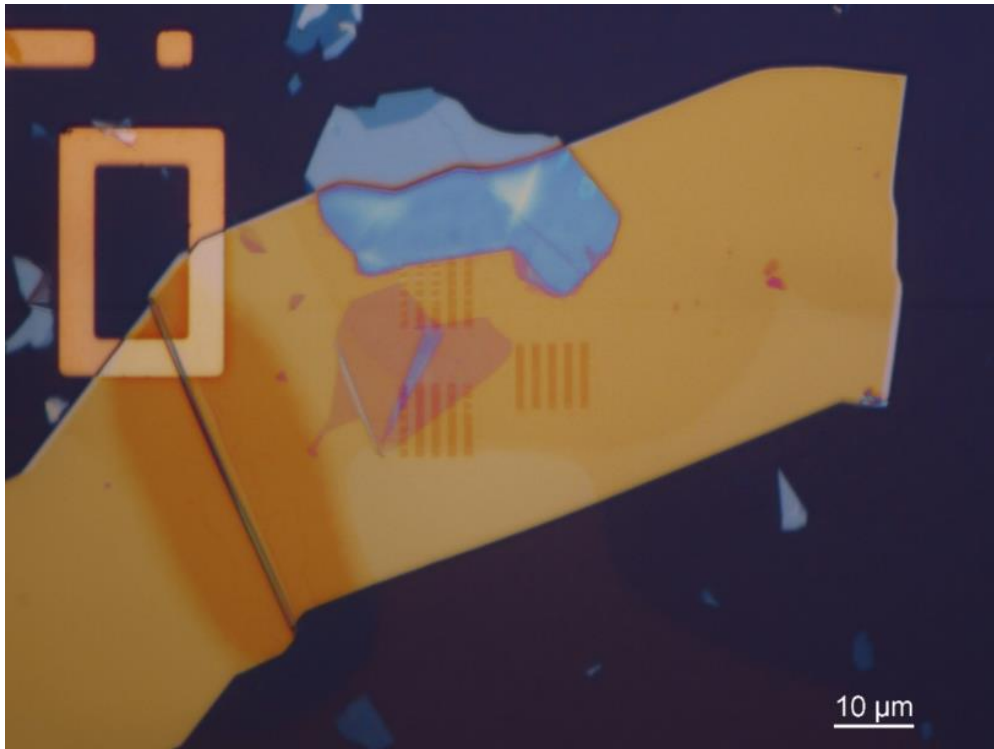
D5: A schematic showing the formation of a PS-*b*-PDMS multilayer in trenches deeper than the natural length of the BCP.



D6: hBN flake with trench pattern made from laser writing in S1805 resist. Inside the trench, the ordering of the ox-PDMS cylinders can be observed going from a horizontal alignment at the trench edges to a vertical alignment when moving towards the trench center. This could indicate a difference in the film thickness. The inset is the Fourier transform of each area showing the periods of 36.45 nm (horizontal) and 33.2 nm (vertical)



D7: Showing a bottom hBN flake patterned with t-SPL through route 1, with an hBN flake transferred on top of the trenches.



Bibliography

1. Ren, J., L. Stagi, and P. Innocenzi, *Hydroxylated boron nitride materials: from structures to functional applications*. Journal of Materials Science, 2021. **56**(6): p. 4053-4079.
2. Cochran, E.W., C.J. Garcia-Cervera, and G.H. Fredrickson, *Stability of the gyroid phase in diblock copolymers at strong segregation (vol 39, pg 2449, 2006)*. Macromolecules, 2006. **39**(12): p. 4264-4264.
3. Cooper, D.R., et al., *Experimental Review of Graphene*. 2012, Hindawi Limited: International Scholarly Research Notices. p. 56.
4. Bohme, S., et al., *Annealing treatments of cylindrical siloxane-based block copolymers optimized for nanomanufacturing*. Micro and Nano Engineering, 2018. **1**: p. 56-62.
5. Jeong, S.J., et al., *Ultralarge-Area Block Copolymer Lithography Enabled by Disposable Photoresist Prepatterning*. Acs Nano, 2010. **4**(9): p. 5181-5186.
6. O'Driscoll, B.M.D., et al., *Achieving structural control with thin polystyrene-b-polydimethylsiloxane block copolymer films: The complex relationship of interface chemistry, annealing methodology and process conditions*. European Polymer Journal, 2013. **49**(11): p. 3445-3454.
7. Castro Neto, A.H., et al., *The electronic properties of graphene*. Reviews of Modern Physics, 2009. **81**(1): p. 109-162.
8. Botiz, I. and S.B. Darling, *Optoelectronics using block copolymers*. Materials Today, 2010. **13**(5): p. 42-51.
9. Jessen, B.S., et al., *Lithographic band structure engineering of graphene*. Nature Nanotechnology, 2019. **14**(4): p. 340-346.
10. Gotrik, K.W., et al., *Morphology Control in Block Copolymer Films Using Mixed Solvent Vapors*. Acs Nano, 2012. **6**(9): p. 8052-8059.
11. Zhou, C., et al., *Fabrication of Nanoporous Alumina Ultrafiltration Membrane with Tunable Pore Size Using Block Copolymer Templates*. Advanced Functional Materials, 2017. **27**(34).
12. Huang, S.Q., et al., *Single-layer graphene membranes by crack-free transfer for gas mixture separation*. Nature Communications, 2018. **9**.
13. Cummins, C., et al., *Enabling future nanomanufacturing through block copolymer self-assembly: A review*. Nano Today, 2020. **35**.
14. Xia, F., et al., *Graphene Field-Effect Transistors with High On/Off Current Ratio and Large Transport Band Gap at Room Temperature*. Nano Letters, 2010. **10**(2): p. 715-718.
15. Bai, J., et al., *Graphene nanomesh*. Nature Nanotechnology, 2010. **5**(3): p. 190-194.
16. Geim, A.K. and I.V. Grigorieva, *Van der Waals heterostructures*. Nature, 2013. **499**(7459): p. 419-425.
17. Heiranian, M., A.B. Farimani, and N.R. Aluru, *Water desalination with a single-layer MoS₂ nanopore*. Nature Communications, 2015. **6**(1): p. 1-6.

18. Zheng, Z., R. Gr unker, and X. Feng, *Synthetic Two-Dimensional Materials: A New Paradigm of Membranes for Ultimate Separation*. Advanced Materials, 2016. **28**(31): p. 6529-6545.
19. Suk, M.E. and N.R. Aluru, *Water Transport through Ultrathin Graphene*. The Journal of Physical Chemistry Letters, 2010. **1**(10): p. 1590-1594.
20. Nourbakhsh, A., et al., *MoS₂ Field-Effect Transistor with Sub-10 nm Channel Length*. Nano Letters, 2016. **16**(12): p. 7798-7806.
21. Fang, T., et al., *Mobility in semiconducting graphene nanoribbons: Phonon, impurity, and edge roughness scattering*. Physical Review B, 2008. **78**(20).
22. Dean, C.R., et al., *Boron nitride substrates for high-quality graphene electronics*. Nature Nanotechnology, 2010. **5**(10): p. 722-726.
23. Lang, C., M. Kumar, and R.J. Hickey, *Current status and future directions of self-assembled block copolymer membranes for molecular separations*. Soft Matter, 2021. **17**(46): p. 10405-10415.
24. Stanford, M.G., P.D. Rack, and D. Jariwala, *Emerging nanofabrication and quantum confinement techniques for 2D materials beyond graphene*. npj 2D Materials and Applications, 2018. **2**(20): p. 1-15.
25. Park, H., et al., *Nano-patterning on multilayer MoS₂ via block copolymer lithography for highly sensitive and responsive phototransistors*. Communications Materials, 2021. **2**(1).
26. Bates, C.M. and F.S. Bates, *50th Anniversary Perspective: Block Polymers—Pure Potential*. Macromolecules, 2016. **50**(1): p. 3-22.
27. Morris, M.A., *Directed self-assembly of block copolymers for nanocircuitry fabrication*. Microelectronic Engineering, 2015. **132**: p. 207-217.
28. Yun, T., et al., *2D Metal Chalcogenide Nanopatterns by Block Copolymer Lithography*. Advanced Functional Materials, 2018. **28**(50).
29. Cagliani, A., et al., *Large-area nanopatterned graphene for ultrasensitive gas sensing*. Nano Research, 2014. **7**(5): p. 743-754.
30. Park, W.I., et al., *Self-Assembly-Induced Formation of High-Density Silicon Oxide Memristor Nanostructures on Graphene and Metal Electrodes*. Nano Letters, 2012. **12**(3): p. 1235-1240.
31. Ninago, M.D., et al., *Synthesis and Morphology of Model PS-*b*-PDMS Copolymers*. Journal of Polymer Science Part a-Polymer Chemistry, 2010. **48**(14): p. 3119-3127.
32. Bates, F.S., et al., *Multiblock Polymers: Panacea or Pandora's Box?* Science, 2012. **336**(6080): p. 434-440.
33. Tseng, Y.-C. and S.B. Darling, *Block Copolymer Nanostructures for Technology*. Polymers, 2010. **2**(4): p. 470-489.
34. Matsen, M.W. and F.S. Bates, *Unifying weak- and strong-segregation block copolymer theories*. Macromolecules, 1996. **29**(4): p. 1091-1098.
35. Bates, C.M., et al., *Block Copolymer Lithography*. Macromolecules, 2014. **47**(1): p. 2-12.

-
36. Suh, H.S., et al., *Thickness Dependence of Neutral Parameter Windows for Perpendicularly Oriented Block Copolymer Thin Films*. *Macromolecules*, 2010. **43**(10): p. 4744-4751.
 37. Knoll, A., et al., *Phase behavior in thin films of cylinder-forming block copolymers*. *Physical Review Letters*, 2002. **89**(3).
 38. Aissou, K., M. Kogelschatz, and T. Baron, *Self-assembling study of a cylinder-forming block copolymer via a nucleation-growth mechanism*. *Nanotechnology*, 2009. **20**(9).
 39. Jung, Y.S. and C.A. Ross, *Orientation-Controlled Self-Assembled Nanolithography Using a Polystyrene-Polydimethylsiloxane Block Copolymer*. *Nano Letters*, 2007. **7**(7): p. 2046-2050.
 40. Andersen, T.H., et al., *Surface morphology of PS-PDMS diblock copolymer films*. *Journal of Electron Spectroscopy and Related Phenomena*, 2001. **121**(1-3): p. 93-110.
 41. Li, T., et al., *Substrate tolerant direct block copolymer nanolithography*. *Nanoscale*, 2016. **8**(1): p. 136-140.
 42. Borah, D., et al., *Orientation and Alignment Control of Microphase-Separated PS-*b*-PDMS Substrate Patterns via Polymer Brush Chemistry*. *Acs Applied Materials & Interfaces*, 2013. **5**(1): p. 88-97.
 43. Bates, C.M., et al., *Polarity-Switching Top Coats Enable Orientation of Sub-10-nm Block Copolymer Domains*. *Science*, 2012. **338**(6108): p. 775-779.
 44. Kim, E., et al., *A Top Coat with Solvent Annealing Enables Perpendicular Orientation of Sub-10 nm Microdomains in Si-Containing Block Copolymer Thin Films*. *Advanced Functional Materials*, 2014. **24**(44): p. 6981-6988.
 45. Sinturel, C., et al., *Solvent Vapor Annealing of Block Polymer Thin Films*. *Macromolecules*, 2013. **46**(14): p. 5399-5415.
 46. Dinachali, S.S., et al., *Thermo-Solvent Annealing of Polystyrene-Polydimethylsiloxane Block Copolymer Thin Films*. *Acs Macro Letters*, 2015. **4**(5): p. 500-504.
 47. Jung, Y.S. and C.A. Ross, *Solvent-Vapor-Induced Tunability of Self-Assembled Block Copolymer Patterns*. *Advanced Materials*, 2009. **21**(24): p. 2540-+.
 48. Bai, W., K.G. Yager, and C.A. Ross, *In Situ Characterization of the Self-Assembly of a Polystyrene-Polydimethylsiloxane Block Copolymer during Solvent Vapor Annealing*. *Macromolecules*, 2015. **48**(23): p. 8574-8584.
 49. Rasappa, S., et al., *Morphology evolution of PS-*b*-PDMS block copolymer and its hierarchical directed self-assembly on block copolymer templates*. *Microelectronic Engineering*, 2018. **192**: p. 1-7.
 50. Jeong, J.W., et al., *Highly Tunable Self-Assembled Nanostructures from a Poly(2-vinylpyridine-*b*-dimethylsiloxane) Block Copolymer*. *Nano Letters*, 2011. **11**(10): p. 4095-4101.
 51. Jeon, H.U., et al., *Electric field directed self-assembly of block copolymers for rapid formation of large-area complex nanopatterns*. *Molecular Systems Design & Engineering*, 2017. **2**(5): p. 560-566.

-
52. Jin, H.M., et al., *Laser Writing Block Copolymer Self-Assembly on Graphene Light-Absorbing Layer*. *Acs Nano*, 2016. **10**(3): p. 3435-3442.
 53. Novoselov, K.S., et al., *Electric field effect in atomically thin carbon films*. *Science*, 2004. **306**(5696): p. 666-669.
 54. Novoselov, K.S., et al., *Two-dimensional atomic crystals*. *Proceedings of the National Academy of Sciences of the United States of America*, 2005. **102**(30): p. 10451-10453.
 55. Son, J.G., et al., *Sub-10 nm Graphene Nanoribbon Array Field-Effect Transistors Fabricated by Block Copolymer Lithography*. *Advanced Materials*, 2013. **25**(34): p. 4723-4728.
 56. Wang, Z., et al., *Experimental demonstration of graphene plasmons working close to the near-infrared window*. *Optics Letters*, 2016. **41**(22): p. 5345-5348.
 57. Moghadam, F. and H.B. Park, *2D nanoporous materials: membrane platform for gas and liquid separations*. *2D Materials*, 2019. **6**(4): p. 1-33.
 58. Lee, J., et al., *Uniform Graphene Quantum Dots Patterned from Self-Assembled Silica Nanodots*. *Nano Letters*, 2012. **12**(12): p. 6078-6083.
 59. Liang, X., et al., *Formation of Bandgap and Subbands in Graphene Nanomeshes with Sub-10 nm Ribbon Width Fabricated via Nanoimprint Lithography*, *Nano Letters*, 2010. **10**(7): p. 2454-2460.
 60. Lee, C., et al., *Measurement of the elastic properties and intrinsic strength of monolayer graphene*. *Science*, 2008. **321**(5887): p. 385-388.
 61. Mayorov, A.S., et al., *Micrometer-Scale Ballistic Transport in Encapsulated Graphene at Room Temperature*. *Nano Letters*, 2011. **11**(6): p. 2396-2399.
 62. Balandin, A.A., *Thermal properties of graphene and nanostructured carbon materials*. *Nature Materials*, 2011. **10**(8): p. 569-581.
 63. Bunch, J.S., et al., *Impermeable atomic membranes from graphene sheets*. *Nano Letters*, 2008. **8**(8): p. 2458-2462.
 64. Novoselov, K.S., et al., *A roadmap for graphene*. *Nature*, 2012. **490**(7419): p. 192-200.
 65. Dean, C.R., et al., *Hofstadter's butterfly and the fractal quantum Hall effect in moiré superlattices*. *Nature*, 2013. **497**(7451): p. 598-602.
 66. Hunt, B., et al., *Massive Dirac Fermions and Hofstadter Butterfly in a van der Waals Heterostructure*. *Science*, 2013. **340**(6139): p. 1427-1430.
 67. Kim, M., et al., *Fabrication and Characterization of Large-Area, Semiconducting Nanoperforated Graphene Materials*. *Nano Letters*, 2010. **10**(4): p. 1125-1131.
 68. Mackenzie, D.M.A., et al., *Graphene antidot lattice transport measurements*. *International Journal of Nanotechnology*, 2017. **14**(1-6): p. 226-234.
 69. Han, M.Y., et al., *Energy Band-Gap Engineering of Graphene Nanoribbons*. *Physical Review Letters*, 2007. **98**(20).
 70. Chen, J.H., et al., *Intrinsic and extrinsic performance limits of graphene devices on SiO₂*. *Nature Nanotechnology*, 2008. **3**(4): p. 206-209.

-
71. Watanabe, K., T. Taniguchi, and H. Kanda, *Direct-bandgap properties and evidence for ultraviolet lasing of hexagonal boron nitride single crystal*. Nature Materials, 2004. **3**(6): p. 404-409.
 72. Zhou, H.Q., et al., *High thermal conductivity of suspended few-layer hexagonal boron nitride sheets*. Nano Research, 2014. **7**(8): p. 1232-1240.
 73. Falin, A., et al., *Mechanical properties of atomically thin boron nitride and the role of interlayer interactions*. Nature Communications, 2017. **8**.
 74. Fukamachi, S., et al., *Large-area synthesis and transfer of multilayer hexagonal boron nitride for enhanced graphene device arrays*. Nature Electronics, 2023. **6**(2): p. 126-+.
 75. Zhang, Y., et al., *Hexagonal Boron Nitride with Designed Nanopores as a High-Efficiency Membrane for Separating Gaseous Hydrogen from Methane*. The Journal of Physical Chemistry C, 2015. **119**(34): p. 19826-19831.
 76. Liu, L., et al., *Hexagonal boron nitride with nanoslits as a membrane for water desalination: A molecular dynamics investigation*. Separation and Purification Technology, 2020. **251**.
 77. Wang, X.T., et al., *Effects of solvents and polymer on photoluminescence of transferred WS₂ monolayers*. Journal of Vacuum Science & Technology B, 2019. **37**(5).
 78. Gammelgaard, L., *PhD thesis -2D Material Device Architectures: Process Optimisation and Characterisation*. Technical University of Denmark, 2016: <https://orbit.dtu.dk/en/publications/2d-material-device-architectures-process-optimisation-and-charact>.
 79. Withers, F., et al., *Light-emitting diodes by band-structure engineering in van der Waals heterostructures*. Nature Materials, 2015. **14**(3): p. 301-306.
 80. Pizzocchero, F., et al., *The hot pick-up technique for batch assembly of van der Waals heterostructures*. Nature Communications, 2016. **7**(1): p. 1-10.
 81. Sandner, A., et al., *Ballistic Transport in Graphene Antidot Lattices*. Nano Letters, 2015. **15**(12): p. 8402-8406.
 82. Phillip, W.A., et al., *Self-Assembled Block Copolymer Thin Films as Water Filtration Membranes*. Acs Applied Materials & Interfaces, 2010. **2**(3): p. 847-853.
 83. Jung, Y.S., et al., *Nanowire Conductive Polymer Gas Sensor Patterned Using Self-Assembled Block Copolymer Lithography*. Nano Letters, 2008. **8**(11): p. 3776-3780.
 84. Huang, L.L., et al., *Catalyst design by scanning probe block copolymer lithography*. Proceedings of the National Academy of Sciences of the United States of America, 2018. **115**(15): p. 3764-3769.
 85. Kim, J.Y., et al., *3D Tailored Crumpling of Block-Copolymer Lithography on Chemically Modified Graphene*. Advanced Materials, 2016. **28**(8): p. 1591-1596.
 86. Yang, G.G., et al., *Block Copolymer Nanopatterning for Nonsemiconductor Device Applications*. Acs Applied Materials & Interfaces, 2022. **14**(10): p. 12011-12037.

-
87. Hu, X.-H. and S. Xiong, *Fabrication of Nanodevices Through Block Copolymer Self-Assembly*. 2022, Front. Nanotechnol.
 88. Gu, X., I. Gunkel, and T.P. Russell, *Pattern transfer using block copolymers*. Philos. Trans. R. Soc. A: Mathematical, Physical and Engineering Sciences, 2013. **371**(2000): p. 20120306.
 89. Chang, T.H., et al., *Directed self-assembly of block copolymer films on atomically-thin graphene chemical patterns*. Scientific Reports, 2016. **6**.
 90. Rasappa, S., et al., *High quality sub-10 nm graphene nanoribbons by on-chip PS-b-PDMS block copolymer lithography*. 2015.
 91. Rasappa, S., et al., *Directed self-assembly of a high-chi block copolymer for the fabrication of optical nanoresonators*. Nanoscale, 2018. **10**(38): p. 18306-18314.
 92. Jeong, S.J., et al., *Soft Graphoepitaxy of Block Copolymer Assembly with Disposable Photoresist Confinement*. Nano Letters, 2009. **9**(6): p. 2300-2305.
 93. Cheng, J.Y., et al., *Templated self-assembly of block copolymers: Top-down helps bottom-up*. Advanced Materials, 2006. **18**(19): p. 2505-2521.
 94. Chu, J.H., et al., *MORPHOLOGIES OF STRONGLY SEGREGATED POLYSTYRENE-POLY(DIMETHYLSILOXANE) DIBLOCK COPOLYMERS*. Polymer, 1995. **36**(8): p. 1569-1575.
 95. Ndoni, S., et al., *Lubricating effect of thin films of styrene-dimethylsiloxane block copolymers*. Langmuir, 1999. **15**(11): p. 3859-3865.
 96. Saam, J.C., D.J. Gordon, and S. Lindsey, *BLOCK COPOLYMERS OF POLYDIMETHYLSILOXANE AND POLYSTYRENE*. Macromolecules, 1970. **3**(1): p. 1-&.
 97. Ninago, M.D., et al., *Controlled Synthesis of Poly(dimethylsiloxane) Homopolymers Using High-Vacuum Anionic Polymerization Techniques*. Journal of Polymer Science Part a-Polymer Chemistry, 2009. **47**(18): p. 4774-4783.
 98. Rasappa, S., et al., *High molecular weight block copolymer lithography for nanofabrication of hard mask and photonic nanostructures*. Journal of Colloid and Interface Science, 2019. **534**: p. 420-429.
 99. Cagliani, A., et al., *Defect/oxygen assisted direct write technique for nanopatterning graphene*. Nanoscale, 2015. **7**(14): p. 6271-6277.
 100. Arias-Zapata, J., et al., *Engineering Self-Assembly of a High-chi Block Copolymer for Large-Area Fabrication of Transistors Based on Functional Graphene Nanoribbon Arrays*. Chemistry of Materials, 2019. **31**(9): p. 3154-3162.
 101. Zhou, J., et al., *Self-Aligned Assembly of a Poly(2-vinylpyridine)-b-Polystyrene-b-Poly(2-vinylpyridine) Triblock Copolymer on Graphene Nanoribbons*. Acs Applied Materials & Interfaces, 2021. **13**(34): p. 41190-41199.
 102. Jiao, L.Y., L.M. Xie, and H.J. Dai, *Densely aligned graphene nanoribbons at similar to 35 nm pitch*. Nano Research, 2012. **5**(4): p. 292-296.
 103. Arias-Zapata, J., et al., *Effective patterning and cleaning of graphene by plasma etching and block copolymer lithography for nanoribbon fabrication*. Journal of Vacuum Science & Technology A, 2018. **36**(5).

-
104. Jacobberger, R.M., et al., *Boundary-directed epitaxy of block copolymers*. Nature Communications, 2020. **11**(1).
 105. Lin, X.B., et al., *Heterogeneous MXene/PS-b-P2VP Nanofluidic Membranes with Controllable Ion Transport for Osmotic Energy Conversion*. Advanced Functional Materials, 2021. **31**(45).
 106. Tian, H., et al., *General Interfacial Self-Assembly Engineering for Patterning Two-Dimensional Polymers with Cylindrical Mesopores on Graphene*. Angewandte Chemie-International Edition, 2019. **58**(30): p. 10173-10178.
 107. Hadjichristidis, N., et al., *Anionic polymerization: High vacuum techniques*. Journal of Polymer Science Part a-Polymer Chemistry, 2000. **38**(18): p. 3211-3234.
 108. Lee, W., et al., *Molecular weight distribution of polystyrene made by anionic polymerization*. Macromolecules, 2000. **33**(14): p. 5111-5115.
 109. Worsfold, D.J. and S. Bywater, *ANIONIC POLYMERIZATION OF STYRENE*. Canadian Journal of Chemistry-Revue Canadienne De Chimie, 1960. **38**(10): p. 1891-1900.
 110. Hsieh, H.L., *KINETICS OF POLYMERIZATION OF BUTADIENE ISOPRENE AND STYRENE WITH ALKYL LITHIUMS .I. RATE OF POLYMERIZATION*. Journal of Polymer Science Part a-General Papers, 1965. **3**(1PA): p. 153-&.
 111. Hammouch, S.O., et al., *SYNTHESIS AND CHARACTERIZATION OF MONOFUNCTIONAL POLYDIMETHYLSILOXANES WITH A NARROW MOLECULAR-WEIGHT DISTRIBUTION*. Polymer, 1995. **36**(2): p. 421-426.
 112. Frye, C.L., et al., *REACTIONS OF ORGANOLITHIUM REAGENTS WITH SILOXANE SUBSTRATES*. Journal of Organic Chemistry, 1970. **35**(5): p. 1308-&.
 113. Maschke, U. and T. Wagner, *Synthesis of high-molecular-weight poly(dimethylsiloxane) of uniform size by anionic polymerization, 1. Initiation by a monofunctional lithium siloxanolate*. Die Makromolekulare Chemie, 1992. **193**: p. 2453-2466.
 114. Zilliox, J.G., J.E.L. Roovers, and S. Bywater, *PREPARATION AND PROPERTIES OF POLYDIMETHYLSILOXANE AND ITS BLOCK COPOLYMERS WITH STYRENE*. Macromolecules, 1975. **8**(5): p. 573-578.
 115. Zundel, T., et al., *TRIMETHYLSILYLMETHYLLITHIUM - A NOVEL INITIATOR FOR THE ANIONIC-POLYMERIZATION OF CYCLOSILOXANES AND VINYL MONOMERS*. Macromolecular Symposia, 1994. **88**: p. 177-189.
 116. Elkins, C.L. and T.E. Long, *Living anionic polymerization of hexamethylcyclotrisiloxane (D-3) using functionalized initiation*. Macromolecules, 2004. **37**(17): p. 6657-6659.
 117. Fessler, W.A. and P.C. Juliano, *REACTIVITY OF SOLVATED LITHIUM N-BUTYLDIMETHYLSILANOLATE WITH ORGANOSILOXANE SUBSTRATES*. Industrial & Engineering Chemistry Product Research and Development, 1972. **11**(4): p. 407-&.

-
118. Georgopoulos, P., et al., *Synthesis, molecular characterization and self-assembly of (PS-*b*-PDMS)(*n*) type linear (*n*=1, 2) and star (*n*=3, 4) block copolymers*. Polymer Chemistry, 2017. **8**(5): p. 843-850.
 119. Bellas, V., H. Iatrou, and N. Hadjichristidis, *Controlled anionic polymerization of hexamethylcyclotrisiloxane. Model linear and miktoarm star co- and terpolymers of dimethylsiloxane with styrene and isoprene*. Macromolecules, 2000. **33**(19): p. 6993-6997.
 120. Higginbotham, J.U.I.a.C.L., *Polymer Molecular Weight Analysis by ¹H NMR Spectroscopy*. 2011. **88**(8): p. 1098-1104.
 121. Umoren, S.A. and M.M. Solomon, *Polymer Characterization : Polymer Molecular Weight Determination*. 2016: p. 412-419.
 122. Morgan, A.M., S.K. Pollack, and K. Beshah, *Synthesis and multidimensional NMR characterization of PDMS-*b*-PS prepared by combined anionic ring-opening and nitroxide-mediated radical polymerization*. Macromolecules, 2002. **35**(11): p. 4238-4246.
 123. Malhotra, S.L., T.L. Bluhm, and Y. Deslandes, *SYNTHESIS AND CHARACTERIZATION OF STYRENE-B-DIMETHYLSILOXANE DIBLOCK AND STYRENE-B-ISOPRENE-B-DIMETHYLSILOXANE TRIBLOCK COPOLYMERS*. European Polymer Journal, 1986. **22**(5): p. 391-397.
 124. Williams, E.A. and J.D. Cargioli, *Silicon-29 NMR Spectroscopy*. 1979, Annual Reports on NMR Spectroscopy: Elsevier.
 125. Chai, M.H., P.L. Rinaldi, and S.L. Hu, *H-1/C-13/Si-29 triple resonance 3D NMR study of poly(dimethylsiloxane) MD3MH*. Nmr Spectroscopy of Polymers in Solution and in the Solid State, 2003. **834**: p. 137-146.
 126. I. Ando, M.K., M. Kanekiyo, S. Kuroki, S. Ando, S. Matsukawa, H. Kurosu, H. Yasunaga, S. Amiya, *Experimental Methods in Polymer Science, Chapter 4*. 2000, Academic Press; 1st edition.
 127. Fleming, I. and D. Williams, *Spectroscopic Methods in Organic Chemistry*. 2007, McGraw-Hill Education. p. 304.
 128. Kupce, E. and R. Freeman, *Fast multidimensional NMR by polarization sharing*. Magnetic Resonance in Chemistry, 2007. **45**(1): p. 2-4.
 129. Ndoni, S., et al., *LABORATORY-SCALE SETUP FOR ANIONIC-POLYMERIZATION UNDER INERT ATMOSPHERE*. Review of Scientific Instruments, 1995. **66**(2): p. 1090-1095.
 130. Cazes, J., *GEL PERMEATION CHROMATOGRAPHY .2*. Journal of Chemical Education, 1966. **43**(8): p. A625-&.
 131. Quirk, R.P. and W.C. Chen, *FUNCTIONALIZATION OF POLYMERIC ORGANO-LITHIUM COMPOUNDS - OXIDATION*. Journal of Polymer Science Part a-Polymer Chemistry, 1984. **22**(11): p. 2993-3000.
 132. Park, W.I., et al., *Self-Assembled Incorporation of Modulated Block Copolymer Nanostructures in Phase-Change Memory for Switching Power Reduction*. Acs Nano, 2013. **7**(3): p. 2651-2658.

-
133. Radamson, H.H., et al., *The Challenges of Advanced CMOS Process from 2D to 3D*. Applied Sciences-Basel, 2017. **7**(10).
 134. Jung, Y.S., et al., *A Path to Ultranarrow Patterns Using Self-Assembled Lithography*. Nano Letters, 2010. **10**(3): p. 1000-1005.
 135. Berger, C., et al., *Electronic confinement and coherence in patterned epitaxial graphene*. Science, 2006. **312**(5777): p. 1191-1196.
 136. Pettes, M.T., et al., *Influence of Polymeric Residue on the Thermal Conductivity of Suspended Bilayer Graphene*. Nano Letters, 2011. **11**(3): p. 1195-1200.
 137. Bang, K., et al., *Effect of ribbon width on electrical transport properties of graphene nanoribbons*. Nano Convergence, 2018. **5**.
 138. Kim, S.S., et al., *Large area tunable arrays of graphene nanodots fabricated using diblock copolymer micelles*. Nanotechnology, 2012. **23**(12).
 139. Hu, S., et al., *Proton transport through one-atom-thick crystals*. Nature, 2014. **516**(7530): p. 227-+.
 140. Chen, C., et al., *Functionalized boron nitride membranes with ultrafast solvent transport performance for molecular separation*. Nature Communications, 2018. **9**.
 141. Rubinstein, M. and R.H. Colby, *Polymer Physics*. Reprint ed. 2006, London: Oxford Univ. Press.
 142. West, P.E., *Introduction to Atomic Force Microscopy: Theory, Practice, Applications*. 2007, Santa Clara, CA: Pacific Nanotechnology. 159.
 143. Andersen, A.B., et al., *Limiting Damage to 2D Materials during Focused Ion Beam Processing*. Physica Status Solidi B-Basic Solid State Physics, 2020. **257**(12).
 144. Keerthi, A., et al., *Water friction in nanofluidic channels made from two-dimensional crystals*. Nature Communications, 2021. **12**(1).
 145. Wang, Q., P.F. Nealey, and J.J. de Pablo, *Monte Carlo simulations of asymmetric diblock copolymer thin films confined between two homogeneous surfaces*. Macromolecules, 2001. **34**(10): p. 3458-3470.
 146. Chan, C.-M. and E. Michele, *Polymer surface modification and characterization*. 1st ed. ed. 1994, Munich: Hanser publishers.
 147. Danielsen, D.R., et al., *Super-Resolution Nanolithography of Two-Dimensional Materials by Anisotropic Etching*. Acs Applied Materials & Interfaces, 2021. **13**(35): p. 41886-41894.
 148. Wheatley, D.E., *FLUIDICS-A NEW TECHNOLOGY*. Aircraft Engineering, 1967. **39**(8): p. 26-&.
 149. Eijkel, J.C.T. and A. van den Berg, *Nanofluidics: what is it and what can we expect from it?* Microfluidics and Nanofluidics, 2005. **1**(3): p. 249-267.
 150. Zhu, J.Y., et al., *The rapid emergence of two-dimensional nanomaterials for high-performance separation membranes*. Journal of Materials Chemistry A, 2018. **6**(9): p. 3773-3792.
 151. Cohen-Tanugi, D. and J.C. Grossman, *Water Desalination across Nanoporous Graphene*. Nano Letters, 2012. **12**(7): p. 3602-3608.

-
152. Radha, B., et al., *Molecular transport through capillaries made with atomic-scale precision*. Nature, 2016. **538**(7624): p. 222-+.
 153. Keerthi, A., et al., *Ballistic molecular transport through two-dimensional channels*. Nature, 2018. **558**(7710): p. 420-+.
 154. Tan, S.H., et al., *Oxygen plasma treatment for reducing hydrophobicity of a sealed polydimethylsiloxane microchannel*. Biomicrofluidics, 2010. **4**(3).
 155. Plecis, A. and Y. Chen, *Improved glass-PDMS-glass device technology for accurate measurements of electro-osmotic mobilities*. Microelectronic Engineering, 2008. **85**(5-6): p. 1334-1336.
 156. Bao, W.Z., et al., *Controlled ripple texturing of suspended graphene and ultrathin graphite membranes*. Nature Nanotechnology, 2009. **4**(9): p. 562-566.
 157. Gottlieb, S., et al., *Thermal scanning probe lithography for the directed self-assembly of block copolymers (vol 28, 175301, 2017)*. Nanotechnology, 2017. **28**(28).
 158. Sundrani, D., S.B. Darling, and S.J. Sibener, *Hierarchical assembly and compliance of aligned nanoscale polymer cylinders in confinement*. Langmuir, 2004. **20**(12): p. 5091-5099.
 159. Harasaki, A. and J.C. Wyant, *Fringe modulation skewing effect in white-light vertical scanning interferometry*. Applied Optics, 2000. **39**(13): p. 2101-2106.

E. Manuscript

“Nano-patterning of hBN via block-copolymer self-assembly of PS-PDMS”

*Christina. Breth Nielsen, Anton Lyksborg-Andersen, Xiang Cheng, Tim Booth and
Kristoffer Almdal*

(To be submitted)

Nano-patterning of hBN via block-copolymer self-assembly of PS-PDMS

Christina Breth Nielsen, Anton Lyksborg-Andersen, Xiang Cheng, Timothy J. Booth, Kristoffer Almdal

Cite: C. Breth Nielsen(a,c), Anton Lyksborg-Andersen(b), X. Cheng(b), Tim Booth(b,c), Kristoffer Almdal(a,c)

- a) Department of Chemistry, Technical University of Denmark, DK-2800 Kgs. Lyngby, Denmark
- b) Department of Physics, Technical University of Denmark, DK-2800 Kgs. Lyngby, Denmark
- c) Center for Nanostructured Graphene (CNG), Technical University of Denmark, DK-2800 Kgs. Lyngby, Denmark

Abstract

Nano-structuring of 2D materials is key to tuning their properties, for example introducing a bandgap in graphene via a nanomesh or antidot lattice. This requires high-quality periodic patterns with nanoscale resolution over large areas. Most conventional nano-structuring techniques for 2D materials are difficult to scale. Block copolymer (BCP) lithography can offer a scalable solution, but few studies show this lithography applied to 2D materials beyond graphene. Different surface interactions on various 2D materials can have a determining role in BCP microphase segregation. Here we report the nano-patterning of mechanically exfoliated hBN flakes through the BCP lithography process using polystyrene-polydimethylsiloxane, PS-PDMS. A monolayer of PDMS cylinders in a PS matrix is produced on the surface of multilayer hBN with no PDMS wetting layer. After an O₂ plasma etch, the PDMS is formed into hard silicon oxycarbide cylinders and subsequently can be used as a hard mask to transfer the patterns into hBN flakes using an SF₆ plasma. A clean nano-patterned hBN surface results from the plasma etching and additional furnace annealing during the BCP lithography process.

Introduction

For many of today's technologies, such as data storage [2, 3], integrated circuits [4-8] and membranes [9-11], lithographic structuring is an essential step in the device fabrication process. As devices have become smaller, specialized nanopatterning methods, such as electron beam-, ion beam- and deep UV lithography have risen. Most of these methods are limited by cost and lack of efficient upscaling [12-14]. However, block copolymer (BCP) lithography has shown very promising results in terms of low cost, scalability, and efficiency in obtaining feature sizes from 100 nm to below 10 nm [5, 15, 16].

BCP lithography typically uses thin films of BCP solutions to open a range of patterning morphologies driven by the thermodynamics of the BCP self-assembly mechanism. The key factors regarding BCP self-assembly in thin films are the block characteristics, substrate chemistry, interface interaction, and film thickness [11]. The interaction between the blocks is described by the Flory-Huggins parameter (χ) which together with the degree of polymerization (N) governs the pattern feature size. Recent BCP lithography studies have been focused on e.g. polystyrene-*b*-polydimethylsiloxane (PS-PDMS) which not only has a high χ -parameter but also shows good etch contrast between its constituent blocks [4, 7, 15, 17-20].

Patterning lattices of antidots (holes) in 2D materials has been shown to be a viable route towards controllably introducing a tailored bandgap [21, 22]. BCP lithography has previously been applied to

perform such nanopatterning on graphene and MoS₂ [3-5, 7, 8, 15, 23, 24]. However, despite the huge potential of BCP lithography for nano-patterning of 2D materials, it has not expanded to other 2D compounds.

A common problem when doing BCP lithography on 2D materials is the existence of polymer residues on the 2D material after the nano-patterning process. The presence of these has shown to impact the electronic properties e.g. by introducing p-doping of graphene resulting in decreased device performance [15, 23-25]. These residues often come from the use of polymer brushes or random BCPs used on graphene or MoS₂, to functionalize their surfaces before the BCP lithography process [3, 4, 24]. The brush layers help to obtain long-range order and to control the morphology orientation. However it also adds additional steps to the BCP process which is not desirable when considering manufacturing [7, 24].

Besides the ordering, the brushes also decreases the possibility of dewetting and hence wetting layers at the top/bottom interfaces, which are often seen for BCPs with large surface energy differences such as PS-PDMS. The formation of wetting layers in the PS-PDMS system has been investigated towards different surfaces, including chemical vapor deposition (CVD) graphene, usually based on its water contact angle. The studies report the formation of wetting layers at the substrate/BCP and BCP/air interfaces [7, 18, 26]. We note that studies on the wetting of PS-PDMS towards mechanically exfoliated graphene are limited, although this remains the best way to obtain high-quality graphene [24, 25].

Problems regarding the conservation of the intrinsic properties arise when nano-structuring 2D materials, due to bad pattern quality, in the form of dangling bonds, edge- and line roughness, polymer residues, etc. [27, 28]. Previous studies have shown that encapsulation of 2D materials can limit these problems and thereby maintain the wanted properties of pristine graphene. A good example is the van der Waals (vdW) heterostructure of hBN-encapsulated graphene [4, 6, 24, 29, 30]. hBN is an insulator that is structurally isomorphic to graphene and is a good candidate material for future separation technologies [31, 32]. It has been shown that graphene, sandwiched between two hBN flakes, can be nano-patterned with e-beam lithography and afterward show the opening of a tunable band gap and persistent physical properties compared to pristine graphene [22]. However, to mimic this with a BCP lithography process, we first need to know how the use of hBN affects the BCP lithography process. This will include the effects arising from the difference in surface energy and the use of exfoliated flakes. To the best of our knowledge, BCP lithography has never been studied on heterostructures or hBN.

In this paper, we aim to investigate the BCP lithography process on mechanically exfoliated hBN flakes using cylindrical forming PS-PDMS. Through cross-sectional scanning transmission electron microscopy (STEM) and atomic force microscopy (AFM), we study the cylindrical morphology and orientation together with the interactions at the different interfaces obtained through solvent vapor annealing (SVA). We demonstrate a 15 W oxygen plasma method to remove the PS block and simultaneously oxidize the PDMS into hard silicon oxycarbide cylinders (ox-PDMS) [4]. Finally, the pattern transfer into mechanically exfoliated hBN flakes is verified.

Results and discussion

The fabrication process is illustrated in Figure 1. No surface treatment was used before the spin casting of the PS-PDMS (27K/11K) block copolymer thin film onto a wafer with exfoliated flakes of 2D materials. The resulting film thickness, t_{film} , as determined by atomic force microscopy (AFM), was 30-40 nm, close to an integer multiple of the natural period (L_0). However, the presence of exfoliated 2D material flakes with different heights ranging from monolayers (4.1\AA) to multilayers of hundreds of nm, produced inhomogeneities in the film thickness in different areas on the substrate. As reported for other cylindrical forming BCP systems, the equilibrium order depended heavily on the film thickness [1] and it was expected to influence the ordering of the oxidized PDMS cylinders over a large area.

The samples were annealed for 20 min in toluene vapor at RT [22, 33]. The ratio, S/V (S = surface area of the solvent, V = volume of air mixing with the solvent vapor) was kept at around 0.65 cm^{-1} . After SVA, terraces with thicknesses approximately 10 nm taller/deeper than the original thickness were formed on all samples. These was observed by both SEM- and AFM images, seen in Figure 2 and Figure S1 respectively.

To investigate this further, SEM/FIB cross-sectional lift-outs were made which also allowed us to investigate the wetting of PS-PDMS on hBN. Two lift-out regions were chosen from optical microscope

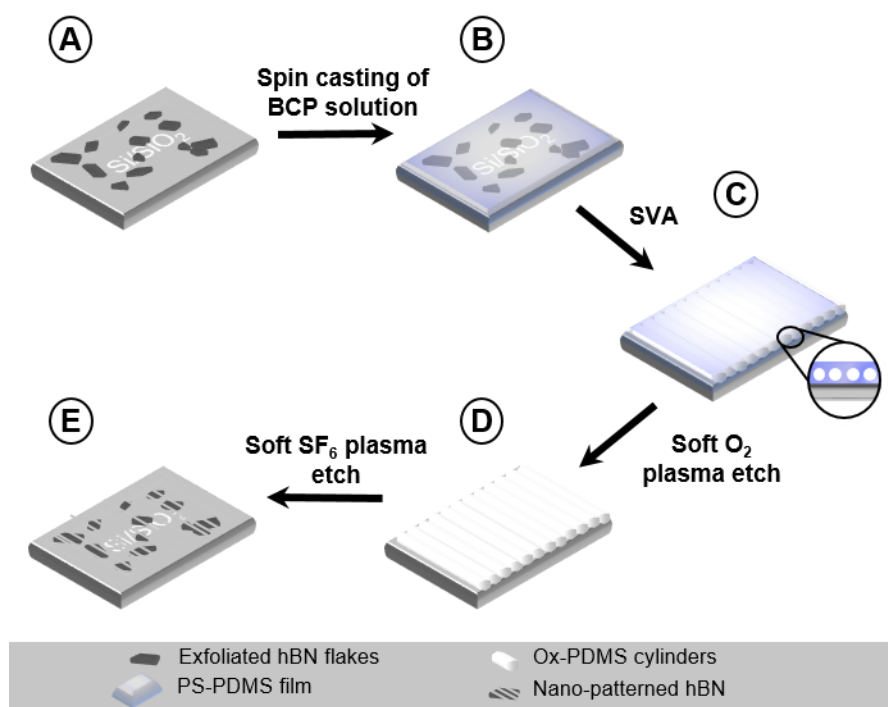


Figure 1: Illustration of the BCP lithography process. **A)** hBN flakes were exfoliated onto an argon plasma etched Si/SiO₂(90nm) substrate. **B)** A PS-PDMS (38K) solution was spin-cast with a static method onto the Si/SiO₂/hBN, leaving a thin film of approx. 30-40 nm. **C)** SVA in toluene for 20 min at RT. **D)** A O₂ plasma etch, removes the PS block and leaves a robust ox-PDMS hard mask on top of hBN. **E)** A furnace annealing and a SF₆ plasma etch, removes the exposed parts of the hBN flakes and the ox-PDMS, leaving nano-patterned hBN flakes. order depended heavily on the film thickness [1] and it was expected to influence the ordering of the ox-PDMS cylinders over a large area

images, one showing a varying film thickness on a hBN flake and one showing a smooth film on an hBN flake, see Figure 2A and Figure S2. Figure 2A shows a SEM image from the varying film thickness region. The dark terraces was, through the cross-sectional STEM images, found to contain ordered PDMS cylinders in a PS while the brighter parts showed a different morphology.

Figure 2B is a zoom-in from an area with a film thickness of 29 nm. Here the desired morphology with PDMS cylinders in a PS matrix is found with a periodicity, $L_0 \sim 35$ nm and a PDMS cylinder diameter of 15 nm. In previous cross-sectional studies of PS-PDMS films under SVA they observed an elliptic distortion of the PDMS cylinders which is discussed to originate from in-plane film strain formed by the solvent evaporation [17, 18]. This distortion is however, not observed in this study. Going towards an area with a lower film thickness, the morphology changes. Figure 2C shows a zoom-in of an area with a PS-PDMS monolayer film thickness of 21.5 nm. Here, a lamellar morphology parallel to the hBN surface is observed. This pattern could also be from a PDMS cylinder cut in half, with a diameter of 10 nm. However, this would mean that the equilibrium morphology would accept film thicknesses ranging from around 35 to 21.5 nm which seems unreasonable when considering the systems morphology sensitivity towards thickness changes [18]. The presence of silicon in the dark grey areas of the PS-PDMS film was confirmed by energy electron loss spectroscopy (EELS), see Figure S3. STEM images from the smooth film region are found in Figure S2. Here a non-ordered multilayer PS-PDMS film on hBN was found.

In all cases, we observe a selective wetting towards PS at the hBN/BCP interface and no top- or bottom PDMS wetting layer(s) at either the BCP/air interface or the hBN/BCP interface. This is a surprise, especially the fact that no PDMS wetting layer is observed at the BCP/air interface. The PDMS wetting layers are created because of the large difference in surface tension between PS (40.7 mN/m) and PDMS (19.9 mN/m) which leads to PDMS segregation at the interfaces [34]. Our findings are in contrast to

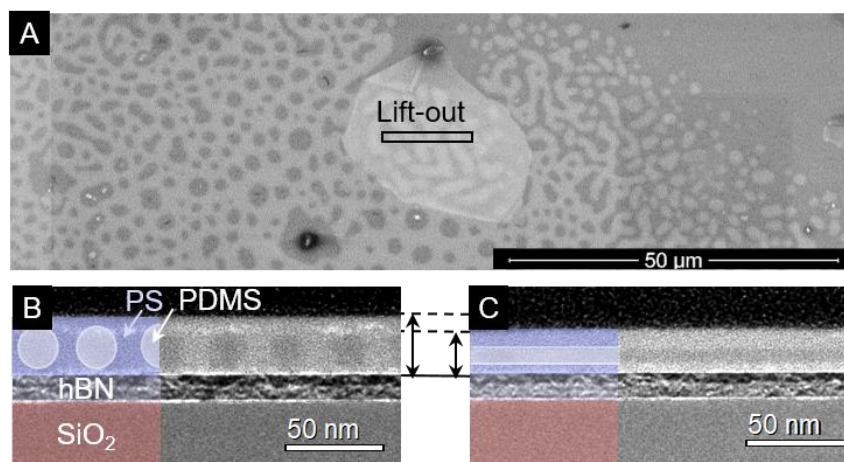


Figure 2: A) SEM image from before taken lift-out of hBN flake with a SVA PS-PDMS on top. The dark areas correspond to areas with horizontal PDMS cylinders in a PS matrix as seen in the cross-sectional STEM images of a sample lift-out with Pt/C protection on top of PS-PDMS on a hBN flake (12 nm thick)/SiO₂ (90 nm)/Si. B) zoom on an area with PDMS cylinders parallel to the hBN surface in a PS matrix and a film thickness of 29 nm. C) zoom on an area with PS-PDMS lamellae ordering parallel to the hBN surface and a PS-PDMS film thickness of 21.5 nm. The thickness difference between the two areas is illustrated with the arrows.

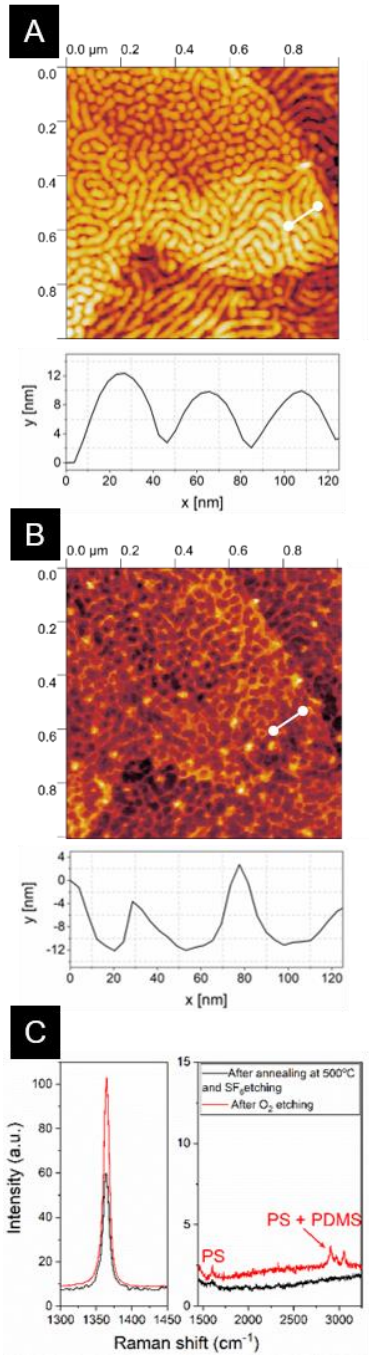


Figure 3: AFM height images at the edge of an hBN flake during the BCP lithography process. Height profiles from the white lines are shown beneath. **A)** After O_2 plasma etching, the height profile shows the contour of the ox-PDMS cylinders on top of an hBN flake. **B)** After furnace annealing and an SF_6 plasma etch, the height profile shows the inverted pattern into the hBN flake. **C)** Raman spectra of **A)** where PS is still present together with ox-PDMS after O_2 etching (red line) and **B)** after furnace annealing SF_6 plasma etching showing no presence of PS and PDMS seen (black line).

previous observations with PS-PDMS on CVD graphene surfaces that have not been functionalized either thermally or by applying a polymer brush [7, 35]. The water contact angle for CVD graphene has been experimentally found to be around 68° but can be increased to 94.8° with a thermal treatment which results in the absence of a PDMS wetting layer at graphene/BCP interface [7]. Similar increases in contact angles from 60° to 80° have been reported for exfoliated graphene when exposed to air over 4 days, whereas for exfoliated hBN, a smaller increase is observed from approximately 82° to 88° [36]. Compared to CVD graphene, hBN has a slightly lower surface energy, which could explain the lack of a PDMS wetting layer at the hBN/BCP interface. The reason for the lack of a similar interface at the BCP/air interface is not clear.

The presence of PDMS wetting layers depends not only on the preferential interaction between the BCP and the substrate [18] but also the film thickness [37] and the annealing procedure [15]. The lack of a PDMS wetting layer at the CVD graphene/BCP interface has been observed in one study using a combination of toluene solvent vapor- and thermal annealing ($>45^\circ C$) [15]. They argue that the lack of the PDMS wetting layer is due to the toluene vapor pressure being high enough and slightly selective towards PS, to compensate for the PDMS segregation. However, our findings suggest that this compensation might already be realized by SVA in toluene at RT.

A lack of a PDMS wetting layer at the BCP/air interface is useful in this work, since this means that plasma etching used to form the hard mask can be performed in a single step with O_2 plasma. We used plasma powers of 10-15 W which are ideal for 2D material processes, but are an order of magnitude smaller than typical plasma powers for BCP lithography [16, 23]. The O_2 process parameters was 10 sccm, 15 W, 20 min. Figure 3A shows an AFM height image of an hBN flake edge with ox-PDMS on top after O_2 plasma etching. The presence of vertical and horizontal cylinders is seen on hBN whereas only

horizontal cylinders are observed on SiO₂. The top part of the hBN flake, which contains the largest number of vertical cylinders is thinner than the rest of the hBN flake, suggesting that the difference in BCP morphology is due to film thickness variations caused by the difference in flake thickness. Though, in general a larger number of vertical cylinders was found on hBN flakes compared to SiO₂ which either means that hBN is somewhat non-selective towards the two blocks creating a perpendicular orientation or that a larger film thickness variation is seen on hBN compared to SiO₂. However, this was not investigated further. The height profile reveals 6-12 nm high cylinders and an $L_0 = 38.9$ nm which is in accordance with the STEM cross section results. Raman spectroscopic measurements after O₂ etching showed the presence of PS residues (Figure 3C). These residues have been shown to affect the electronic properties of 2D materials [24, 25]. To remove these residues, furnace annealing at 500°C under Ar/H₂ flow was performed. Finally, an SF₆ etching step (10 sccm, 10 W, for approximately 30 s) transferred the pattern into the hBN flakes, with the ox-PDMS acting as a mask. Figure 3B shows an AFM height image of the same hBN flake edge after furnace annealing and SF₆ plasma etching. The height profile shows up to 15

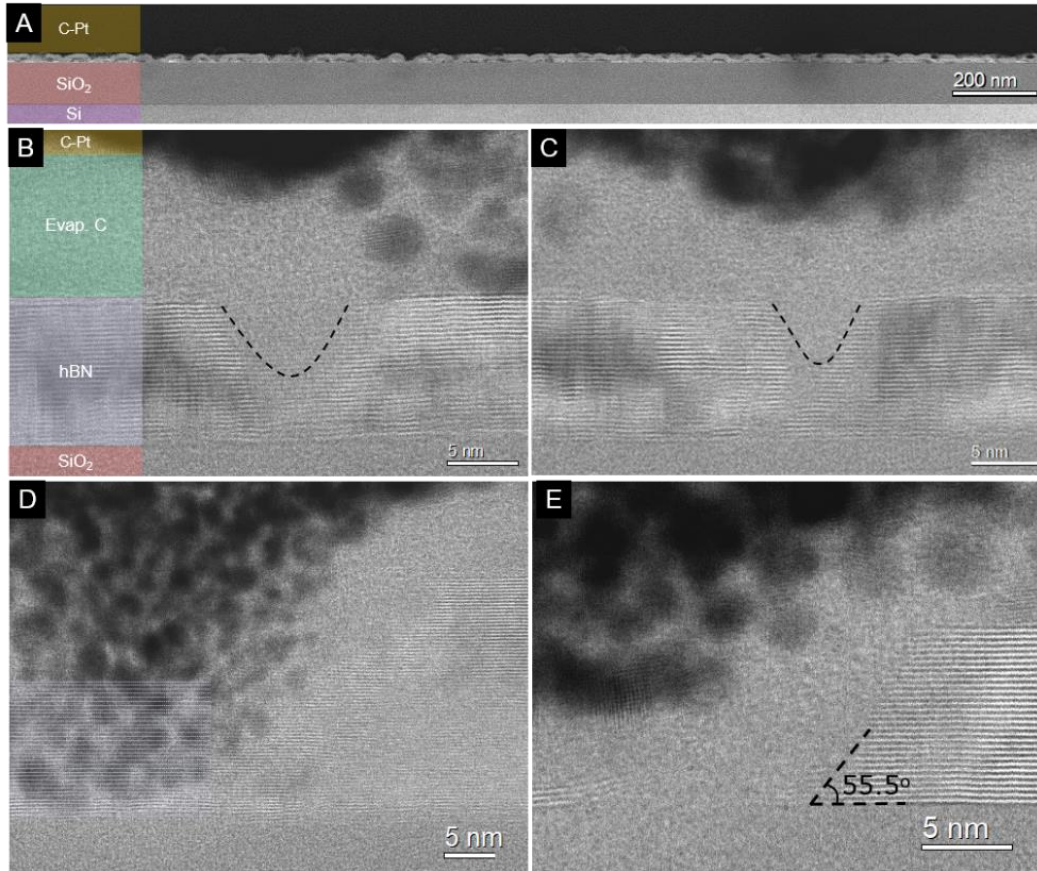


Figure 4: Cross-sectional (S)TEM images of a sample lift out after annealing and SF₆ etching. A) and B) are images of the same area taken with different microscope focuses revealing a patterned hole that continues throughout the 100 nm cross-section. C) Shows an overview of the nano-patterned hBN flake. The amorphous carbon-Pt (C-Pt) protection layer helps to identify where the flake has been patterned. D) and E) are images of the same area taken with different microscope focuses showing a pattern that does not continue throughout the 100 nm cross-section. The blue lines in D) mark the hBN layers seen through the protection layer. Layers, Yellow: MeCpPtMe₃, Green: Evap. C = evaporated carbon, Blue: hBN, Red/Purple: SiO₂/Si.

nm deep holes. Additionally, we observed the complete removal of both PS and PDMS after annealing and SF₆ etching, further confirmed by the Raman spectroscopy measurements presented in Figure 3C.

To fully confirm the pattern transfer to the hBN flake we did a SEM/FIB cross-sectional lift-out and investigated it with (S)TEM imaging. In Figure 4A a 1.5 μm overview image of the nano-patterned hBN flake, shown in the inset of Figure 4B, is shown. The platinum containing protection layer reveals the non-ordered patterns, which is in good agreement with the aforementioned AFM and STEM images. The STEM images show the projection of the front of the cross section which can be changed by changing the focus of the electron microscope and with this it is possible to verify the origin of the patterns. Figure 4B shows a hole that continues when changing the focus, see Figure 4C. This indicates that an ox-PDMS mask with horizontal lying cylinders has been present prior to the SF₆ etching. Another thing to note is that there is no significant changes in the evaporated carbon layer which is a strong indication that all PS- PDMS residues have been removed, leaving a clean nano-patterned hBN surface.

Figure 4D and Figure 4E again show STEM cross sectional images from the same area but with a different focus. In Figure 4E a clear sign of a hole is seen together with a etch angle of 55.5°. presence of hBN layers marked in Figure 4D is an indication that the pattern does not continue throughout the 100 nm cross-section and that it originates from an ox-PDMS mask with vertical standing cylinders. Additional cross sectional images can be found in the supplementary materials, Figure S4. Furthermore, in this study, angles of etched hBN sidewalls from 49-56° were observed; approximately 10° lower than the range of sidewall angles found in the literature [38, 39]. Our results suggest that a lower power plasma results in a smaller sidewall angle than in the case of higher powers for similar chamber pressures. This lower sidewall angle is an advantage when considering using this process to nano-pattern graphene in hBN/graphene/hBN stacks, since it can provide an additional reduction in the feature size [39].

Conclusion

We have shown a BCP lithography process that can be used to nano-pattern mechanically exfoliated hBN flakes without requiring special pre-treatment, e.g. a polymer brush layer. Through cross-sectional lift-outs, the interactions between PS-PDMS and hBN were shown to allow the self-assembly of a monolayer of PDMS cylinders in a PS matrix parallel to the hBN flake. Notably, this occurs without the formation of PDMS wetting layers either at the substrate or air interfaces. After a single step of O₂ plasma etching, AFM images revealed the presence of both vertical and horizontal hard silicon oxycarbide cylinders lying on top of hBN. These patterns could be transferred into hBN flakes through an SF₆ etch step followed by furnace annealing, leaving a clean hBN surface that is ideal for device applications. With this study, we hope to pave the way for the application of BCP lithography to nano-pattern mechanically exfoliated 2D materials and heterostructures other than graphene. This enables patterning of a wider range of materials not only beyond the resolution limit of conventional nanolithography, but also in a scalable manner.

Experimental

Materials and methods

Materials and block copolymer (BCP) synthesis:

PS-PDMS (M_n : 37.9 kg/mol, PDI: 1.1 (GPC results measured against PS standards), f_{PDMS} : 0.28 (from 1H -NMR), $L_{0, calc.}$: 24 nm from self-consistent mean-field (SCMF) theory, assuming χ = 0.265 [40] and other values from [41]) was synthesized by living anionic polymerization. Polymerization of styrene in cyclohexane was initiated with sec-butyllithium and hexamethylcyclotrisiloxane was added after 18h. The reaction was left overnight at RT. The next morning THF was added and the reaction was left to stir for 2h at RT before getting cooled to 0°C and left there for 3 days. Hereafter, the reaction was terminated with chlorotrimethylsilane. All solvents were purchased from research chemical suppliers and monomer and solvent purification was done as described elsewhere [42].

Fabrication of Si/SiO₂/hBN/PS-PDMS samples:

Si/SiO₂ (90nm) substrates were marked with an index mark system using optical lithography and deposition of Cr/Au in a conventional lift-off process. Crystals of hBN were purchased from HQ Graphene and exfoliated onto these Si/SiO₂ substrates with semiconductor die sawing tape (Nitto Denko) after pre-treatment of the wafers with a O₂ plasma (PlasmaEtch PE-50, 120W, ~200 Torr, 5 sccm, 8-10 min) to improve adhesion. The PS-PDMS was dissolved in cyclohexane with a 1 wt% concentration and spin-coated at 3000 rpm, acceleration 500 rpm/s for 60s with a static dispense method onto the Si/SiO₂/hBN, leaving a thin film of approx. 35 nm. The film was solvent vapor annealed on a petri dish within a petri dish (approx. S/V = 0.68 [19]) with toluene (2.5 mL) and a lid on top for 20 min at RT. Hereafter, the sample was subjected to a O₂ plasma etch (Moorfield Minilab 026, 15W, running pressure: 1.8×10^{-2} mbar, 10 sccm, DC bias: 160 V, ~20 min), removing the PS block and leaving a robust oxidized PDMS template on top of hBN. An annealing step at 500°C for 3h in 3% H₂/Ar was introduced to remove residual PS. A SF₆ plasma etch (Moorfield Minilab 026, 10W, running pressure: 1.8×10^{-2} mbar, 10 sccm, DC bias: 128 V, ~30-60s) removed the exposed parts of the hBN flakes and the ox-PDMS, leaving only the patterned hBN flakes.

Atomic force microscopy (AFM)

AFM measurements were conducted in a Bruker Dimension Icon-PT, in either soft-tapping air mode (height and phase) or with ScanAsyst mode (height). A standard tapping mode tip was used, and the typical acquisition parameters were 256 lines with a scan rate of 0.99 Hz. Scan sizes were typically 500nm-4μm.

Focus ion beam (FIB) processing and scanning electron microscopy (STEM)

The sample edges were painted with silver paint to reduce charges from building up and mounted on an SEM holder. The FIB processing was done on an FEI-Helios dual beam system with 5kV and the sample preparation was done as described elsewhere [43]. All samples were coated with an electron beam deposited gas, Trimethyl(methylcyclopentadienyl)platinum(IV) (MeCpPtMe₃) before FIB milling. The nano-patterned hBN sample was coated with evaporated carbon and 1-2 nm gold before the e-beam coating to protect the surface from the harsh MeCpPtMe₃ e-beam deposition. The cross-sectional lift-

outs were thinned with the FIB before during STEM measurement. STEM bright- and dark field and STEM-EELS measurements were conducted on a Titan Analytical 80-300ST TEM operated at 300 kV or 120 kV.

Associated content

Supplementary material

Corresponding author

Kristoffer Almdal, kral@dtu.dk

Acknowledgments

The work described in this paper was supported by the Center for the Nanostructured Graphene (CNG) sponsored by the Danish National Research Foundation DNR103 together with the Department of Chemistry and Physics at the Technical University of Denmark (DTU). TB gratefully acknowledges support from the Villum Foundation project IonGate [grant number] and the Novo Nordisk Foundation project BIOMAG [grant number]

References

1. Knoll, A., et al., *Phase behavior in thin films of cylinder-forming block copolymers*. Physical Review Letters, 2002. **89**(3).
2. Park, W.I., et al., *Self-Assembled Incorporation of Modulated Block Copolymer Nanostructures in Phase-Change Memory for Switching Power Reduction*. Acs Nano, 2013. **7**(3): p. 2651-2658.
3. Park, W.I., et al., *Self-Assembly-Induced Formation of High-Density Silicon Oxide Memristor Nanostructures on Graphene and Metal Electrodes*. Nano Letters, 2012. **12**(3): p. 1235-1240.
4. Nourbakhsh, A., et al., *MoS₂ Field-Effect Transistor with Sub-10 nm Channel Length*. Nano Letters, 2016. **16**(12): p. 7798-7806.
5. Son, J.G., et al., *Sub-10 nm Graphene Nanoribbon Array Field-Effect Transistors Fabricated by Block Copolymer Lithography*. Advanced Materials, 2013. **25**(34): p. 4723-4728.
6. Kim, M., et al., *Fabrication and Characterization of Large-Area, Semiconducting Nanoperforated Graphene Materials*. Nano Letters, 2010. **10**(4): p. 1125-1131.
7. Arias-Zapata, J., et al., *Engineering Self-Assembly of a High- χ Block Copolymer for Large-Area Fabrication of Transistors Based on Functional Graphene Nanoribbon Arrays*. Chemistry of Materials, 2019. **31**(9): p. 3154-3162.
8. Park, H., et al., *Nano-patterning on multilayer MoS₂ via block copolymer lithography for highly sensitive and responsive phototransistors*. Communications Materials, 2021. **2**(1).
9. Zhou, C., et al., *Fabrication of Nanoporous Alumina Ultrafiltration Membrane with Tunable Pore Size Using Block Copolymer Templates*. Advanced Functional Materials, 2017. **27**(34).
10. Huang, S.Q., et al., *Single-layer graphene membranes by crack-free transfer for gas mixture separation*. Nature Communications, 2018. **9**.
11. Cummins, C., et al., *Enabling future nanomanufacturing through block copolymer self-assembly: A review*. Nano Today, 2020. **35**.

12. Morris, M.A., *Directed self-assembly of block copolymers for nanocircuitry fabrication*. Microelectronic Engineering, 2015. **132**: p. 207-217.
13. Radamson, H.H., et al., *The Challenges of Advanced CMOS Process from 2D to 3D*. Applied Sciences-Basel, 2017. **7**(10).
14. Stanford, M.G., P.D. Rack, and D. Jariwala, *Emerging nanofabrication and quantum confinement techniques for 2D materials beyond graphene*. npj 2D Materials and Applications, 2018. **2**(20): p. 1-15.
15. Rasappa, S., et al., *High quality sub-10 nm graphene nanoribbons by on-chip PS-b-PDMS block copolymer lithography*. 2015.
16. Jung, Y.S., et al., *A Path to Ultranarrow Patterns Using Self-Assembled Lithography*. Nano Letters, 2010. **10**(3): p. 1000-1005.
17. Bohme, S., et al., *Annealing treatments of cylindrical siloxane-based block copolymers optimized for nanomanufacturing*. Micro and Nano Engineering, 2018. **1**: p. 56-62.
18. O'Driscoll, B.M.D., et al., *Achieving structural control with thin polystyrene-b-polydimethylsiloxane block copolymer films: The complex relationship of interface chemistry, annealing methodology and process conditions*. European Polymer Journal, 2013. **49**(11): p. 3445-3454.
19. Jung, Y.S. and C.A. Ross, *Solvent-Vapor-Induced Tunability of Self-Assembled Block Copolymer Patterns*. Advanced Materials, 2009. **21**(24): p. 2540-+.
20. Rasappa, S., et al., *Morphology evolution of PS-b-PDMS block copolymer and its hierarchical directed self-assembly on block copolymer templates*. Microelectronic Engineering, 2018. **192**: p. 1-7.
21. Berger, C., et al., *Electronic confinement and coherence in patterned epitaxial graphene*. Science, 2006. **312**(5777): p. 1191-1196.
22. Jessen, B.S., et al., *Lithographic band structure engineering of graphene*. Nature Nanotechnology, 2019. **14**(4): p. 340-346.
23. Arias-Zapata, J., et al., *Effective patterning and cleaning of graphene by plasma etching and block copolymer lithography for nanoribbon fabrication*. Journal of Vacuum Science & Technology A, 2018. **36**(5).
24. Bai, J., et al., *Graphene nanomesh*. Nature Nanotechnology, 2010. **5**(3): p. 190-194.
25. Pettes, M.T., et al., *Influence of Polymeric Residue on the Thermal Conductivity of Suspended Bilayer Graphene*. Nano Letters, 2011. **11**(3): p. 1195-1200.
26. Li, T., et al., *Substrate tolerant direct block copolymer nanolithography*. Nanoscale, 2016. **8**(1): p. 136-140.
27. Fang, T., et al., *Mobility in semiconducting graphene nanoribbons: Phonon, impurity, and edge roughness scattering*. Physical Review B, 2008. **78**(20).
28. Bang, K., et al., *Effect of ribbon width on electrical transport properties of graphene nanoribbons*. Nano Convergence, 2018. **5**.
29. Jiao, L.Y., L.M. Xie, and H.J. Dai, *Densely aligned graphene nanoribbons at similar to 35 nm pitch*. Nano Research, 2012. **5**(4): p. 292-296.
30. Kim, S.S., et al., *Large area tunable arrays of graphene nanodots fabricated using diblock copolymer micelles*. Nanotechnology, 2012. **23**(12).

31. Hu, S., et al., *Proton transport through one-atom-thick crystals*. Nature, 2014. **516**(7530): p. 227-+.
32. Chen, C., et al., *Functionalized boron nitride membranes with ultrafast solvent transport performance for molecular separation*. Nature Communications, 2018. **9**.
33. Sandner, A., et al., *Ballistic Transport in Graphene Antidot Lattices*. Nano Letters, 2015. **15**(12): p. 8402-8406.
34. Andersen, T.H., et al., *Surface morphology of PS-PDMS diblock copolymer films*. Journal of Electron Spectroscopy and Related Phenomena, 2001. **121**(1-3): p. 93-110.
35. Lee, J., et al., *Uniform Graphene Quantum Dots Patterned from Self-Assembled Silica Nanodots*. Nano Letters, 2012. **12**(12): p. 6078-6083.
36. Keerthi, A., et al., *Water friction in nanofluidic channels made from two-dimensional crystals*. Nature Communications, 2021. **12**(1).
37. Wang, Q., P.F. Nealey, and J.J. de Pablo, *Monte Carlo simulations of asymmetric diblock copolymer thin films confined between two homogeneous surfaces*. Macromolecules, 2001. **34**(10): p. 3458-3470.
38. Chan, C.-M. and E. Michele, *Polymer surface modification and characterization*. 1st ed. ed. 1994, Munich: Hanser publishers.
39. Danielsen, D.R., et al., *Super-Resolution Nanolithography of Two-Dimensional Materials by Anisotropic Etching*. Acs Applied Materials & Interfaces, 2021. **13**(35): p. 41886-41894.
40. Gu, X., I. Gunkel, and T.P. Russell, *Pattern transfer using block copolymers*. Philos. Trans. R. Soc. A: Mathematical, Physical and Engineering Sciences, 2013. **371**(2000): p. 20120306.
41. Rubinstein, M. and R.H. Colby, *Polymer Physics*. Reprint ed. 2006, London: Oxford Univ. Press.
42. Ndoni, S., et al., *LABORATORY-SCALE SETUP FOR ANIONIC-POLYMERIZATION UNDER INERT ATMOSPHERE*. Review of Scientific Instruments, 1995. **66**(2): p. 1090-1095.
43. Andersen, A.B., et al., *Limiting Damage to 2D Materials during Focused Ion Beam Processing*. Physica Status Solidi B-Basic Solid State Physics, 2020. **257**(12).